PAVEMENT PERFORMANCE EVALUATION USING CONNECTED VEHICLES

A Dissertation
Submitted to the Graduate Faculty
of the
North Dakota State University
of Agriculture and Applied Science

By

Rajinder Bridgelall

In Partial Fulfillment of the Requirements
for the Degree of
DOCTOR OF PHILOSOPHY

Major Program:
Transportation and Logistics

June 2015

Fargo, North Dakota

North Dakota State University
Graduate School

Title

Pavement Performance Evaluation Using Connected Vehicles

By

Rajinder Bridgelall

The Supervisory Committee certifies that this ***disquisition*** complies with North Dakota State University's regulations and meets the accepted standards for the degree of

DOCTOR OF PHILOSOPHY

SUPERVISORY COMMITTEE:

Denver D. Tolliver
Chair

Kendall E. Nygard

Ying Huang

J. Bruce Rafert

Pan Lu

Approved:

6-24-2015
Date

Denver D. Tolliver
Department Chair

ABSTRACT

Roads deteriorate at different rates from weathering and use. Hence, transportation agencies must assess the ride quality of a facility regularly to determine its maintenance needs. Existing models to characterize ride quality produce the International Roughness Index (IRI), the prevailing summary of roughness. Nearly all state agencies use Inertial Profilers to produce the IRI. Such heavily instrumented vehicles require trained personnel for their operation and data interpretation. Resource constraints prevent the scaling of these existing methods beyond 4% of the network. This dissertation developed an alternative method to characterize ride quality that uses regular passenger vehicles. Smartphones or connected vehicles provide the onboard sensor data needed to enable the new technique.

The new method provides a single index summary of ride quality for all paved and unpaved roads. The new index is directly proportional to the IRI. A new transform integrates sensor data streams from connected vehicles to produce a linear energy density representation of roughness. The ensemble average of indices from different speed ranges converges to a repeatable characterization of roughness. The currently used IRI is undefined at speeds other than 80 km/h. This constraint mischaracterizes roughness experienced at other speeds. The newly proposed transform integrates the average roughness indices from all speed ranges to produce a speed-independent characterization of ride quality. This property avoids spatial wavelength bias, which is a critical deficiency of the IRI.

The new method leverages the emergence of connected vehicles to provide continuous characterizations of ride quality for the entire roadway network. This dissertation derived precision bounds of deterioration forecasting for models that could utilize the new index. The results demonstrated continuous performance improvements with additional vehicle

participation. With practical traversal volumes, the achievable precision of forecast is within a few days. This work also quantified capabilities of the new transform to localize roadway anomalies that could pose travel hazards. The methods included derivations of the best sensor settings to achieve the desired performances. Several case studies validated the findings. These new techniques have the potential to save agencies millions of dollars annually by enabling predictive maintenance practices for all roadways, worldwide.

ACKNOWLEDGEMENTS

I am grateful to my advisor, Dr. Denver D. Tolliver for the opportunity and flexibility to pursue this challenge while working. His guidance and interest in my professional development has made this journey an absolute delight. His lectures and class notes inspired some of the main ideas of this dissertation. I sincerely thank my supervisory committee members for all the support and critical reviews that helped to improve the dissertation quality. Dr. Kendall Nygard provided me with a solid education to develop some of the statistical methods utilized. Dr. Ying Huang provided critical reviews of my early work that provided a framework for this research. The unending professional guidance and feedback from Dr. J. Bruce Rafert has helped me to manage multiple simultaneous challenges in achieving the goals of this effort. Dr. Pan Lu provided an assessment of the initial ideas that eventually blossomed into the technical foundation of this dissertation. Throughout this journey, my sons Aaron and Isaac have seen less of me than they deserved; I am especially thankful to them for their patience and understanding. Finally, I would like to include a special note of thanks to my wife, Joanne, for her continuous encouragement, support, and love.

TABLE OF CONTENTS

LIST OF TABLES

LIST OF FIGURES

LIST OF ABBREVIATIONS

AADT ..... Annual Average Daily Traffic

ARI ..... Accelerometer Roughness Index

BPR ..... Bureau of Public Roads

CSV ..... Comma Separated Value

DFT ..... Discrete Fourier Transform

DSP ..... Digital Signal Processing

DSRC ..... Dedicated Short-Range Communications

EAR ..... Ensemble Averaged RIF

FHWA ..... Federal Highway Administration

FIR ..... Finite Impulse Response

GB ..... Gigabyte

GIS ..... Geographic Information System

GMRL ..... General Motors Research Laboratory

IRI ……..... International Roughness Index

ITS ..... Intelligent Transportation Systems

KDOH ..... Kentucky Department of Highways

LOS …..... Level-of-Service

LTI ..... Linear Time-Invariant

LTPP ..... Long-Term Pavement Performance

LWP ..... Left Wheel Path

MAC ..... Multiply-and-Accumulate

MOE ..... Margin of Error

NCHRP ..... National Cooperative Highway Research Program

NDDOT ..... North Dakota Department of Transportation

NHS ……..... National Highway System

PSD ..... Power Spectral Density

PSI ..... Present Serviceability Index

PSR ……..... Present Serviceability Rating

RIF ……... Road Impact Factor

RMS ..... Root-Mean-Square

RMSVA ..... Root-Mean-Square Vertical Acceleration

RTRRMS ..... Response-Type Road Roughness Measuring System

RWP ..... Right Wheel Path

SAE ..... Society of Automotive Engineers

SUB ..... Sports Utility Vehicle

SV ..... Slope Variance

TRB ..... Transportation Research Board

TWIT ……... Time-Wavelength-Intensity Transform

UAS ..... Unmanned Aircraft System

USDOT …..... United States Department of Transportation

V2I ……..... Vehicle-to-Infrastructure

V2V ……..... Vehicle-to-Vehicle

WSDOT ..... Washington State Department of Transportation

LIST OF SYMBOLS

$a_z(t)$ ..... vertical acceleration from the body bounces of a quarter-car

$a_{z[n]}(t)$ ..... vertical acceleration from the body bounces of a quarter-car n

$A_{LP[n]}$ ……..... low-pass filter amplitude for quarter-car n

B_k ……..... number of speed bands available for segment k

c_s ..... viscous damping coefficient of a quarter-car

$c_{\mu s}$ ……...…. average damping coefficient of the sprung-mass for a set of vehicles

$c_{\mu u}$ ……...…. average damping coefficient of the unsprung-mass for a set of vehicles

C_H ..... degree of unevenness for a power spectral density

$D_g(\imath)$ …….. Gaussian distribution as a function of frequency bin $\imath$

$D_L(\imath)$ …….. logistic distribution as a function of frequency bin $\imath$

$D_n(\imath)$ …….. Log normal distribution as a function of frequency bin $\imath$

$D_t(\imath)$ …….. Student's t-distribution as a function of frequency bin $\imath$

$E_{z\delta}$ ……..... vertical acceleration signal energy from an impulse excitation

E_{gz}^{L} ……..... longitudinal energy density of vertical acceleration signal energy

$\overline{E}_{gz}^{L}$ ……..... average of the vertical acceleration signal energy density among traversals

E_{kv} ..... vertical acceleration kinetic energy for a road segment

E_{pv} ..... vertical acceleration potential energy for a road segment

e ..... Euler's mathematical constant

$e_n[k]$ ……..... noise sample k

$e_{[n,\kappa]}$ …….. sampled signal error for traversal κ

f ……..... frequency in hertz

$\bar{f}_A$ ..... average sample rate of the inertial sensor

f_s ..... signal sample rate in hertz

$f_{[c,n]}$ ..... low-pass filter cut-off frequency for quarter-car n

$f_{\mu s}$ .....estimated sprung-mass resonance mode frequency

$f_{\mu u}$ .....estimated sprung-mass resonance mode frequency

$f_{[s,n]}$ ..... sprung-mass resonance mode frequency

$f_{[u,n]}$ ..... unsprung-mass resonance mode frequency

$f_z(t)$ ..... vertical forces acting on a quarter-car system

h ..... compression distance of a quarter-car suspension spring

g ..... unit of standard gravity defined as 9.81 $m \cdot s^{-1}$

$\bar{g}_{\bar{v}}^{L}$ ..... average g-force magnitude at speed $\bar{v}$ for a segment of length L

$g_z(t)$ ..... g-force output from a vertical acceleration sensor as a function of time t

g_{xu} ..... sensor x-axis acceleration magnitude

g_{yu} ..... sensor y-axis acceleration magnitude

g_{zu} ..... sensor z-axis acceleration magnitude

$G_z(f)$ ..... magnitude spectrum of the vehicle inertial response

$G\sigma$ ..... magnitude threshold for locating the first inertial peak of a signal

$I_{\bar{v}}^{L}$ ..... International Roughness Index for a segment of length L, at an average speed $\bar{v}$

J_N ..... total number of time-periods in a dataset of historical ride quality

k_s ..... spring stiffness of a quarter-car

$k_{\mu u}$ ..... average unsprung mass spring stiffness for vehicles

L ..... length of road segment

m_s ..... sprung-mass of a quarter-car

m_u ..... unsprung-mass of a quarter-car

$m_{\mu u}$ ..... average unsprung mass for a vehicle

$m_{\mu G}$ ..... average gross mass for a vehicle

N_{FIR} ..... number of FIR filter taps

N_k ..... total number of speed bands available for segment k

N_κ ..... noise energy for traversal κ

$N_{\bar{v}[w]}^{P_j}$ ..... traversal volume within the speed band $\bar{v}[w]$ for period ΔP_j

ΔP_j ..... time-period increment of instance j

$q_{1-\alpha/2}$ ..... standard normal quartile for a (1-α)% confidence interval

$q_z(t)$ ..... quarter-car impulse response

$Q(f)$ ..... quarter-car frequency response

R_{earth} ..... mean earth radius of approximately 6371 kilometers

$R^L[p]$ ..... RIF-index for segment of length L evaluated in time-period p

$\overline{R}_{\bar{v}[w]}^{L}$ ..... ensemble average RIF-index for segment of length L and speed band $\bar{v}[w]$

$R_{\bar{v}}^{L}$ ..... RIF-index for segment of length L when traversed at an average speed $\bar{v}$

$\overline{R}_{\bar{\bar{v}}}^{\Delta L}$ ..... EAR-index for segment of length ΔL and batch mean speed $\bar{\bar{v}}$

$R_{\hat{v}}^{\delta}$ ..... theoretical maximum RIF-index from an impulse excitation

$\Delta R_{1-\alpha}^{L}$ ..... Margin-of-error for the RIF-index within a (1-α)% confidence interval

$s[k]$ ..... signal sample k

s_{RIF}^{L} ..... standard deviation of the RIF-index for segment of length L

$s^2_{\bar{\sigma}E}$ …….. covariance of the average speed and vertical acceleration signal energy

$S_H(\Omega)$ ..... spectral density as a function of spatial frequency Ω

$t_{df}(\imath)$ ..... t-distribution function of frequency bin $\imath$ and df degrees of freedom

$t_{1-\alpha/2,df}$ ……. t-distribution value at α significance and df degrees of freedom

T ……..... total traversal time across a segment

$\hat{T}(\psi_\alpha)$ …..... expected time to reach a future index of ride quality ψ_α

ΔT_ψ ….... margin-of-error in time estimate to reach a future index of ride quality ψ_α

T_ε ……..... traversal time when the quarter-car impulse becomes negligibly small

$T_{\mu GPS}$ …..... average update interval for the GPS receiver

$u(t)$ …..……. the Heaviside step function

$vE_{z\delta}$ ……..... variance of the vertical acceleration signal energy from an impulse excitation

$\bar{v}$ ..... average speed of a traversal

$\bar{\bar{v}}$ ..... batch mean speed amongst traversals

$\bar{v}[w]$ …...….. speed band of average speed $\bar{v}$ and instance w

w_v ..... waviness parameter for a power spectral density

W_z ..... number of wheel-assemblies in a simulated vehicle

x_0 ..... position of bump peak

$Z(f)$ ..... Fourier transform of the temporal bump profile

$Z_s(f)$ ..... sprung-mass frequency response of a quarter-car

$z(x)$ ……..... bump height profile as a function of longitudinal distance x

$z_s(t)$ …...….. sprung-mass temporal response

$\dot{z}_s(t)$…..…..... sprung-mass vertical motion rate

$z_u(t)$…..…... unsprung-mass temporal response

$\dot{z}_u(t)$…..…..... unsprung-mass vertical motion rate

$z_\delta(t)$ …..…...impulse response of a generic damped mass spring system

$z_{\delta s}(t)$ …..…...impulse response of a sprung-mass spring system

$\ddot{z}_{\delta s}(t)$ …..…... vertical acceleration of the impulse response of a sprung-mass spring system

$z_{\delta u}(t)$ ..…..…... impulse response of an unsprung-mass spring system

$\ddot{z}(t)$ ..... second derivative of the temporal elevation profile

α …….....significance value for a statistical distribution

$\alpha_{[u,n]}$ …….. proportion of each LPF in the parallel filter model

α_0 ..... bump model amplitude parameter

α_g ..... amplitude parameter of the Gaussian distribution model

α_L ..... amplitude parameter of the logistic distribution model

α_n ..... amplitude parameter of the lognormal distribution model

α_t ..... amplitude parameter of the Student's *t*-distribution model

β_L .....coefficient of empirical model to forecast deterioration for segment of length *L*

β_v ..... width scaling factor for a bump

$\beta_{z[n]}$ ..... coefficient of linear combination of vertical acceleration for quarter-car *n*

γ_g ……... inertial sensor constant

δ_r ……... high-resolution interpolation sub-interval for the EAR-indices

$\bar{\varepsilon}_b$ …….....bump position expected bias error from vehicle and sensor filtering delays

$\bar{\varepsilon}_d$ ……..... bump position expected bias error from vehicle and sensor transient responses

$\bar{\varepsilon}_{dGPS}$ ……. bump position expected bias from the GPS receiver trilateration errors

$\bar{\varepsilon}_{dlag}$…….. bump position expected bias from the GPS receiver position tag latency errors

$\bar{\varepsilon}_{DSP}$ …….. bump position expected bias error from DSP filtering

$\bar{\varepsilon}_{GPS}$ ……... bump position expected bias error from the GPS receiver sub-systems

$\bar{\varepsilon}_i$ ……..... bump position expected bias error from first peak path distance interpolation

ε_p ……..... distance tag for the first peak of the bump inertial response signal

$\bar{\varepsilon}_r$ ……..... bump position expected bias error from EAR-index interpolation subinterval

$\bar{\varepsilon}_s$ ……..... bump position expected bias error from sensor offset from the first axle

ζ_s ……...…... damping ratios of the sprung-mass frequency response

ζ_u ……...…... damping ratios of the unsprung-mass frequency response

$\zeta_{\mu s}$ ..... average damping ratio of the sprung-mass for a set of vehicles

$\zeta_{\mu u}$ ..... average damping ratio of the unsprung-mass for a set of vehicles

ζ_δ ……...…... damping ratios for the impulse response of the damped mass spring system

$\zeta_{[s,n]}$ …….. damping ratios of the sprung-mass frequency response, enumerated by n

$\zeta_{[u,n]}$ …….. damping ratios of the unsprung-mass frequency response, enumerated by n

η ……..... proportion of sprung-mass damping coefficient

$\Im[\bullet]$……..... Fourier transform operator

θ ……..... roll angle of unit vector rotation

κ_{RI} ..... RIF/IRI proportionality constant for an impulse excitation

λ ..... bump model width parameter

μ_g ..... mean parameter of the Gaussian distribution model

μ_L ..... mean parameter of the logistic distribution model

μ_n ..... mean parameter of the lognormal distribution model

μ_t ..... mean parameter of the Student's *t*-distribution model

ξ_0 ..... sharpness parameter for the bump model

$\rho_{z[n]}$ ..... coefficient of unsprung- to sprung-mass ratio for quarter-car *n*

ρ_δ ..... coefficient of linear combination for the quarter-car mass spring systems

σ^2_{dlag} ..... variance of the GPS receiver position estimate from position tagging latency

σ^2_{dlag} ..... variance of the GPS receiver position estimate from position tagging latency

σ^2_{EAR} ..... variance of the peak EAR-indices

σ_{fA} ..... standard deviation of the inertial sensor sample rate

σ_{fs} ..... standard deviation of the sprung-mass resonant frequency

$\sigma^2_{R\delta}$ ..... variance of the maximum RIF-index from an impulse excitation

$\overline{\sigma}_{\Delta dn}$ ..... average of the standard deviations of the GPS update distances amongst traversals

$\overline{\sigma}_{\Delta \tau m}$ .....average of the standard deviations of the GPS update times amongst traversals

$\overline{\sigma}_{\Delta \tau n}$ .....average of the standard deviations of the GPS update intervals amongst traversals

$\sigma^2_{\varepsilon DSP}$ ..... variance of the bias error from DSP delays

$\sigma_{\zeta u}$ ..... standard deviation of the unsprung-mass damping ratio

σ^2_{GPS} ..... variance of the GPS related position errors

$\sigma_{\varepsilon i}^2$ …..... variance of the bias error from interpolation

$\sigma_{\varepsilon s}$ …..... standard deviation of the bias error from sensor position

$\sigma_{\varepsilon d}$ …..... standard deviation of the bias error from transient responses

$\sigma_{\varepsilon r}$ …..... standard deviation of the bias error from interpolation subintervals

σ_g ..... standard deviation parameter of the Gaussian distribution model

σ_{msmu} ..... covariance factor of the sprung- and unsprung-mass distributions

$\sigma_{ms\omega u}$ ..... covariance factor of the sprung-mass and mode of the unsprung-mass

$\sigma_{mu\omega u}$ ..... covariance factor of the unsprung-mass and mode of the unsprung-mass

σ_{tag} …..... standard deviation of the GPS receiver position tagging latency

σ_L ..... standard deviation parameter of the logistic distribution model

σ_n ..... standard deviation parameter of the lognormal distribution model

σ_t ..... standard deviation parameter of the Student's *t*-distribution model

σ_v ..... standard deviation of the traversal velocity

$\sigma_{\bar{v}}$ ..... batch standard deviation of the mean speed amongst traversals

σ_{υ}^2 ..... variance of the position tag of the first peak in the inertial signal

$\sigma_{\bar{v}E}^2$ ..... covariance of the mean speed and vertical acceleration signal energy

$\sigma_{\omega u}$ ..... standard deviation of the unsprung-mass for a set of vehicles

$\sigma_{\zeta s}$ ..... standard deviation of the sprung-mass damping ratio

σ_R^L …….. standard deviation of the RIF for a segment of length L

$\bar{\tau}_{lag}$ …..... average GPS receiver position tagging latency

$\tilde{\upsilon}$ ……..... position bias error for a bump along a traversal path

$\tilde{\upsilon}_r$ ……..... position bias error of the peak EAR-index for a bump along a traversal path

υ_p ……..... reference position for a bump along a traversal path

$\hat{\upsilon}_p$ ……..... position estimate for a bump along a traversal path

$\hat{\upsilon}_r$ ……..... position of the EAR-index peak for a bump along a traversal path

ϕ ……..... yaw angle of unit vector rotation

χ^2 ……..... critical chi-squared value of the chi-squared test

ψ_0 ……..... initial index of ride quality for the empirical model of deterioration forecasting

ψ_α ……..... future index of ride quality for the empirical model of deterioration forecasting

$\psi(t)$ ……..... initial index of ride quality for the empirical model of deterioration forecasting

ω_n ……..... natural frequency of a damped mass system

ω_s ……..... natural frequency of sprung-mass system of a quarter-car

ω_u ……..... natural frequency of unsprung-mass system of a quarter-car

$\overline{\vartheta}_{dr}$ ……..... average phase shift of the sprung-mass equivalent sinusoidal combinations

$\Delta\varepsilon_{1-\alpha}$ ……... margin-of-error of the position estimate for the peak EAR-index

Δ_{cv} ……..... lumped covariance of the unsprung-mass damping ratio

Λ ……..... pitch angle of unit vector rotation

(Θ_E, Φ_E) ..... end pairs of latitude and longitude coordinates, respectively

(Θ_S, Φ_S)..... start pairs of latitude and longitude coordinates, respectively

Π_{xyz} ..... unit vector rotation in Cartesian space

$\Psi_k(\Delta P_j)$ ..... TWIT for time-period increment instance j

LIST OF APPENDIX TABLES

LIST OF APPENDIX FIGURES

CHAPTER 1. INTRODUCTION

The United States relies on the performance of more than four million miles of roadways to sustain its economic prosperity and to support the well-being of its growing population. However, transportation agencies rate less than half of those roadways as being in good condition (USDOT 2014). Researchers have determined that road roughness significantly increases the average annual cost of operating a vehicle (TRIP 2013). Agencies collectively lack the resources needed to scale existing methods of ride quality characterizations beyond the National Highway System (NHS), which accounts for less than 4% of the roadway network (HPMS 2012). The present methods of pavement performance evaluations include visual inspections that tend to disrupt traffic flows. This research develops an approach that enables regular vehicles to assess the roughness of any facility by providing continuous measures of ride quality. The new methods and models leverage the ubiquity of smartphones and the emergence of connected vehicles to provide unimpeded monitoring of the entire roadway network that includes both paved and unpaved roads.

The significance of this research is its broad impact to the economic prosperity of nations worldwide. The next section introduces a macro model to explain the interdependencies between the two distinct concepts of economic well-being and regular pavement performance evaluations. The challenges identified highlight the benefits of attaining the research objectives. The scope and methods of this research include model synthesis, simulations, and theoretical validation using data from several case studies. This chapter provides the context and motivation for the research, lists the research objectives, introduces the methods employed, summarizes the research contributions, and describes the organization of the dissertation.

1.1. Context and Motivation

Besides environmental factors, heavy vehicles contribute considerably to roadway deterioration. Many jurisdictions currently restrict the maximum gross weight of vehicles because they have long recognized that heavy vehicles such as trucks accelerate pavement deterioration (Khosla 1985). Trucks nevertheless play a critical role in the economic prosperity of a nation. They provide short-haul transport and connect intermodal shipments from long-haul modes such as air, rail, pipelines, and waterways to their final destinations. Trucks have consistently hauled between 60% to 70% of the U.S. freight tonnage moved by all modes (BTS 2013).

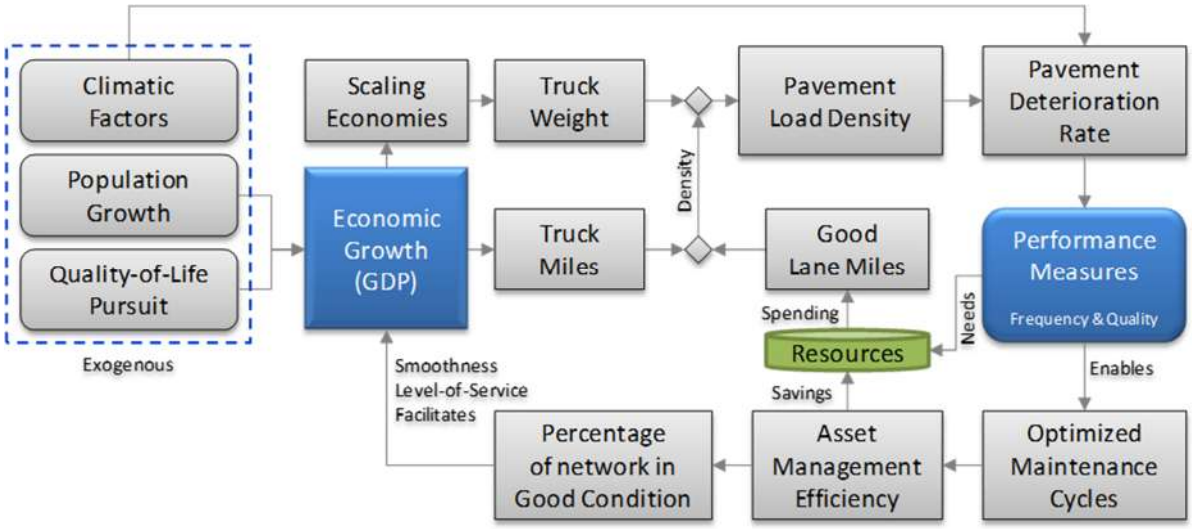

Figure 1. Infrastructure performance linked to economic growth

As illustrated in Figure 1 without a corresponding increase in good lane miles, continued economic growth and economies of scale will lead to greater pavement load density from trucks. Consequently, deterioration rates will accelerate. Trucks are becoming heavier because carriers strive to spread their fixed costs across a greater number of units shipped per vehicle to gain economies of scale. Analysts predict that the weight of shipments carried by trucks will increase by 1.3% per year from 2010 to 2040 (USDOT 2014).

Traffic density has already reached chronic congestion levels because the number of road miles has not kept up with travel demand. From 1990 to 2011, road miles increased only 5% while the number of vehicle miles traveled has increased by more than 35% (FHWA 2013). Truck miles grew at an even faster rate, increasing by nearly 50% during the same period. Hence, agencies expect road conditions to worsen unless governments manage to close the approximately $86 billion annual shortfall needed to maintain the present performance levels (USDOT 2014). Transportation agencies rely on regular characterizations of ride quality to forecast needed resources. Increasing the frequency of roughness assessments becomes necessary when the pace of roadway deterioration accelerates (Haider, Chatti, et al. 2011). Surveys found that infrequent assessments of roughness underestimates repair costs at the network level (Haider and Dwaikat 2011).

Federal laws require that state agencies provide roughness measures for portions of the NHS and other critical roadway arterials (HPMS 2012). However, agencies cannot afford to meet those minimum requirements more than once annually because resource constraints limit the cost-effective scaling of existing methods to characterize ride quality. Consequently, important vulnerabilities such as frost heaves that appear and disappear between monitoring cycles often go undetected. Anomalies such as potholes tend to increase travel times because drivers slow down to avoid them. The identification of anomalies is critical for assessing the load-bearing capacity of any road and to estimate its remaining service life (FHWA 2010). More frequent monitoring will reduce user vulnerability to anomalies that could lead to property damages, injuries, fatalities, and chronic congestion from speed reductions.

The ability to assess frequently the performance of all roads will improve network-wide deterioration forecasts and enable the optimal timing of preservation activities and investments.

Pavement preservation strategies are most effective when applied while the pavement is still in good condition (AASHTO 2009). The timing of road surface maintenance is critical because action taken too soon could waste valuable resources, whereas action too late could result in a six- to ten-fold increase in the cost for improvements (Galehouse, Moulthrop and Hicks 2003). An effective preservation program has the potential to double the life of a pavement, which would consequently result in savings of more than three times the cost of reconstruction. As the macro model in Figure 4 suggests, asset management optimization will eventually boost the number of lane miles in good condition and simultaneously reduce the cost of maintenance. Consequently, smoother pavements will further promote economic growth. Sustaining the complex cycle of growth requires agencies to allocate resources at the optimum times to maintain or enhance network capacity. The ability to enhance network capacity through optimized maintenance practices will lead to a reduction in pavement load density.

1.2. Research Objectives

The main goal of this research is to develop a method of ride quality characterization that is compatible with the probe data from emerging connected vehicle standards. Hence, all jurisdictions will be able to afford and use the new method to monitor continually the performance of their entire network. This new ability will provide agencies with actionable and timely information to minimize risks and to enable the optimal scheduling of roadway preservation activities and investments. To achieve the goal, this dissertation will develop a statistical model of sensor data integration to produce a measure of roughness for both paved and unpaved roads. An anticipated feature of the statistical method is continual performance improvements as more vehicles participate to upload their sensor data.

The ubiquity of smartphones has lured researchers worldwide to seek ways of utilizing their embedded inertial sensors and Global Position System (GPS) receivers to produce repeatable and reliable indices of roughness. The existing approaches reported require device calibration with individual vehicles to account for differences in travel speed and suspension responses. The calibration approach is impractical to scale and manage with increasing volumes of connected vehicles. A statistical method that converges as data volume increases will obviate the need for calibration. Hence, this research will develop a method to integrate the data from multiple heterogeneous sensors aboard vehicles to characterize ride quality by producing a single-index summary of road roughness. A further goal is to determine a computationally simple method of combining the ride quality indices from many vehicles to produce an objective and consistent quantification of roughness for any length of road segment. The following is an outline of the research objectives:

1. Develop a model to characterize ride quality by transforming the heterogeneous sensor data from connected vehicles
2. Develop a method to combine the ride quality characterizations from a large volume of vehicles to produce a single index summary of roughness for any length of road segment
3. Develop the method of sensor data integration and compression to be computationally simple so that implementations will be practical and suitable for real-time applications
4. Evaluate the performance of the sensor data integration and compression models with practically achievable data volume
5. Relate the new roughness index to the prevailing index, which is the International Roughness Index (IRI)

6. Identify an approach to extend investments in the IRI datasets by relating them to the new roughness index
7. Identify properties and behaviors of the new models relative to those of the IRI
8. Identify the best setting for the inertial sensor sample rate
9. Identify the best setting for the GPS receiver update rate
10. Determine the impact of sensor and vehicle parameter variations on the precision and accuracy of forecasting pavement deterioration
11. Determine how variations in sensor characteristics and vehicle suspension parameters would affect the precision and accuracy of anomaly localization

Implementing these objectives will require the development of software to simulate the behavior of the models under a variety of circumstances, and to process the data from each case study. The appendix contains a description of the main algorithms.

1.3. Scope and Method of Research

Agencies evaluate pavement performance using a wide variety of tools that range from recording visual inspections on paper to the use of sophisticated instrumentation aboard probe vehicles. Visual inspection practices use a variety of standard procedures and ratings, such as the Present Serviceability Rating (PSR) to "judge the ability of a pavement to serve the traffic it is meant to serve," but such subjective methods are inconsistent (Al-Omari and Darter 1994). Unlike visual inspections, probe vehicles produce objective and consistent data. This dissertation will focus on objective methods of estimating road roughness through ride quality characterizations.

The method will involve developing a base model for the sensor data integration – the Road Impact Factor (RIF) transform. That is, a mathematical transformation of the time, inertial,

and geospatial position from each vehicle will produce a single-index summary of roughness for any segment of road. The RIF-transform isolates the factor in roughness generation to unevenness of the road surface. Related work that is outside of this research scope will incorporate other factors that produce roughness, such as variations in the longitudinal and lateral motions, to characterize the condition of railroad tracks and equipment. The average RIF-index from all roadway vehicle traversals, within some predetermined interval of time, will be the summary of roughness for a road segment of a given length.

The next chapter will summarize the history of instrumented vehicles and the state-of-the-art. This background will highlight the progression of studies conducted and issues resolved to result in the prevalence of the IRI. The chapters following will provide a detailed derivation and assessment of the IRI to highlight its benefits and to uncover the underlying principles for limitations reported. The introduction of a parameterized bump model and a review of the IRI quarter-car suspension model will provide an analytical framework to study the behaviors of each transform. The framework will facilitate simulations to demonstrate how different vehicles will respond to a range of bump height and width when traveling at different speeds. The RIF-index and IRI computed from the simulated vehicle responses under identical conditions of roughness will provide a relative comparison of their behaviors. The insights gained will explain how the RIF-index is proportional to the IRI at a standard speed and yet represent the actual ride quality experienced at any speed. Analysis of the vehicle responses in both the time and frequency domains will provide different perspectives for understanding their characteristics and utility.

With limited access to connected vehicles, the case studies for this research will utilize regular vehicles with onboard electronic devices such as smartphones that already integrate the

relevant sensors. The case studies will incorporate vehicles of different types to assess the statistical behaviors of the models. The first case study will utilize an Inertial Profiler vehicle to collect data simultaneously to compute both the IRI and the RIF-index. This approach will validate the RIF/IRI proportionality relationship derived. Smartphones aboard regular vehicles and multiple traversals of the same segment will provide the case study data to validate the model performances for different levels of roughness observed.

Blindly selecting the maximum sensor update rate available would result in an unnecessarily large amount of data that each vehicle sensor must log in its available memory for subsequent wireless transmission. Therefore, the analysis will include a derivation of the minimum accelerometer sample rate and the minimum GPS update rate needed. Additional case studies with different sensor settings will validate the update rate selections.

The study will finally apply the new models to assess their performances in two key applications: pavement deterioration forecasting and automated anomaly localization. A sensitivity analysis of the RIF-index with respect to variations in vehicle suspension behavior will provide precision bounds for the deterioration forecasting. Similarly, a sensitivity analysis of the localization accuracy as a function of GPS receiver, suspension transient responses, and other factors will provide precision bounds for the method anomaly localization. Both analyses will incorporate case study data to validate the expected statistical behaviors that characterize tradeoffs in precision with achievable data volume.

1.4. Research Contributions

Currently deployed methods of ride quality characterization are relatively expensive, slow, and complex. Hence, their frequency and span of use is limited. The RIF-transform will break through these long-standing limitations by producing continuous assessment of roughness

for the entire network. Research to identify all possible benefits of the USDOT connected vehicle initiative has focused mainly on ways of using vehicle-to-vehicle (V2V) communications to prevent crashes, and vehicle-to-infrastructure (V2I) communications to enhance mobility and reduce polluting emissions in congested corridors (USDOT 2012). No other research has defined an approach to leverage the convergence of statistics from a large volume of connected vehicle data to characterize ride quality (Bridgelall 2014).

Previous attempts to estimate the IRI from inertial sensors aboard regular vehicles found that such techniques require calibration with individual vehicle responses at a fixed speed (Dawkins, et al. 2011), (Ndoye, et al. 2011), (Chen, Lu, et al. 2011). The convergence of an average RIF-index from the transformation of a large data volume will obviate the need for calibration. Existing probe vehicles produce the IRI from single vehicle traversals. The IRI derived from one traversal is not a statistically significant estimate of the roughness of a road segment. Bernoulli's Theorem (Papoulis 1991) posits that the average RIF-index from a large volume of vehicle traversals will provide a more accurate and precise representation of ride quality than the IRI. This dissertation will further derive a direct proportionality relationship between the RIF-index and the IRI. Direct proportionality will allow the RIF-transform to extend investments in IRI datasets through simple scaling.

This research will provide new insights to explain numerous IRI deficiencies reported by demonstrating its behavior relative to the RIF-index in both the time and frequency domains. The IRI is undefined for speeds besides 80 km/h (Gillespie, Sayers and Queiroz 1986). This constraint limits use of the IRI in urban environments with interrupted traffic flows. Consequently, agencies seldom use the IRI to assess the roughness of interrupted flow facilities. Furthermore, laser-based Inertial Profilers that measure the elevation profile of paved roads tend

to overestimate the roughness from unpaved roads. As a result, highway agencies do not use such instrumented approaches on unpaved roads. Nevertheless, interrupted flow facilities and unpaved roads account for more than 90% of the roadways in the United States. Unlike the IRI, the RIF-transform will be applicable for all facility types and at all speeds.

The IRI is a summary of the roughness that a *fixed* quarter-car produces from the *simulated* traversals of a digitized *replica* of the elevation profile. Therefore, the IRI does not reflect the true roughness that vehicle occupants experience when traveling in vehicles with different suspension characteristics and at speeds different from 80 km/h. The analysis will demonstrate how a vehicle's response to spatial wavelengths of the road's longitudinal profile will vary with suspension characteristics and speed. In fact, numerous studies demonstrated that the IRI masks road roughness that causes human discomfort (Ahlin and Granlund 2002), (Papagiannakis 1997), (Lak, Degrande and Lombaert 2011). The IRI is also insensitive to spatial wavelengths that are characteristic of underlying pavement distress symptoms (Ramji, et al. 2004), (Walker, Fernando and Sho 2005), (Loizos and Plati 2008), (Múčka and Granlund 2012). Conversely, the RIF-transform will be applicable at any speed. The RIF-index will represent the actual roughness that users experience rather than a simulated roughness. This research will further develop a time-wavelength-intensity-transform (TWIT) by integrating RIF-indices from multiple speed bands to produce a speed-independent and wavelength-unbiased roughness index. Therefore, the TWIT will represent the average roughness experienced for the range of speeds that vehicles travel the segment.

Several studies have applied heuristics or machine learning techniques to detect potholes from the inertial data of individual vehicle traversals (Mohan, Padmanabhan and Ramjee 2008), (Silva, Perera and Perera 2008), (Eriksson, et al. 2008), (Tai, Chan and Hsu 2010), (Chen, Zhang

and Lu 2011), (Hautakangas and Nieminen 2011), (Mednis, et al. 2011). However, none of those studies characterized the spatial localization accuracy as a function of variations in vehicle volume, speed, sensor, and suspension parameters. This research will determine the precision bounds of anomaly localization when using a multi-resolution feature of the RIF-transform.

The methods developed in this research will enable cost-reduced decision support platforms with enhanced precision and accuracy to forecast the resource needs for all roads. The inherently higher frequency of ride quality reporting will enable more effective and predictive maintenance practices. A case study of the model application will determine the precision bounds in forecasting deterioration as a function of the available traversal volume for a segment. Unlike the IRI, the multi-resolution features of the RIF and the TWIT will provide high spatial resolution to localize anomalies that could be symptoms of pavement distress or safety hazards. A case study will demonstrate how agencies would utilize the multi-resolution feature to identify and catalog anomalies that would require urgent attention.

Ultimately, the widespread use of the wavelength- and speed-unbiased TWIT will result in optimized asset management practices that extend the lifecycle of pavements and minimize expenditures. Agencies worldwide will be able to use the models developed to deploy practical and affordable solutions that will provide many-fold savings in pavement preservation activities.

1.5. Organization of the Dissertation

Chapter 1 provides an overview of the dissertation, the research objectives, the scope, key contributions, and the organization of its main sections. Chapter 2 summarizes the history and background of pavement performance measures, the challenges of using the prevailing methods, and the emerging opportunities to mitigate their shortcomings using the new models. Chapter 3 establishes the analytical foundation and derives the new models. Chapter 4 explores the relative

behaviors of the IRI and RIF-transforms, proves the direct proportionality relationship, and provides a case study for validation. Chapter 5 analyzes the sensitivity of the models to sensor and vehicle parameter variations and provides case studies to validate the best settings for the inertial sample rate and the GPS update rate. Chapter 6 assesses how variances in sensor and vehicle suspension parameters affect the precision of models that use the RIF-index to forecast pavement deterioration. The associated case study illustrates the practical tradeoff in precision as a function of data collection days. Chapter 7 demonstrates the multi-resolution feature of roughness localization, characterizes the accuracy of its position estimate with respect to variations in sensor and vehicle suspension parameters, and illustrates application of the model through several case studies. Chapter 8 summarizes the theories developed, reviews the research questions answered, and highlights the primary benefits and contributions. This final chapter also identifies limitations of the models and future research to address them.

CHAPTER 2. PAVEMENT RIDE QUALITY CHARACTERIZATION

This chapter provides an overview of the background and history of pavement condition assessment. The focus is on objective methods of ride quality characterizations. A review of the literature exposes current challenges and limitations of the prevailing methods. An assessment of the connected vehicle environment highlights emerging opportunities for new statistical methods to leverage the voluminous data flows from connected vehicles.

2.1. Background and History

Pavement condition assessment is a broad term that involves a wide variety of characterizations. Measures of condition include geometric design and surface material characteristics that affect the overall roadway level of service (LOS). The volume-to-capacity (V/C) ratio and the traffic density typically determine the roadway LOS (HPMS 2012). The volume of vehicles through a segment is the product of the average speed and the traffic density. Hence, the LOS must change when drivers slow down to navigate safely through rough segments. The Federal Highway Administration (FHWA) long recognized that "roughness is widely regarded as the most important measure of pavement performance" because it is the characteristic that is most evident to the traveling public (Perera, Byrum and Kohn 1998). State agencies use roughness indices as acceptance criteria for the quality of new pavements and surface treatments. Roughness levels are also important metrics that agencies rely on to forecast and prioritize preservation activities, and to create or enforce policies based on objective decision-making.

From the earliest times of the first paved roads, society developed devices to produce objective, consistent, and repeatable measures of roughness. Tools have evolved from simple hand-held devices such as straightedge levels to sophisticated onboard computers and lasers that

can measure elevation profiles at highway speeds. Prior to the 1900s, the sliding straightedge, called a Viagraph, was one of the first devices invented to measure roughness. It recorded the vertical deviations of a center piston (Hveem 1960). The Viagraph was the only instrument available until 1922 when the State of Illinois invented the Profilometer. It was essentially a straightedge on wheels. All straightedge type devices measure the depths below peaks of the roadway that touch the base of the device as it slides along the surface. Hence, measurements with such devices are slow and tedious.

Road roughness affects the ride quality that vehicle occupants experience. With the introduction of faster moving vehicles, agencies soon became aware that motorists were more concerned with ride quality than actual profile roughness. Around 1926, the State of New York developed the Via-Log to measure roughness. A stylus mounted to the front-axle recorded its movements relative to the body of the vehicle by marking its relative position on a turning roll of paper. Manufacturers later implemented the same concept in different ways through a combination of mechanical and electronic methods. Thereafter, practitioners named the category response-type road roughness measuring systems (RTRRMS). For repeatable measurements, manufacturers introduced trailers with standardized mass-spring suspensions such as the Bureau of Public Roads (BPR) Roughometer introduced in 1941, and the Mays Ride Meter introduced in the 1960s. Soon thereafter, agencies discovered that the mechanical filtering action of a vehicle's suspension masked some of the RTRRMS roughness indicators that straightedge devices would normally report. This discrepancy led to additional investigations for improved methods.

During the early 1960s, the General Motors Research Laboratory (GMRL) produced the first contactless, high-speed device that incorporated basic principles of the straightedge

(Spangler and Kelley 1966). Contactless depth measuring sensors replaced the center piston and the center wheels of straightedge devices. Acoustic sensors initially provided the depth measurement but manufacturers eventually replaced those with lasers in the 1990s. The GMRL device became a template for engineers to improve accuracy and reduce cost. An important shortcoming, however, was that the tire and suspension system differences of vehicles required some method of regular calibration. This challenge spurred considerable research to find the best means of calibrating roughness-measuring devices (T. D. Gillespie 1992).

In 1982, the World Bank sponsored a series of experiments in Brazil to establish standard processes for calibrating and reporting roughness measurements. This event led to the definition of the IRI. The standardizing body selected a fixed speed of 80 km/h (about 50 mph) to simulate the responses of a fixed quarter-car to the digitized elevation profile (Gillespie, Sayers and Queiroz 1986). Practitioners call this fixed quarter-car the Golden Car. In 1990, the FHWA adopted the IRI as the standard reference for reporting pavement roughness (HPMS 2012). The IRI has been the prevailing method of ride quality characterizations ever since.

2.2. Current Challenges

The American Society of Testing and Materials standard E867 (ASTM 1997) defines roughness as "the deviations of a pavement surface from a true planar surface with characteristic dimensions that affect vehicle dynamics and ride quality." Spatial wavelengths shorter than about 10 feet typically indicate top layer pavement distress (Jordan and Cooper 1989) while sub-grade problems tend to produce longer wavelengths (Doré, Flamand and Pascale 2002). The IRI and Power Spectral Density (PSD) are the two most widely utilized indices for characterizing roughness. Unlike the PSD, it is not possible to measure the IRI directly from the pavement profile. The IRI is the cumulative absolute difference between the sprung- and unsprung-mass

rates of the Golden Car (T. D. Gillespie 1981). The simulation produces the two mass motion rates by moving the Golden Car model at the fixed reference speed across the sampled elevation profile. The IRI is sensitive to the sample interval selection. Therefore, the profiling equipment must carefully regulate the traversal speed of the vehicle to maintain a relatively constant sample interval. Consequently, the stop-and-go conditions of urban roads present significant challenges for road profiling equipment that must maintain a relatively constant speed (Janoff 1990).

The Golden Car model is essentially a mechanical filter. Therefore, it emphasizes vibration energy of wavelengths near the modal resonances and attenuates energy that falls outside of the frequency pass-band. This filtering action results in wavelength biases that mask some distress symptoms (Marcondes, et al. 1991). Studies show that the IRI is not a unique representation of pavement condition because different wavelength compositions can produce the same IRI (Mann, McManus and Holden 1997). To compensate for these deficits of the IRI, some practitioners compute the PSD to attempt detection of underlying or developing faults. A PSD decomposes the spatial profile into an intensity spectrogram of wavenumbers that are in units of cycles per meter (Davis and Thompson 2001). Computing the PSD requires sample sequences of at least one kilometer of the elevation profile (ISO 8608 1995). This requirement makes the PSD impractical for localizing distress symptoms within a few meters (Perera and Kohn 2005).

To provide an alternative to the IRI, the ISO 8608 standardized a single number summary of roughness that is the intercept of a linear fit to the log-log PSD slope. However, this method is a gross approximation of roughness because it incorrectly assumes that the road profile is a stationary stochastic process (Delanne and Pereira 2001). Hence, agencies use the PSD less often than the IRI for network level roughness characterizations.

Nearly all jurisdictions now use Inertial Profilers to produce the IRI and the PSD from measurements of the elevation profile (The Transtec Group 2012). These vehicles integrate a laser and position sensitive light sensor to measure the elevation profile while traveling at highway speeds. Although standards have since been in place to specify their functionality and performance (AASHTO 2010), Inertial Profilers differ in the quality of the data that they report (Ksaibati, et al. 1999), (Dyer, Boyd and Dyer 2005). Specifically, samples of the profile include vehicle body bounces that distort the reference plane needed to determine the correct vertical distance to the pavement surface. Attempts to estimate and remove reference plane bounces by double integration of the signal from a body-mounted accelerometer often result in added distortions because of variable initial conditions, speed changes, and electromagnetic noise (Janoff 1990). Without an effective method of proper reference plane normalization, roughness from objects such as lane dividers and manhole covers produce body bounces that could invalidate miles of collected data (Walker, Fernando and Sho 2005), (Dyer, Boyd and Dyer 2005), (Wang, Birken and Shamsabadi 2014). At the time of this writing, the Transportation Research Board (TRB), National Cooperative Highway Research Program (NCHRP 2013) is conducting research to address these shortcomings of Inertial Profilers.

2.3. Emerging Opportunities

Research groups predict that by 2020, organizations worldwide will collect and process 30 terabytes of data each day from more than 150 million connected vehicles (Boyadjis 2013). The ubiquity of smartphones, wireless hotspots, cloud computing applications, and Big Data analytics has already established a practical framework to implement and use the models that this research developed. The existing connected vehicle framework incorporates sensors aboard fleet vehicles such as postal and freight carriers, utility and law-enforcement vehicles, and public

transit. These vehicles currently communicate with various decision support platforms to enable a wide variety of business processes.

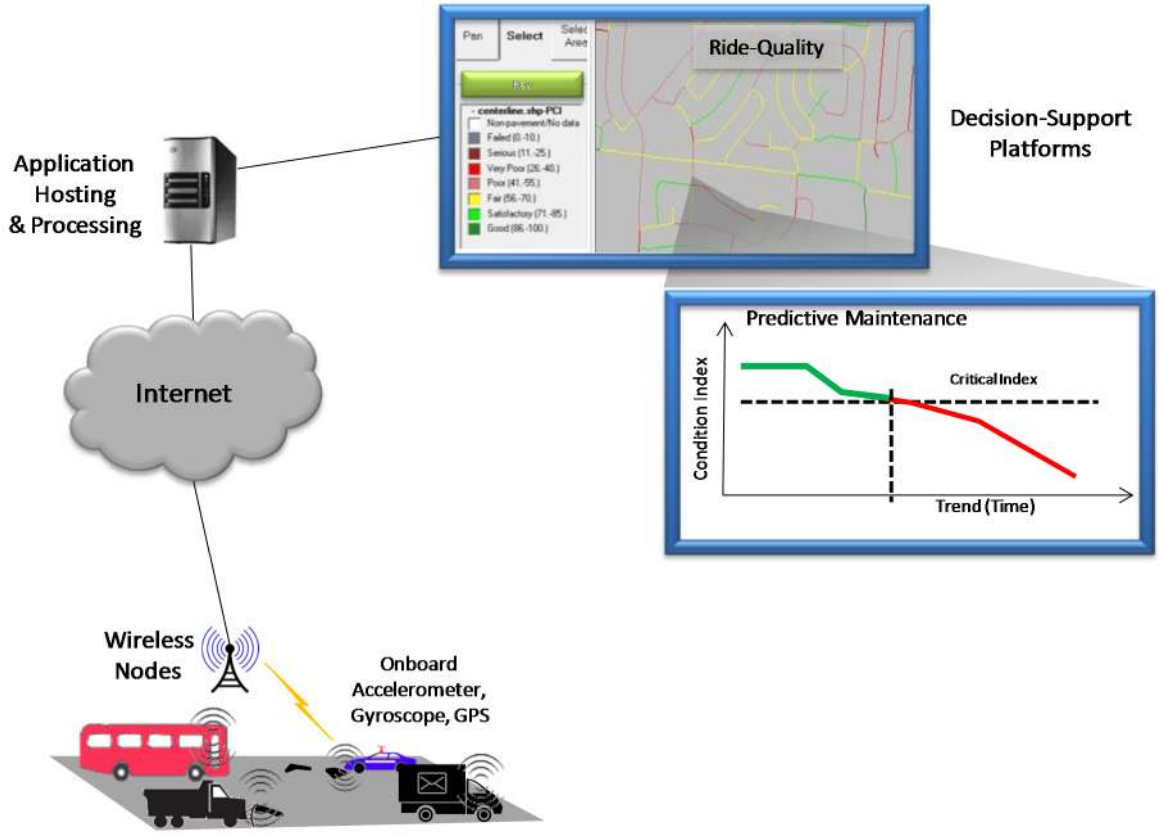

Figure 2. The existing connected vehicle framework

The USDOT roadmap indicates that connected vehicle pilot deployments will conclude by 2020 and transition to full deployment for all vehicles soon thereafter (USDOT 2014). Figure 2 illustrates the overall framework for existing and emerging connected vehicles. Nearly all vehicles integrate accelerometers to provide the signals needed for critical safety functions such as airbag deployment and vehicle dynamics control. Much of these types of data are currently isolated to the vehicle system bus. One of the main objectives of the connected vehicle initiative is to standardize the approach of transmitting this and other sensor data via wireless means. The majority of the onboard GPS receivers are currently aftermarket devices. Nevertheless, the persistent consumer demand for safety, security, comfort, and convenience will

result in their integration as standard features of regular vehicles for navigational guidance. The market for embedded automotive sensors such as accelerometers and GPS receivers was more than $18 billion in 2014. Analysts predict that the market will reach $30 billion by 2020 (Industry Experts Group 2013).

Mandates to improve fuel economy, reduce emissions, and improve safety through V2V communications has spurred the development of regulations and policies to standardize the wireless link and message formats for vehicle probe data. The USDOT selected dedicated short-range communications (DSRC) as the standard for V2V communications. The DSRC standard will naturally extend to V2I communications (NHTSA 2011), (NHTSA 2014). The SAE J2735 standard, produced in part to support the USDOT connected vehicle initiative, prescribes the format for transmitting the relevant onboard sensor data to remote host computers (CAR 2013). The USDOT has already modified the National ITS Architecture to include inertial and location data in the standard message set of its "roadway hazard warnings" service package with the explicit purpose of enabling applications such as pothole detection (USDOT 2014).

The growing availability of vehicle probe data has raised issues involving ethics, security, and privacy (Christin, et al. 2011). The concept of connected vehicles has also led to early concerns about computing resource availability and the capability of existing systems to process such large volumes of data (Leduc 2008). Nevertheless, the growing popularity of Big Data science and engineering has stimulated rapid advancements in computing infrastructure, feature extraction methods, and machine learning techniques to satisfactorily address those issues (Wang and Ku 2012), (Cristofaro and Soriente 2013). Travel advisory applications and in-vehicle navigation systems from providers such as TeleAtlas (TomTom), Here.com (Nokia), Apple Maps (Apple Inc.), and Waze (Google Inc.) now automatically update maps by mining data from

roaming cellular phones (Cohan 2013). Organizations are now routinely mining vehicle probe data to improve fleet safety and operating efficiency (Verizon 2014), to assess environmental impacts (NREL 2014), and to guide transportation planning (NCHRP 775 2014). The USDOT has been promoting technical and policy advancements that will lead to the ubiquitous exchange of vehicle probe data (USDOT 2014). Hence, the performance of methods developed in this dissertation will improve continuously as connected vehicle data become widely available.

CHAPTER 3. MODEL DEVELOPMENT

The literature search of this chapter summarizes existing models of profile roughness that are suitable for analysis and simulation. The lack of analytical models of roughness created the need to develop a bump model to characterize roughness in both the time and frequency domains. The new model provides an ability to sweep bump height and width to reveal how specific characteristics of the vertical acceleration energy would produce different vehicle responses. Functional definitions of the vehicle and sensor response models provide a framework to derive the IRI and to assess its behavior as a function of bump dimensions and vehicle speeds. The insights gained shape the definition of the RIF-transform. The theories developed identify and explain the proportionality relationship between the RIF-index and the IRI. The case study includes a detailed description of the data, their processing, and the method of transformation to RIF-indices.

3.1. Literature Review of Roughness Models

Vehicle manufacturers use random and deterministic models of bumps to study suspension system performance and vehicle responses to road roughness. Both types of models adequately simulate road conditions to characterize their roughness. Whereas roughness simulation models produce profile roughness, roughness characterization models summarize the ride quality from either simulated or actual road profiles. The next sections summarize the evolution of available roughness simulation and roughness characterization models.

3.1.1. Roughness simulation models

The most common random models of road profiles are Gaussian processes (Dodds and Robson 1973), Markov processes (Waechter, et al. 2003) or triangular series with random cosine components (Sun 2003). Researchers are aware that such models cannot reproduce the elevation

profile of an actual road but use them nonetheless to analyze possible vehicle fatigue from road roughness (Robson 1979). Models based on random Gaussian processes do not generally account for road irregularities that cause most of the vehicle fatigue damage (Bogsjö 2007).

Deterministic bump models provide a more controlled approach to the design optimization of artificial road bumps such as those used for traffic calming. These types of models allow direct control of their parameters to observe the effects on vehicle responses at different speeds. Researchers typically model individual bumps as conical or rectangular structures that are either concave or convex with respect to the surface (Oke, et al. 2007). A recent study proposed a non-rectangular form that includes a circle protruding above a flat surface (Garcia-Pozuelo, et al. 2014). However, expressions involving partial circles do not produce analytic functions because of their discontinuities. Hence, it is not possible to create closed form expressions of slope profiles by continuous differentiation. This research demonstrates how combinations of modified Gaussian radial basis functions with randomized parameters produce roughness simulation models that are analytical.

3.1.2. Roughness characterization models

The AASHTO road test conducted from 1956 to 1961 in Ottawa, Illinois resulted in the definition of a present serviceability index (PSI) as the first single-number summary of pavement roughness (Carey and Irick 1960). The researchers defined the PSI as a regression relation between the output of a roughness-measuring device and the average ratings of ride quality from a panel of observers. The state-of-the-art roughness-measuring device at the time was a BPR Roughometer. Its output was "slope variance" (SV), which is the variance of the profile height differences between measurements taken every foot of travel (Carey, Huckins and Leathers 1962). Purdue University researchers found that the SV provided excellent correlation with

panel ratings for rigid pavements. However, the SV was a poor predictor of ratings for flexible pavements (Nakamura and Michael 1963). Other Purdue University researchers soon repeated roughness characterization experiments by incorporating a brick-sized accelerometer strapped to the chest of a driver. They defined an accelerometer roughness index (ARI) as a scaled accumulation of the rectified accelerometer signal for T seconds where

$$ARI(T) = \frac{10^4}{T}\int_0^T |g_z(\tau)|d\tau \quad (1)$$

and $g_z(\tau)$ is the accelerometer output as a function to time τ. Using ARI at fixed speeds improved predictions for the panel rating of flexible pavements conditions but still did not match the predictability for rigid pavements (Wermers 1962). The Kentucky Department of Highways (KDOH) repeated the ARI experiments at different speeds. They found that the ARI was nonlinear with speed and that the indices for flexible and rigid pavements were uncorrelated (Rizenbergs 1965). Since then, researchers conducted numerous studies to determine correlations between user perceptions of roughness and objective measures of roughness that various devices would produce. For example, researchers found that the root-mean-square vertical acceleration (RMSVA) obtained from a Mays Ride Meter, which is the difference between adjacent slope measurements, was useful in equipment calibration, but unreliable as a predictor of panel ratings (Hudson, et al. 1983).

Generally, the lack of agreement between various roughness measuring devices circumvented the definition of a uniformly accepted single-index characterization of roughness until the World Bank experiment in 1982 defined the IRI (Gillespie, Sayers and Queiroz 1986). A Washington State Department of Transportation (WSDOT) study concluded that the IRI was the single best predictor of driver-perceived road roughness and driver acceptability (Shafizadeh, Mannering and Pierce 2002). However, other researchers cautioned against using the IRI by

demonstrating that profiles with distinctly different roughness features can produce the same IRI (Kropáč and Múčka 2005). Agencies worldwide found that the IRI masks wavelengths that produced roughness for both local roads and highways (Brown, Liu and Henning 2010).

As an alternative to the IRI, some transportation agencies use a single-index summary of roughness derived from a regression fit of the PSD. That is, given the spectral density $S_H(\Omega)$ where

$$S_H(\Omega) = C_H \Omega^{-w_v} \tag{2}$$

is a regression to the PSD, the "degree of unevenness" is defined as C_H and "the waviness" as w_v. The ISO 8608 standard specifies the roughness index as C_H within the angular frequency limit of $2\pi/90 \le \Omega \le 2\pi/0.35$ radians/meter and a waviness value of $w_v = 2$. However, numerous authors indicated that the PSD roughness index is an oversimplification. They demonstrated that the waviness factor varies widely in practice from about 1 to 4 depending on where the measurement is taken (Brown, Gerz and Sulten 1991), (Andrén 2006), (Kropáč and Múčka 2009). The simplicity of the model has nevertheless led to its widespread use in vehicle suspension development. Manufacturers are now investigating more complex vehicle responses by extending the PSD model to include data from both wheel paths (Johannesson, Podgórski and Rychlik 2014).

Researchers revisited the ARI in the late 1980s to provide a more sensitive indicator of truck operating costs and cargo damage than the IRI (Todd and Kulakowski 1989). Studies found that the sprung-mass vertical acceleration was the largest contributor to the dynamic axle loads that heavy trucks generate (Papagiannakis 1997). Consequently, researchers proposed a new index based on the PSD of the sprung-mass vertical acceleration of a reference quarter-truck. The reference speed and segment length was 80 km/h and 0.5 km, respectively. The truck

roughness index is the square root of the area under the PSD from zero to 50 Hertz. The researchers found that the new index is uncorrelated with the IRI.

The seemingly unbounded increase in performance levels and cost reduction of smartphones has continually enticed researchers to revisit techniques that involve transformations of the accelerometer data to produce single indices of roughness. However, the findings continue to demonstrate that unless calibrated with the responses of individual vehicles at fixed speeds, correlation with the IRI remains poor. Transformations of the smartphone accelerometer signal include the root-mean-square (RMS) (Dawkins, et al. 2011), the full-car vibration power (Katicha, Khoury and Flintsch 2015), the Fourier Transform magnitude (Douangphachanh and Oneyama 2013), the magnitude weighted Short-Time Fourier Transform (Yagi 2013), and linear regression of the power spectral density (Du, et al. 2014). As the need to calibrate transformations of the accelerometer data from individual vehicles does not provide any substantial improvement over the RTRRMS methods, the IRI has prevailed as the most common representation of road roughness. In fact, many proposals for new indices involve a modification of the IRI procedure (Múčka 2015).

3.2. The Bump Model

A Gaussian radial bases function (Buhmann 2008) is continuously differentiable. It also provides a finite spatial support that is suitable for modeling the height profile $z(x)$ of a single bump as a function of the path traversal distance x such that

$$z(x) = \alpha_0 \exp\left(-\left[\xi_0 (x - x_0)\right]^2\right) \tag{3}$$

where the bump amplitude is α_0, its peak position is x_0, and its 'sharpness' is ξ_0. This theoretical development defines the approximate bump width λ as

$$\lambda = \frac{\sqrt{2\pi e}}{\xi_0} \tag{4}$$

where *e* is Euler's number, a mathematical constant that is approximately 2.71828. A linear combination of bumps with random variations in heights, widths, and positions produces a convenient model of the elevation profile along a wheel path.

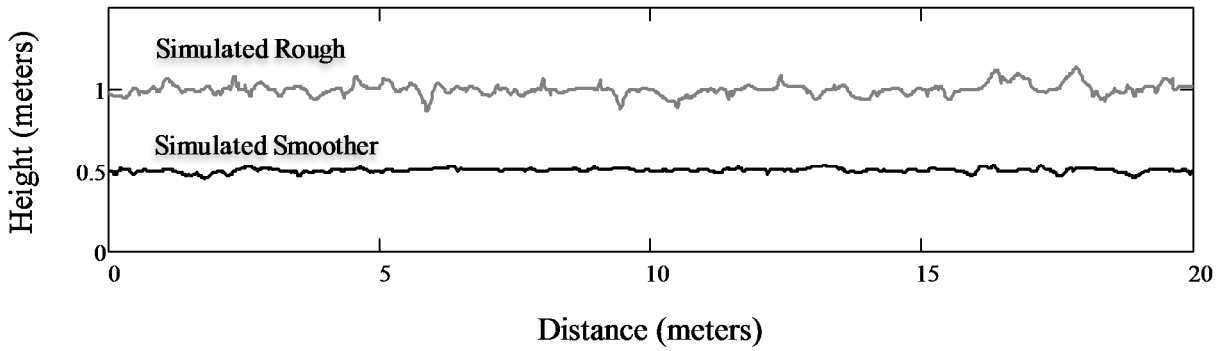

Figure 3. Elevation profile consisting of a random combination of bump functions

Figure 3 plots two simulated profiles by combining the bump functions defined in Equation (3) with randomized parameters. This simulation distributes the bump positions uniformly but distributes the bump heights and widths normally. Adjusting the amplitude parameter produces profiles with varying roughness intensities. The plots offset the simulated rough and smoother profile for clarity. Each cross section exhibits the characteristic micro- and macro-textures of a real profile that provide tire grip and roadway drainage, respectively. Hence, the simulation need not add holes to the profile because the random combination of bumps naturally results in simulated holes as well. Rather than using random profiles, the analysis will adjust the model parameters in a uniform manner to provide insights into the relative effects on ride quality.

3.2.1. Vertical acceleration potential energy

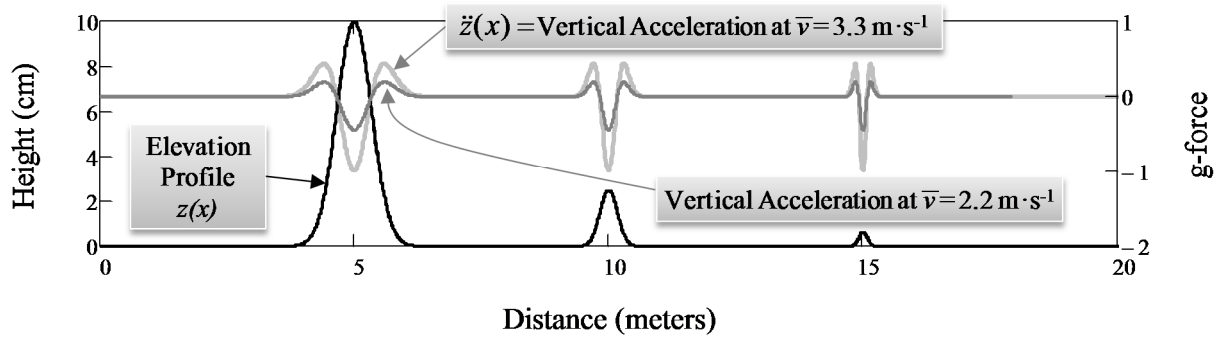

Figure 4. Bump elevation profile and vertical acceleration at different speeds

Ride roughness is directly proportional to the g-forces produced when bump traversals at any speed transforms potential energy to kinetic energy. Figure 4 plots an example of the elevation profile for three bumps with different dimensions. The first, second, and third bumps are positioned at 5, 10, and 15 meters, respectively. The height and width of the first bump is 10 centimeters (cm) and 2 meters, respectively. Progressively decreasing the widths and heights of the bumps by one-half and one-quarter, respectively, produces the same peak vertical acceleration when traversing them at the constant speed $\bar{v}$. Hence, reporting some aspect of the signal magnitude such as the peak or the average value of the inertial sensor output will mischaracterize the true nature of the elevation profile. This explains the main deficiency of the ARI or variants such as the RMS that researchers tend to explore. The vertical acceleration shown is in units of g-force with $\ddot{z}(t)/g = \ddot{z}(x/\bar{v})/g$ where $\ddot{z}(t)$ is the second derivative of the temporal elevation profile and g is the unit of standard gravity defined as 9.81 m·s^{-1}. Bump traversals at any speed causes the spatial elevation profile to produce kinetic energy. Therefore, the potential of bumps to produce kinetic energy from traversals at a speed $\bar{v}$ is their potential energy E_{pv} where

$$E_{pv} = \frac{1}{g}\int \left|\ddot{z}(t)\right|^2 dt = \frac{1}{g}\int \left|\ddot{z}(x/\overline{v})\right|^2 dx. \tag{5}$$

The plots of Figure 4 further compares g-forces produced at two average speeds. Increasing the speed by 50% from 2.2 m·s^{-1} to 3.3 m·s^{-1} doubles the peak g-forces produced. This explains the speed sensitivity of the ARI and similar methods reported.

In general, to produce the same peak g-forces at a fixed speed, a narrower bump must also be shorter by a factor that is equal to the square of the width reduction factor. For example, a bump that is one-half as wide must also be shorter by (½)^2 = ¼ to produce the peak g-force level of the wider bump. By extension, given identically tall bumps traversed at a fixed speed, the narrower bumps will produce exponentially greater g-forces.

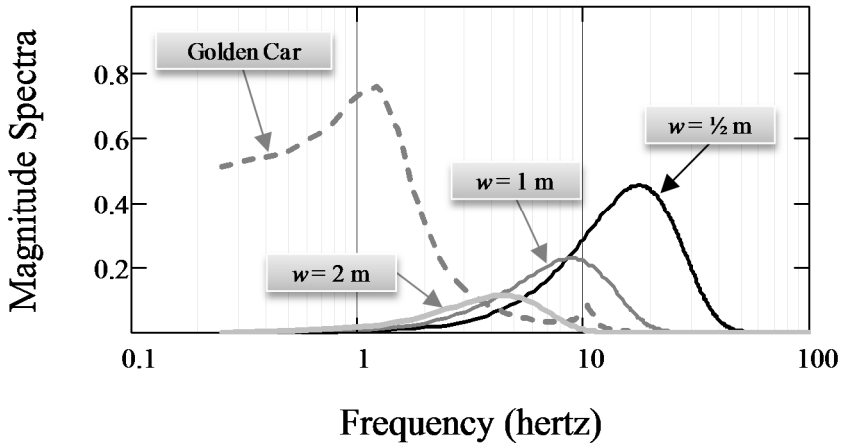

Figure 5. Bump vertical acceleration and Golden Car response spectra

To illustrate the square-law relationship, Figure 5 plots the Discrete Fourier Transform (DFT) of the g-forces produced from simulated traversals at 3.3 m·s^{-1} across equal height 10 centimeter bumps of widths w = 2, 1, and ½ meter. The narrower bump produces a peak g-force that is greater by the square of the amount of width reduction. For example, the second bump is a factor of two narrower than the first. Therefore, the second bump increases the peak g-force produced by a factor of four. The theoretical basis for this square-law relationship becomes

evident when applying the second derivative rule to the bump profiles. That is $\ddot{z}(\beta_v \cdot x) = \beta_v^2 \cdot z(\beta_v \cdot x)$ where β_v^{-1} is the width reduction factor of the bump.

The DFT of the identically tall bumps with decreasing widths illustrate how their potential energy distributes spectrally, relative to the response sensitivity of the Golden Car. The potential energy of each bump is equivalent to the areas under their respective Fourier transform magnitude shown (Oppenheim and Schaefer 1975). By inspection, the narrower bumps have higher potential energy than the wider bumps.

3.2.2. Vertical acceleration kinetic energy

Bump traversals convert potential energy to kinetic energy when the forces acting on the wheel contact area produce a vertical acceleration. The wheel suspension system absorbs a portion of the kinetic energy and dissipates some of it as heat in the suspension dampers, and as acoustic vibrations that produce road noise. The resultant energy produces vehicle body-bounces that account for the roughness in ride that vehicle occupants experience.

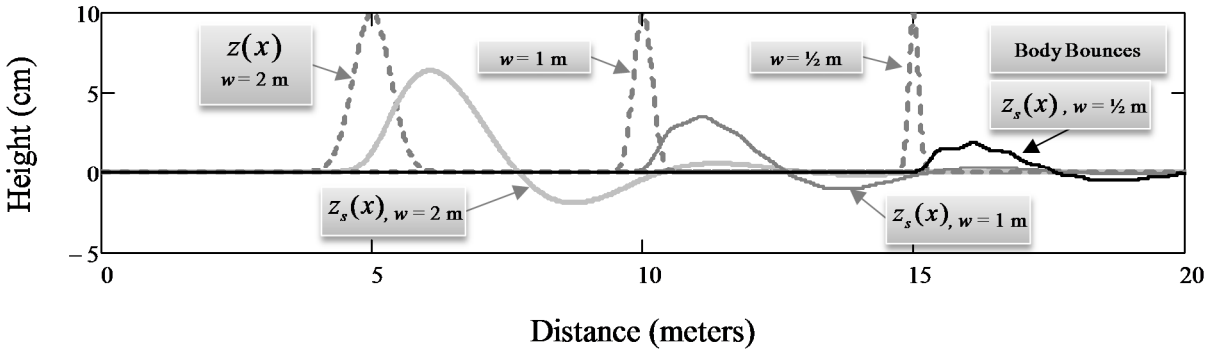

Figure 6. Golden Car responses to bumps of equal heights but different widths

The mechanical filtering action of the Golden Car attenuates bump energy that are approximately higher than 20 hertz. Figure 6 shows the transient responses of the filter for each of the bumps traversed at a constant speed of 3.3 $m \cdot s^{-1}$. As anticipated from the DFT results shown in Figure 5, the Golden Car model will progressively absorb kinetic energy as the bumps

become narrower. This result reflects the dot products of the Golden Car response spectra with the respective frequency spectra for each bump shown in Figure 5. The Fourier transform of the temporal bump profile is denoted $\Im\{z(t)\} = Z(f)$ and the frequency response of the quarter-car is denoted $Q(f)$. Therefore, the inverse Fourier transform of the product $Z(f)Q(f) = Z_s(f)$ where $\Im^{-1}\{Z_s(f)\}=z_s(t)$ produces the corresponding transient responses shown in the plots of Figure 6. The vertical acceleration from vehicle body bounces is $a_z(t)=\ddot{z}_s(t)$. Hence, the vertical acceleration kinetic energy E_{kv} is

$$E_{kv} = \int |a_z(t)|^2 dt. \tag{6}$$

The next section derives the Golden Car frequency response shown in Figure 5.

Higher traversal speeds produce the same effect as narrower bumps. This is intuitive because traveling faster across a bump decreases the time exposure to potential energy. Mathematically, reducing the bump width by a factor of β_v is equivalent to a transformation from $z(x)$ to $z(\beta_v \cdot x)$.

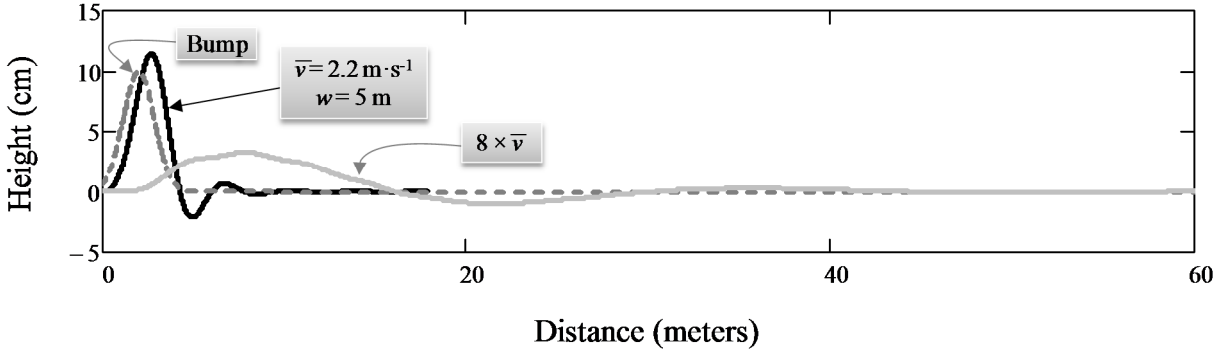

Figure 7. Golden Car sprung-mass responses to vertical acceleration at different speeds

The function becomes $z(\beta_v \cdot \bar{v} \cdot t)$ because $x = \bar{v} \cdot t$ and that is equivalent to increasing the velocity by a factor of β_v. The scaling property of the Fourier transform specifies the amount of frequency shift such that

$$\Im\{z(\beta_v \bar{v} t)\} = \frac{1}{\beta_v \bar{v}} Z\left(\frac{f}{\beta_v \bar{v}}\right). \quad (7)$$

Therefore, the potential energy of the narrower bump will spread into frequencies that are β_v higher, resulting in less response from the Golden Car. Figure 7 compares the body-bounce of the Golden Car traversing a 5-meter-wide bump at 2.2 $m \cdot s^{-1}$ and $\beta_v = 8$ times that speed. This result demonstrates the expected attenuation in transient response at the higher speed. This also explains the reason that a vehicle occupant will experience a lower intensity body-bounce when traveling across the same bumps at higher speeds, even though the potential energy from the narrower bumps is much greater (Figure 5).

In summary, given a set of suspension characteristics and a fixed speed, roughness intensity will tend to decrease non-linearly as bumps become narrower. On the other hand, roughness intensity is linearly or directly proportional to bump height because

$$\Im\{\alpha_0 \times z(t)\} = \alpha_0 \times \Im\{z(t)\} = \alpha_0 \times Z(f). \quad (8)$$

These models explain the fundamentals of how variations in bump height and width result in the roughness intensity that riders experience at different speeds. The mechanical filtering action of the Golden Car amplifies bump energy peaks that coincide with the resonant quarter-car modes, and attenuates energy that falls outside of the spectral response bandwidth. The next section will derive the quarter-car model to provide insights into limitations of the IRI that practitioners observed.

3.3. Vehicle Response Model

The standard quarter-car is a model that consists of a series connection of two mass-spring systems. Suspension engineers relate the vehicle body- and axle-bounces observed to the lumped quarter-car sprung- and unsprung-mass responses, respectively (Angeles 2011).

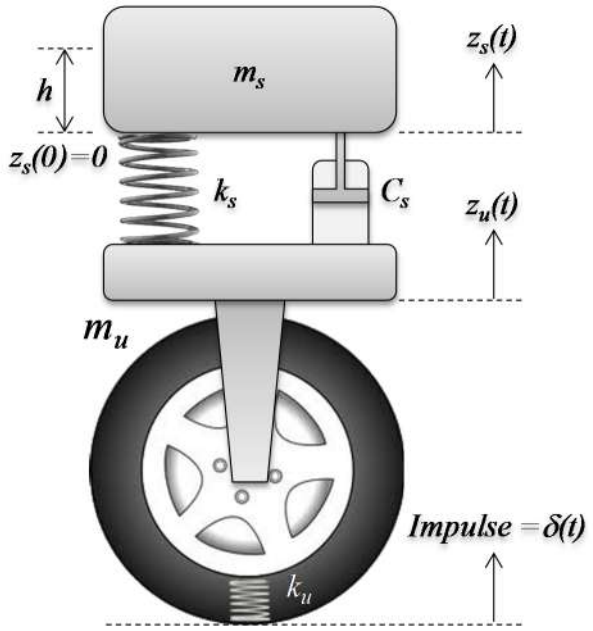

Figure 8. Damped mass-spring model of a quarter-car

Figure 8 illustrates the damped mass-spring model. From Newton's law, the vertical force $f_z(t)$ acting on the sprung-mass m_s of a damped mass-spring system is $f_z(t) = m_s \ddot{z}_s(t)$. The components of this vertical force are the downward acceleration $-m_s g$ due to gravity g, the upward resistance to vertical velocity $\dot{z}_s(t)$ with viscous damping coefficient c_s, and the upward spring force $k_s(h\text{-}z)$ with spring stiffness k_s and compression distance h. Traversing the longitudinal profile creates an upward forcing function $f_z(t)$ from the axle motion $Z_u(t)$. The sum of these forces yields the motion equation for a damped mass-spring model

$$m_s \ddot{z}_s(t) = -m_s g - c_s \dot{z}_s(t) + k_s \left[h - z(t)\right] + f_z(t). \tag{9}$$

When the system is at rest at time $t = 0$ the vertical reference plane is at $z_s(0) = 0$. Hence the equilibrium condition is

$$-m_s g + k_s h = 0. \tag{10}$$

Substituting Equation (10) into Equation (9) yields the second order, non-homogeneous linear differential equation of motion for the sprung-mass response where

$$\ddot{z}_s(t)+\frac{c_s}{m_s}\dot{z}_s(t)+\frac{k_s}{m_s}z_s(t)=\frac{1}{m_s}f_z(t). \tag{11}$$

The natural frequency of the sprung-mass system, ω_s, is defined as

$$\omega_s=\sqrt{\frac{k_s}{m_s}}. \tag{12}$$

The damping ratio, ζ_s, is defined as

$$\zeta_s=\frac{1}{2\omega_s}\frac{c_s}{m_s}=\frac{c_s}{2\sqrt{k_s m_s}}. \tag{13}$$

This expression yields a normalized model where the impulse response of the damped mass-spring system is completely described by its natural frequency and damping ratio

$$\ddot{z}_s(t)+2\zeta_s\omega_s\dot{z}_s(t)+\omega_s^2 z_s(t)=\delta_z(t). \tag{14}$$

The standard solution for the impulse response of the under-damped case with damping ratio in the range $0 < \zeta_\delta < 1$ is

$$z_\delta(t)=u(t)\frac{1}{\omega_n\sqrt{1-\zeta_\delta^2}}\exp\left(-\zeta_\delta\omega_n t\right)\sin\left(\omega_n t\sqrt{1-\zeta_\delta^2}\right) \tag{15}$$

where $z_\delta(t)$ is the impulse response, ω_n is the natural frequency of the system, and $u(t)$ is the Heaviside step function that assures causality of the model.

3.4. The Inertial Sensor Model

The inertial sensor applies a second derivative to the vertical motion signal $z_s(t)$ and produces an output voltage $g_z(t)$ that is directly proportional to the vertical acceleration $a_z(t)$. Therefore, the body-bounce $z_s(t)$ is a convolution of the quarter-car impulse response $q_z(t)$ and the elevation profile $z(t)$ such that

$$z_s(t) = \int q_z(t-\tau) z(\tau) d\tau \tag{16}$$

where

$$a_z(t) = \ddot{z}_s(t) \tag{17}$$

The sensor output is

$$g_z(t) = \frac{\gamma_g}{g} a_z(t) \tag{18}$$

The sensor constant γ_g transforms the sensed g-force (g) to a proportional voltage that scales to the dynamic range of the digital output.

3.5. The International Roughness Index

The notation for the IRI in this development is $I_{\bar{v}}^{L}$. It represents the roughness index for a segment of length L where the constant speed $\bar{v}$ is the standard reference speed of 80 km/h. The IRI is the accumulated absolute rate difference between the sprung- and unsprung-mass motion of a Golden Car such that

$$I_{\bar{v}}^{L} = \frac{1}{L} \int_0^{L/\bar{v}} \left| \dot{z}_s(t) - \dot{z}_u(t) \right| dt. \tag{19}$$

The first derivatives of the sprung- and unsprung-mass vertical motions are $\dot{z}_s(t)$ and $\dot{z}_u(t)$ respectively.

3.5.1. The Golden Car parameters

The unsprung-mass and its associated spring stiffness are m_u and k_u respectively (T. D. Gillespie 1981).

Table 1. Golden Car model parameters

Parameter	Value	Unit
k_s/m_s	63.3	s^{-2}
k_u/m_s	653	s^{-2}
c_s/m_s	6.0	s^{-1}
m_u/m_s	0.15	-

Table 1 summarizes the Golden Car parameters, normalized to the sprung-mass. The literature on IRI typically ignores the damping coefficient c_u of the unsprung-mass model. Nevertheless, a reasonable estimate would be about 15% of the sprung-mass damping coefficient (Türkay and Akçay 2008).

Table 2. Damped mass-spring parameters for the Golden Car

Parameter	Units	Sprung Mass	Unsprung Mass
Resonant Frequency (f)	hertz	1.27	10.50
Damping Ratio (ζ)	-	0.38	0.05

Applying these values to Equations (12) and (13) yields the Golden Car resonant frequencies and damping ratios summarized in Table 2.

3.5.2. The IRI speed constraint

The transient responses from simulated Golden Car traversals at the reference speed produce the sprung- and unsprung-mass motions needed to calculate the IRI. Hence, the IRI-transform produces a roughness index by simulating the transient responses of the Golden Car as it responds to the roughness of a digitized replica of the elevation profile. The simulator often includes numerical algorithms to solve Equation (11) for the transient responses before applying the transform provided in Equation (19) to calculate the roughness index. The simulator applies the fixed reference speed of 80 km/h to the longitudinal motion of the Golden Car, regardless of the speed that the Inertial Profiler obtained the samples of the actual elevation profile. Equation (5) revealed that the potential energy of elevation profiles is speed dependent.

Therefore, the IRI will not represent roughness that the elevation profile would have produced at speeds different from the reference speed.

3.5.3. The IRI wavelength sensitivity

The products of the Fourier transforms of the Golden Car sprung- and unsprung-mass impulse responses produce the Golden Car frequency response. Their Fourier transforms are denoted $\Im[z_{\delta s}(t)]=Z_{\delta s}(\omega)$ and $\Im[z_{\delta u}(t)]=Z_{\delta u}(\omega)$ respectively. Given the impulse response defined in Equation (15), their Fourier transforms $Z_\delta(\omega)$ are of the form

$$Z_\delta(\omega)=\frac{1}{\sqrt{1-\zeta_\delta^2}}\frac{1}{\omega_n^2+\left(\zeta_\delta\omega_n+j\omega\right)^2}. \tag{20}$$

This form characterizes a second-order low-pass filter with cutoff frequency at the modal resonances of the individual damped mass-spring systems.

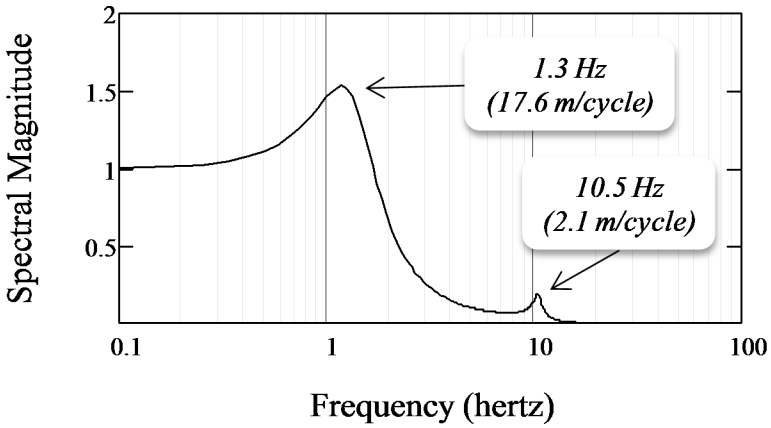

Figure 9. Golden Car transfer function

Substituting the Golden Car parameters into Equation (20) for each of the damped mass-spring systems and evaluating the magnitude of the product $Z_{\delta s}(\omega)\cdot Z_{\delta u}(\omega)$ results in the Golden Car transfer function shown in Figure 9. The response peaks at 1.3 hertz and 10.5 hertz correspond to the resonant frequencies of the Golden Car sprung- and unsprung-mass spring

systems. Hence, the Golden Car model will amplify elevation profile potential energy that is within proximity of those modes.

Traversing a road segment at a constant speed converts its spatial wavelengths in cycles per meter to temporal wavelengths in cycles per second or hertz. Traveling the same profile at different speeds will shift spatial wavelengths into and out of the Golden Car frequency response band. The mechanical filtering action of the Golden Car attenuates responses to wavelengths that are outside of its frequency response range. All quarter-cars, including the Golden Car, will produce a maximum response to spatial wavelengths that range from $\bar{v}/f_s$ to $\bar{v}/f_u$ meters where f_s and f_u are the sprung- and unsprung-mass resonance frequencies, respectively, in units of hertz. Hence, at $\bar{v} = 80$ km/h, the IRI will underrepresent spatial frequencies lower than 17.6 meters·cycle^{-1} and higher than 2.1 meters·cycle^{-1} as shown in Figure 9. Furthermore, the IRI will exaggerate roughness from wavelengths that translate to frequencies near the resonant peaks.

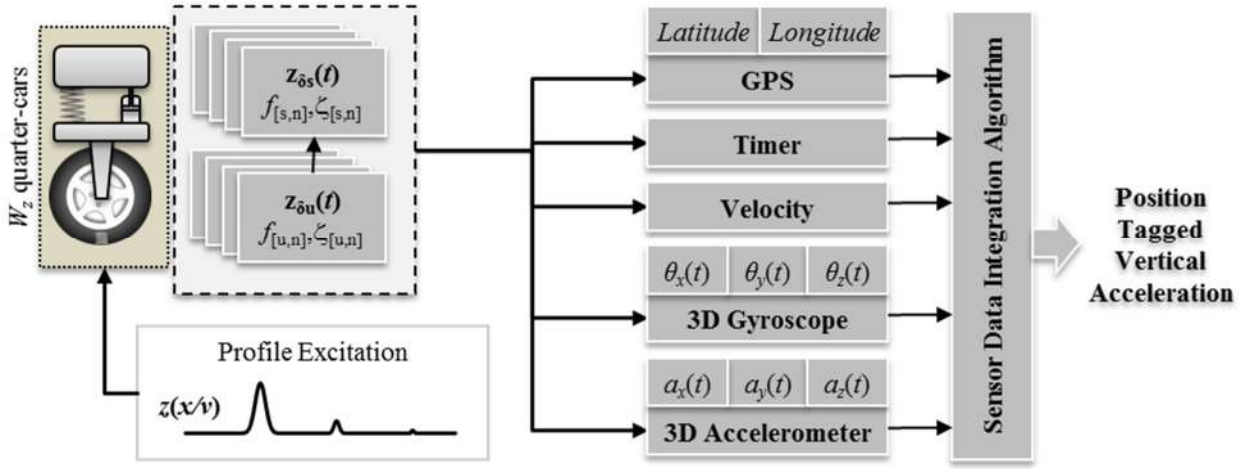

Figure 10. Operations for sensor data integration

3.6. Development of the New Transforms

This section develops a new transform to integrate the data from time, inertial, orientation, and geospatial position sensors to produce a summary index of roughness for road

segments of any length. Figure 10 illustrates the overall operation to produce a stream of position tagged vertical acceleration values that the new transform will compress into a summary of roughness.

3.6.1. The inertial response model

Nearly all modern GPS receivers provide longitudinal speed data by filtering position updates with a predictive Kalman filter (Brookner 1998). Alternatively, a speed sensor or odometer could provide the speed directly if available. The linear time-invariant (LTI) transform of Equation (16) dictates that the vertical acceleration produced from the body-bounces of each quarter-car is equivalently a convolution of the vertical acceleration $\ddot{z}(t)$ input from the wheel path and the quarter-car impulse response $q_z(t)$ such that

$$a_z(t) = \int q_z(t-\tau)\ddot{z}(\tau)d\tau \tag{21}$$

The temporal quarter-car response is the inverse Fourier transform of the transfer function product $Z_{\delta s}(\omega)\cdot Z_{\delta u}(\omega)$. Equation (20) provides the form for each transfer function. Equivalently, the quarter-car impulse response is the convolution of its sprung- and unsprung-mass impulse responses such that

$$q_z(t) = z_{\delta s}(t) * z_{\delta u}(t) = \int z_{\delta s}(t-\tau)z_{\delta u}(\tau)d\tau \tag{22}$$

where * is the mathematical convolution operator. An accelerometer mounted to the body of the connected vehicle measures the resultant vertical acceleration from each wheel-assembly as a linear combination of their quarter-car vertical acceleration responses $a_{z[n]}(t)$ at the sensor's location such that

$$g_z(t) = \frac{\gamma_g}{g}\sum_{n=1}^{W_z}\beta_{z[n]}a_{z[n]}(t) \tag{23}$$

where $\beta_{z[n]}$ are constants of the linear combination. Their values depend on the position of the sensor in the vehicle relative to each of the W_z wheel-assemblies. Hence, their proportional contributions are such that

$$\sum_{n=1}^{W_z} \beta_{z[n]} = 1. \tag{24}$$

This expression accumulates the proportional g-forces from each wheel-assembly into the resultant acceleration sensed.

3.6.2. The Road Impact Factor transform and index

The average magnitude of vertical acceleration sensed per unit length L of a road segment traveled at a constant speed $\overline{v}$ is

$$\overline{g}^{L} = \frac{1}{L}\int_{0}^{L} |g_z(x)| dx. \tag{25}$$

Applying the relationship $dx = v(t)dt$ provides an equivalent time-domain expression where

$$\overline{g}_{\overline{v}}^{L} = \frac{1}{L}\int_{0}^{T} |g_z(t)v(t)| dt = \frac{1}{L}\int_{0}^{L/\overline{v}} |g_z(t)v(t)| dt. \tag{26}$$

Parseval's Theorem (Oppenheim and Schaefer 1975) relates the frequency domain representation of the signal $G_z(f)$ to its time domain representation $g_z(t)$ as

$$\int |G_z(f)|^2 df = \int |g_z(t)|^2 dt \tag{27}$$

The left side of Equation (27) represents the area under the vertical acceleration magnitude spectra, which is the resultant kinetic energy of ride roughness sensed. Therefore, the energy of the g-forces sensed as a function of distance must completely represent the kinetic energy response of the quarter-car from profile roughness. Applying the energy transformation to

Equation (26) and applying a linearization produces the average g-force magnitude per unit of distance $R_{\bar{v}}^{L}$ as

$$R_{\bar{v}}^{L} = \sqrt{\frac{1}{L}\int_{0}^{L/\bar{v}} \left| g_z(t) v(t) \right|^2 dt}. \tag{28}$$

This research defines $R_{\bar{v}}^{L}$ as the RIF-index. Incidentally, for an average speed $v(t) = \bar{v}$ across a path segment of length L, the RIF-transform simplifies to

$$R_{\bar{v}}^{L} = \bar{v}\sqrt{\frac{1}{L}\int_{0}^{L/\bar{v}} \left| g_z(t) \right|^2 dt} = \bar{v}\sqrt{E_{gz}^{L}} \tag{29}$$

where E_{gz}^{L} is the longitudinal energy density of the vertical acceleration signal. The signal energy is in units of Joules per meter when the sensor output is in units of volts. It is evident that the RIF-index is zero when the traversal speed is zero.

3.6.3. Spatial data fusion

The index of roughness $\overline{R}_{\bar{\bar{v}}}^{L}$ is the ensemble average of the RIF-indices from N_v traversals across a path of length L where

$$\overline{R}_{\bar{\bar{v}}}^{L} = \frac{1}{N_v}\sum_{\rho=1}^{N_v} R_{\bar{v}}^{L}[\rho] \tag{30}$$

$R_{\bar{v}}^{L}[\rho]$ is the RIF-index from the ρ^{th} traversal of the segment at an average speed of $\bar{v}$, and $\bar{\bar{v}}$ is the batch mean speed from all traversals. In addition to compressing the inertial and position data longitudinally along the traversal direction, the ensemble averaged RIF (EAR) indices fuses multiple data streams within the same geospatial window of all traversals. Hence, the EAR-index represents a vertical compression when visualizing the RIF-indices from multiple traversals across a segment as a stack of values.

The EAR-index represents the average roughness that the typical vehicle occupant experiences when traveling the segment within a specified range of speeds or speed band. For example, selecting data streams from vehicle traversals that are within 5 km/h of an average speed of 80 km/h will produce an EAR-index that summarizes roughness in proportion to the IRI. However, producing the EAR-indices for the prevailing average speed of a facility type such as the speed limit would be more practical and meaningful. Like the IRI, the RIF-index must be speed-dependent because it is a function of the quarter-car suspension response. Therefore, the EAR-index from the same speed band will correspond to the changes in ride quality within that speed range over time. The TWIT, defined in the next section, integrates the EAR-indices from all speed bands to produce a speed-independent characterization of roughness.

3.6.4. The Time-Wavelength-Intensity Transform

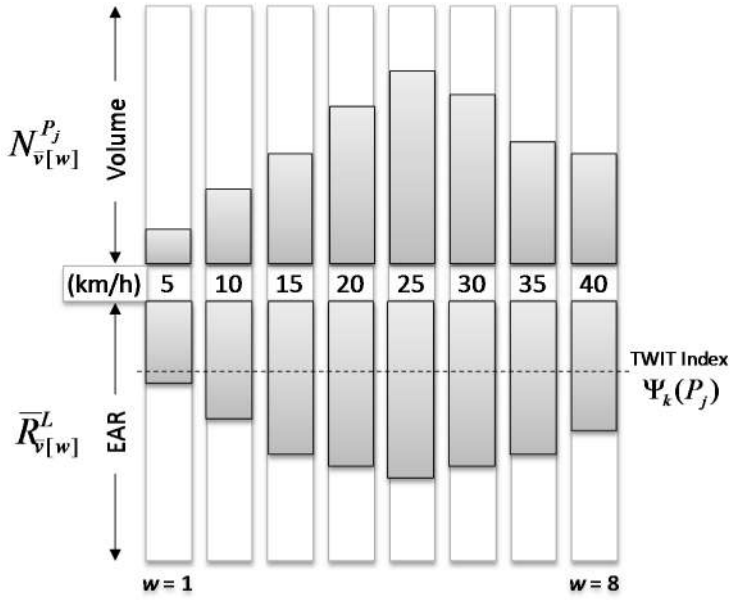

Figure 11. Graphical representation of the TWIT components

The TWIT is a linear combination of the EAR-indices from available speed bands. The coefficients are the percentages of traversals within each speed band. The TWIT, denoted by the

dependent variable Ψ is, therefore, a weighted EAR-index by traffic volume within each speed band or window *w* such that:

$$\Psi_k(P_j) = \frac{\sum_{w=1}^{N_k} \overline{R}^L_{\bar{v}[w]} \times N^{P_j}_{\bar{v}[w]}}{\sum_{w=1}^{N_k} N^{P_j}_{\bar{v}[w]}} \tag{31}$$

The units of time increment ΔP_j should match the period that agencies use to measure traffic volume, which is typically one hour. The number of segment *k* traversals in period increment ΔP_j within speed band $\bar{v}[w]$ is denoted $N^{P_j}_{\bar{v}[w]}$. The corresponding EAR-index for each speed band is denoted $\overline{R}^L_{\bar{v}[w]}$. The total number of speed bands available for segment *k* is N_k.

Figure 11 is a graphical representation of the EAR-indices and the TWIT index for a hypothetical road segment after a period of one day. For this scenario, the width of each speed band is 5 km/h. The selection of bin width depends on the application. This selection will involve a tradeoff in traversal volume available for the speed band and the speed variance. Chapter 6 explores how the tradeoff in traversal volume and speed variance affects the precision of empirical models that forecast pavement deterioration.

From Bernoulli's Theorem (Papoulis 1991), as the vehicle volume across a segment increases, the EAR-index within a speed window will converge to represent the average ride quality that the occupant of a typical vehicle experienced. For each speed window, the vehicle suspension will respond most to spatial wavelengths near $\bar{v}/f_s$ that coincide with the range of sprung-mass modes. Therefore, as the number of traversals and speed bands increases, the TWIT will produce an unbiased representation of the true spatial wavelength composition of the segment. Furthermore, the weighted linear combination of the EAR-indices from each speed

band will adapt the TWIT to emphasize wavelengths that most significantly affect ride quality within the predominant speed ranges.

The TWIT is analogous to the short-time Fourier transform in signal processing. For roadways, the vehicle speed amounts to a spatial frequency selector that characterizes the ride quality from a narrow range of wavelengths along the path. Hence, slow speeds will emphasize the responses from the short spatial wavelengths of narrow cracks and small bumps. Conversely, higher speeds will emphasize quarter-car responses to longer spatial wavelengths that could be symptoms of emerging subgrade problems. Overall, the TWIT-index is a broadband summary of the roughness that a typical rider experienced for the range of speeds traveled. Consequently, the TWIT-index has the desirable property that it will represent changes in actual ride quality over time even if the spectral characteristics of the segment changes. On the other hand, the EAR-index from different speed bands would represent wavelength selective changes in ride quality over time that could be symptoms of specific road distress. In particular, the EAR-index derived from an 80 km/h speed band will be representative of the IRI.

3.7. Case Study of Applying the Models

This case study uses a regular passenger vehicle to collect the GPS and inertial data that the RIF-transform requires. The selected road contains distinctly smooth and rough segments, including a very rough rail grade crossing. A chi-squared fit of the RIF-index distribution with classic statistical distributions will typify the quality of the data collected.

3.7.1. Data collection site and equipment

Numerous apps are currently available for nearly all of the popular smartphone models to log data from their internal sensors such as the GPS receiver, the tri-axial accelerometer, and the tri-axial gyroscope. One smartphone app developed at the university provided the ability to

select the sample rate of the inertial sensor (Bouret 2013). The iOS® device logged time, inertial, and geospatial position data from 30 traversals of a 2007 Subaru Legacy sedan through the segment of Bolley Drive. The vehicle remained within 1 $m \cdot s^{-1}$ of the average speed of 7 $m \cdot s^{-1}$.

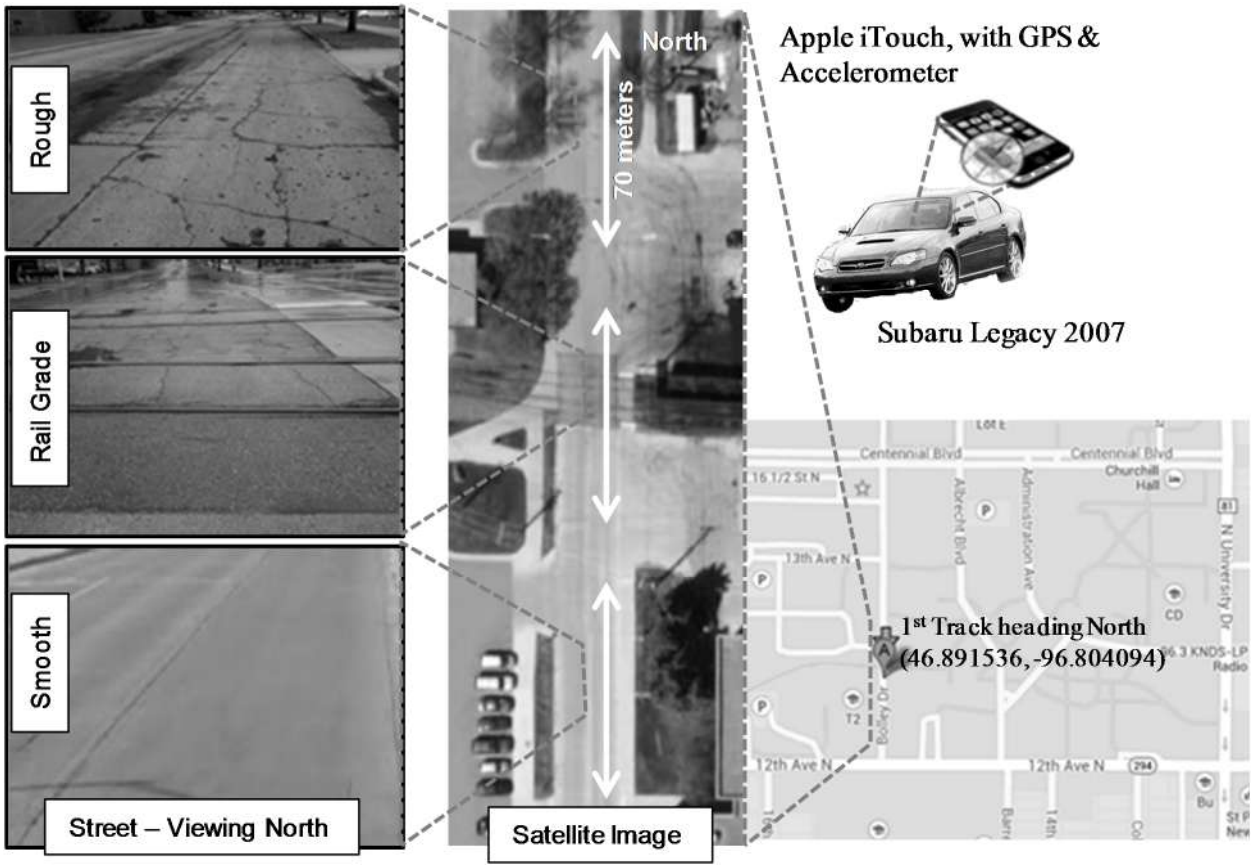

Figure 12. Data collection site and equipment for the RIF-indices

Figure 12 illustrates the setting. The road segment contains a rail grade crossing that produces a noticeably rougher ride than the rest of the segment. The crossing consists of four rails. The latitude and longitude of the first track crossed when heading north is as indicated in Figure 12. The 70-meter segment south of the crossing looks and feels significantly smoother than the 70-meter segment north of the crossing. Similarly, the north segment looks and feels much smoother than the 70-meter segment containing the crossing. The maximum achievable

GPS and accelerometer update rates for this case study were 1 and 93 hertz, respectively. Chapter 5 develops criteria and methodology for selecting the best update rates for each sensor.

3.7.2. Data format

The accelerometer produced "Gz," "Gx," and "Gy," which are the g-forces sensed in the vertical, lateral, and longitudinal directions, respectively, with each normalized to 9.81 $m \cdot s^{-2}$. The gyroscope produced the "Pitch," "Roll," and "Yaw," which are the sensor orientation angles in degrees, respectively. The gyroscope also produced the "Rx," "Ry," and "Rz" values, which are the angular rotational rates about the respective sensor axis in degrees per second.

Table 3. Data format used for the RIF-transform

Time	Gz	Lat	Lon	Vel	Pitch	Roll	Yaw	Gx	Gy
21.347	-0.98	46.88096	-96.7701	1.42	8.19	1.51	-25.61	0.05	-0.13
23.956	-1.02	46.88096	-96.7701	1.42	8.17	1.51	-25.63	0.05	-0.14
26.118	-0.99	46.88096	-96.7701	1.42	8.17	1.51	-25.63	0.02	-0.15
37.812	-1.03	46.88096	-96.7701	1.42	8.17	1.50	-25.64	0.05	-0.12
48.627	-0.97	46.88096	-96.7701	1.42	8.17	1.50	-25.64	0.08	-0.14
59.410	-1.02	46.88096	-96.7701	1.42	8.16	1.55	-25.67	0.00	-0.16
123.741	-0.95	46.88096	-96.7701	1.42	8.20	1.47	-25.73	0.02	-0.13
134.777	-1.05	46.88096	-96.7701	1.42	8.20	1.47	-25.73	0.04	-0.15

Table 3 shows a fragment of the dataset that the smartphone app produced as a comma separated value (CSV) file format. The first row contains a header with labels for each column of data sampled from the sensors. The "Time" column is the sample period in milliseconds. The output register of the GPS receiver produced the "Lat" and "Lon," which are the latitude and longitude, respectively, in decimal format. These values were unchanged for this data fragment because the inertial sensor updated 93 times faster than the GPS receiver did. The GPS receiver also produced the "Vel," which is the estimated ground speed in $m \cdot s^{-1}$.

3.7.3. Data volume and upload time

The data from each vehicle will contain ten parameters per row as shown in Table 3. The data logger uses single-precision floating-point (32 bits) to store each parameter in digital memory. Each row contains the sample interval time instant and the updated sample from each sensor output. Hence, the data logger will have a capacity of 217, 109, and 54 hours per gigabyte (GB) of memory storage for sample rates of 32, 64, and 128 hertz, respectively. Each sensor produces an updated output asynchronously with respect to the other. Therefore, a higher sample rate will capture fresher data whenever the sensor changes its output. However, blindly sampling at the highest rates possible could produce more data than are necessary. Chapter 5 analyzes the trade-off between sample rate and performance requirements to select the best settings.

The data logger will opportunistically identify available and approved networks to upload its recently captured data. For example, vehicles may upload data when parked in a Wi-Fi zone such as near a home or office. This approach continually frees memory to store new data. Sampling at 32, 64, and 128 hertz produces data at the rates of 10.2, 20.5, and 41 kilobits per second (kbps).

Table 4. Data rates and time capacity as a function of sample rate

Rates	Collection Rate (hertz)		
	32	**64**	**128**
Data Rate (kbps)	10.2	20.5	41.0
Capacity (hrs/GB)	217	109	54
Upload time per drive hour (sec)	1.8	3.7	7.4

Table 4 summarizes the data rates, time capacity, and upload time per drive hour. Incidentally, the 20.5 kbps capture data rate from sampling at 64 hertz is similar to the compact

disc audio bandwidth of 22.1 kilohertz. A wireless connection at 20 megabits per second (mbps) will require 6.7 minutes per GB of data upload. That is, the wireless upload of 109 hours of data sampled at 64 hertz will take less than 7 minutes. Viewed alternatively, using the same wireless connection speed will require 3.7 seconds to upload the data logged at 64 hertz for every hour of drive time. Hence, a connected vehicle environment that uses standard DSRC will provide the opportunity for near real-time analysis of roadway conditions.

Table 5. Data capacity requirements for different speeds and sample rate

Capacity (km/GB)	Collection Rate (hertz)		
	32	64	128
25 km/h (~15 mph)	5,425	2,713	1,356
55 km/h (~34 mph)	11,936	5,968	2,984
100 km/h (~62 mph)	21,701	10,851	5,425

Table 5 summarizes the storage capacity between uploads in terms of kilometers of profiling for each traversal velocity and sample rate combination. Roughness characterizations of local roads with typically low speed limits will take longer than highways where the traversal speed could be four times greater. Hence, between uploads, the data logger will have a greater distance capacity per unit of available memory for restricted access roads such as freeways.

3.7.4. Path distance tagging

The GPS update rate must be sufficiently high to account for differences in the traversal distance along curvilinear paths. Studies found that vehicles travel no faster than 20 mph when traversing the sharpest right-turn curves that have a minimum corner radius of 25 feet (Fitzpatrick and IV 2005). This is equivalent to traversing the curved path of about 12 meters in length at a speed of approximately 9 $m \cdot s^{-1}$. Hence, in this worst-case scenario, the GPS must update faster than 0.75 Hz to provide an estimate for the traversal distance along the curviest

paths expected. Present technology limits the maximum update rate of standard GPS receivers to about 10 Hz (O'Kane and Ringwood 2012). Most devices such as smartphones allow a maximum GPS update rate of 1 Hz. Consequently, the GPS update rate would be several-fold slower than the maximum accelerometer sample rate. To accommodate this misalignment in update rates, the data processing algorithm must interpolate between GPS updates to estimate the path distance between accelerometer samples. The interpolated distance is the ratio of the GPS update distance to the number of intervening accelerometer samples. GPS receivers typically incorporate Kalman filters to minimize the effects of multipath reflections and any loss of satellite line-of-sight conditions (Brookner 1998). The approximate distance between a pair of GPS coordinates on the earth's surface where (Θ_S, Φ_S) and (Θ_E, Φ_E) denotes the start and end (latitude, longitude) pairs, respectively, is (Gade 2010)

$$\Delta L = R_{earth}\left[2 \times \arcsin\left(\sqrt{\sin\left(\frac{\Theta_S - \Theta_E}{2}\right)^2 + \cos(\Theta_S) \times \cos(\Theta_E) \times \sin\left(\frac{\Phi_S - \Phi_E}{2}\right)^2}\right)\right] \tag{32}$$

where R_{earth} is the mean earth radius of approximately 6,371 kilometers. The appendix outlines the algorithm used to compute the path distances for traversals of the case studies.

3.7.5. Data distribution models

The case studies will use the critical chi-squared value to test the distribution of RIF-indices for candidacy as a Gaussian, a Student-*t*, a lognormal, or a logistic distribution. A least squares method will estimate parameters of each distribution that best fit the measured histograms of RIF-indices. The four distributions selected for testing exhibit similar characteristics as a function of sample size (Agresti and Finlay 2008). The Gaussian distribution $D_g(\imath)$, as a function of the frequency bin $\imath$ is

$$D_g(\iota) = \frac{\alpha_g}{\sqrt{2\pi\sigma_g^2}} \exp\left[-\frac{1}{2}\left(\frac{\iota - \mu_g}{\sigma_g} \right)^2 \right] \tag{33}$$

where α_g, μ_g, and σ_g are estimates of the amplitude, mean, and standard deviation parameters, respectively. Similarly, the modified Student's *t*-distribution $D_t(\iota)$ to test is

$$D_t(\iota) = \frac{\alpha_t}{\sigma_t} t_{df}\left[\frac{\iota - \mu_t}{\sigma_t} \right] \tag{34}$$

where $t_{df}(\iota)$ is the normalized Student's *t*-distribution, which is a gamma function of ι and *df* degrees-of-freedom. The parameters α_t, μ_t, and σ_t are estimates of the amplitude, mean, and standard deviation parameters, respectively. The lognormal distribution $D_n(\iota)$ to test is

$$D_n(\iota) = \frac{\alpha_n}{\iota\sqrt{2\pi\sigma_n^2}} \exp\left[-\frac{1}{2}\left(\frac{\ln(\iota) - \mu_n}{\sigma_n} \right)^2 \right]. \tag{35}$$

The parameters α_n, μ_n, and σ_n are estimates of the amplitude, mean, and standard deviation parameters, respectively.

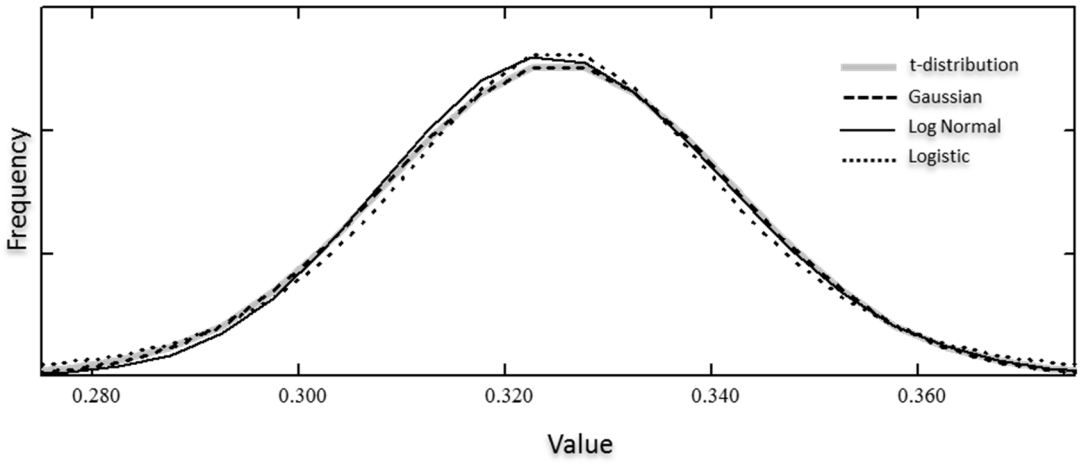

Figure 13. Similarities of the selected classical distributions

The logistic distribution is denoted $D_L(\iota)$, and the associated parameters α_L, μ_L, and σ_L are estimates of the amplitude, mean, and standard deviation, respectively, where

$$D_L(\iota) = \frac{\alpha_L}{\sigma_L\left[1+\exp\left(-\frac{\iota-\mu_L}{\sigma_L}\right)\right]^2}\exp\left[-\frac{\iota-\mu_L}{\sigma_L}\right]. \tag{36}$$

Each distribution provides a slightly different fit for the data histogram. Figure 13 illustrates their similarities for the same mean and spread of a normalized random variable.

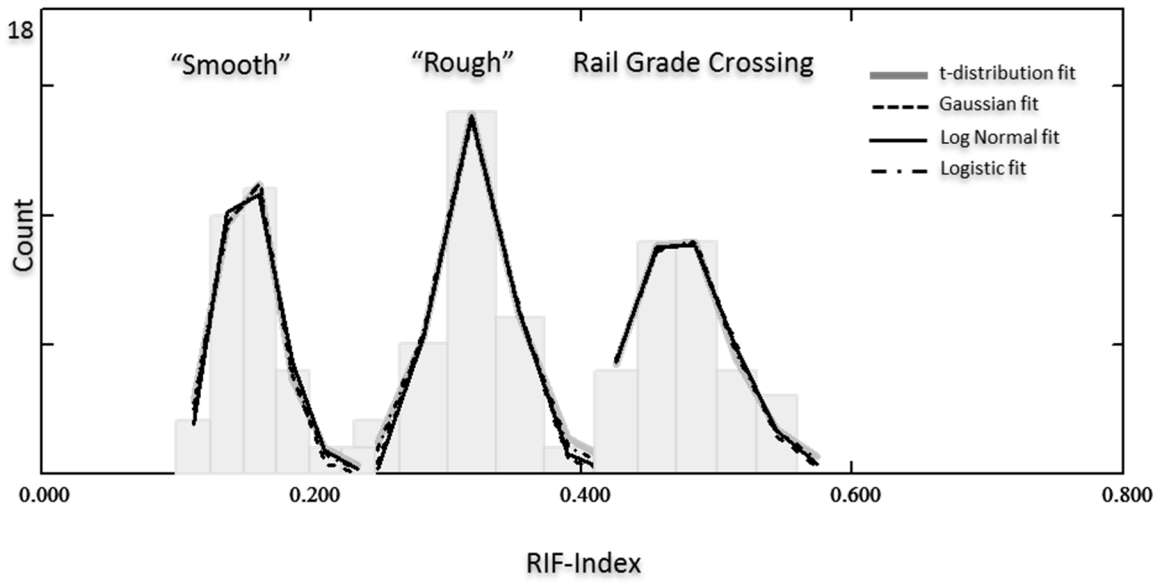

Figure 14. RIF-index distributions for Bolley Drive traversals

The Student's *t*-distribution is practically identical to a Gaussian as sample sizes approach 30. The logistic distribution has heavier tails than the Gaussian distribution and may provide a better model for the distribution of relatively few samples from a case study. The lognormal distribution typically provides a better fit for skewed distributions.

3.7.6. Experimental results

Figure 14 plots the histograms of RIF-indices derived from the data collected for relatively "smooth" and "rough" sections of Bolley Drive, and the section that includes the very rough rail grade crossing.

Table 6. Parameter estimates for the RIF-index distribution fit

	Smooth	Rough	Rail Grade
Gaussian			
df	3	3	3
χ^2 (α = 5%)	7.815	7.815	7.815
χ^2 Data	79.22	151.597	2.111
Significance α (%)	0	0	**54.976**
Amplitude	0.681	0.929	0.886
Mean	0.152	0.32	0.471
Standard Dev.	0.022	0.027	0.037
Student-t			
df	3	3	3
χ^2 (α = 5%)	7.815	7.815	7.815
χ^2 Data	1.673	1.636	1.707
Significance α (%)	**64.293**	**65.136**	**63.547**
Amplitude	0.738	1.022	0.968
Mean	0.151	0.32	0.47
Standard Dev.	0.021	0.027	0.036
Lognormal			
df	3	3	3
χ^2 (α = 5%)	7.815	7.815	7.815
χ^2 Data	6.151	47.872	1.669
Significance α (%)	**10.45**	0	**64.384**
Amplitude	0.687	0.927	0.88
LN(mean)	-1.878	-1.139	-0.751
Standard Dev.	0.148	0.084	0.078
Logistic			
df	3	3	3
χ^2 (α = 5%)	7.815	7.815	7.815
χ^2 Data	5.978	6.746	1.793
Significance α (%)	**11.268**	**8.044**	**61.655**
Amplitude	0.705	0.972	0.92
Mean	0.152	0.32	0.47
Standard Dev.	0.014	0.017	0.023
EAR-Index	0.155	0.322	0.475
$MOE_{0.95}$ (%)	6.928	4.465	2.778
$\sigma_v / \overline{v}$ **(%)**	6.395	6.695	6.105

The plots show that each of the four distributions fit the histograms in a similar manner. It is evident that the EAR-index for each segment is distinctly different as anticipated. Each shape mimics those of classical parametric distributions. Table 6 summarizes the parameter estimates for each of the four distributions from the three road segments. The critical chi-squared value listed in the table as "χ^2 Data" is an evaluation of the expression

$$\chi^2 = \sum_{k=1}^{n} \frac{(O_k - E_k)^2}{E_k} \tag{37}$$

where O_k are histogram values observed in bin k and E_k are the expected values from the hypothesized distribution. The chi-squared distribution value at 5% significance ($\alpha = 5\%$) is the largest value expected with a probability of, at most, 5%. The chi-squared degrees-of-freedom *df* listed are one unit less than the number of histogram bins n, minus the two independent distribution parameters estimated, which are the amplitude and the standard-deviation, the latter being dependent on the estimate of the mean. That is, negligibly small deviations from the tested distribution will yield a relatively small critical χ^2 value where the significance level would be expectedly much greater than 5%. Statisticians generally reject a null hypothesis that the data follow a tested distribution if the significance of the critical χ^2 value is less than 5%, or equivalently, if the critical χ^2 value is larger than the chi-square distribution value at 5% significance.

For at least two of the tested distributions in all three cases, the critical chi-squared values are substantially smaller than the distribution chi-squared values at 5% significance. Therefore, the tests cannot reject a hypothesis that the distribution of the RIF-indices follows one of the distributions. This agreement with classic distributions provides a high degree of confidence that

with higher levels of vehicle traversals, the margin of error (MOE) will diminish to approach the true segment roughness.

The MOE for the RIF-index $\Delta R^L_{1-\alpha}$ within a (1-α)% confidence interval of significance α (Papoulis 1991) is

$$\Delta R^L_{1-\alpha} = \pm \frac{\sigma^L_R \times t_{1-\alpha/2,df}}{\sqrt{N^{P_j}_{\bar{v}[w]}}} \tag{38}$$

where $N^{P_j}_{\bar{v}[w]}$ is the traversal volume defined in Equation (31) and $t_{1-\alpha/2,df}$ is the *t*-score where the normalized cumulative *t*-distribution of *df* degrees of freedom equals (1-α). The standard deviation of the RIF-index is denoted σ^L_R. The ratio of $MOE_{1-\alpha}$ to the EAR-index is the MOE percentage, which is a relative measure of the data spread. For example, $MOE_{0.95}$ (%) indicates that 95% of the data points are likely to be within that percentage of the EAR-index. Table 6 lists the $MOE_{0.95}$ (%) for each of the three road segments. The average MOE for all segments is less than 5% with only 29 traversals each. This provides a high confidence that the MOE % will become progressively smaller with additional traversals. The velocity standard deviation σ_v as a percentage of the mean velocity $\bar{v}$ is less than 7%. Velocity variance contributes to RIF-index variance. Chapter 5 further examines its significance with respect to selecting the appropriate GPS update rate.

3.8. Summary

This chapter developed a new roughness simulation model to provide the theoretical foundation for evaluating the new roughness characterization models under a range of conditions. The key concepts of vertical acceleration potential and kinetic energies provided the insights needed to develop the new roughness characterization models. This suite of models

establishes the analytical framework for the remaining research. A derivation of the quarter-car model reveals the mechanical filtering action that explains the IRI deficiencies reported. The spatial wavelength bias of the IRI is a fundamental limitation that results from the fixed speed constraint of the IRI-transform. The RIF-transform relies on the integration of data from multiple heterogeneous sensors that include a tri-axial accelerometer, a tri-axial gyroscope, a ground velocity sensor, a timer, and a geospatial position receiver. The resulting data stream from individual vehicle traversals is a stream of the resultant vertical acceleration sensed and a path distance associated with each sample. The RIF-transform produces a single-index summary of roughness per unit of longitudinal distance, traversed within a specified speed range. The EAR-index is the average RIF-index from all vehicle traversals of a specified segment, within the specified speed window. The TWIT integrates the EAR-indices from all available speed bands for the segment to provide a wavelength unbiased characterization of roughness.

The case study demonstrated practical utilization of the EAR-index by using a smartphone app to log the required sensor data from a regular passenger car. Each row of the data stream contained the sample updates from a smartphone with integrated timer, accelerometer, gyroscope, and GPS receiver. Based on the data rates utilized, the typical smartphone would be capable of storing more than 100 hours of data per gigabyte of available storage.

The local road selected consists of three equal length segments with distinct differences in roughness, including a rail grade crossing. Fewer than 30 vehicle traversals near the speed limit provided a suitable statistical sampling of RIF-indices for each segment. The differences in EAR-indices for each segment matched the perceived differences in relative roughness. The average margin-of-error for the EAR-indices was approximately 4% for a 95% confidence

interval. The chi-squared tests could not reject the hypothesis that the distribution of RIF-indices are in accordance with classical models such as the Gaussian, Student-*t*, lognormal, and logistic distributions. Therefore, the case study validated the models and provided a high degree of confidence that the EAR-index, and consequently the TWIT, will continue to provide a higher precision of ride quality characterization as additional vehicles traverse the segment. Hence, the high volume of traversals anticipated from connected vehicle environments will provide an ideal setting to use these new models.

CHAPTER 4. CHARACTERISTICS OF THE MODELS

This chapter compares the IRI and RIF-transforms under various scenarios of profile roughness. The analytical bump model developed in Chapter 3 provides an ability to methodically simulate, analyze, and compare the behaviors of each transform by varying the bump width, bump height, and vehicle speed. The literature search summarizes and explores the limitations of existing approaches to transform inertial data into a single-index summary of roughness. A proof of the direct proportionality relationship between the IRI and the RIF-index utilizes their underlying commonality as linear time-invariant systems. A functional decomposition of their inner operations explains the similarities and differences in their responses to a range of roughness characteristics. The case study validates the proportionality relationship. A scenario study demonstrates how practitioners could extend IRI datasets by using EAR-indices and the RIF/IRI proportionality relationship.

4.1. Literature Search of Inertial and Position Data Integration Models

The literature search reveals a lack of models to transform accelerometer and GPS data into a single-index summary of roughness. The available approaches generally apply a time or frequency domain transform to the inertial data. Time domain methods include the ARI given by Equation (1) and the RMS of the accelerometer signal (Papagiannakis 1997). The latter is similar to the ARI, and neither accounts for variations in vehicle speed. Frequency domain methods such as the Fourier Transform (Douangphachanh and Oneyama 2013) and the PSD (Chen, Lu, et al. 2011) are computationally intensive and they do not identify localized roughness. Hybrid methods such as the Wavelet Transform (Tomiyama, Kawamura and Ohiro 2014) and the Hilbert-Huang Transform (Ayenu-Prah and Attoh-Okine 2009) attempt to localize roughness by decomposing the time-domain signal into empirical basis functions. By

approximating the shape of typical inertial signatures, basis functions match similar features in the signal but they do not provide a single-index summary of roughness. Almost all methods reported are some variation of the procedure to produce the IRI, and they require a fixed speed standard (Múčka 2015). Methods of compensation for speed variations often result in an unstable index that could approach an infinite value when speed decreases toward zero (Dawkins, et al. 2011).

4.2. Behavior of the IRI and the RIF-transforms

Chapter 3 demonstrated how variations in the bump width or the traversal speed shift the frequency distribution of vertical acceleration energy produced. This section examines the relative effects of such variations on the output of the IRI- and RIF-transforms.

4.2.1. Speed relationship

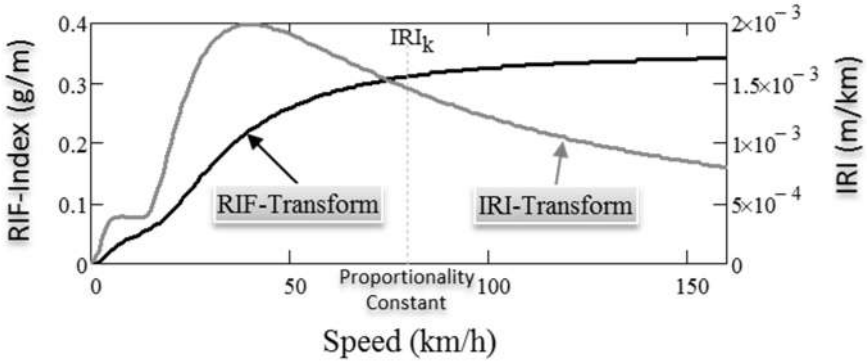

Figure 15. IRI and RIF-transforms for a 10-centimeter high by 1-meter wide bump

Figure 15 plots the output of the IRI- and RIF-transforms from traversing a 10-centimeter high by 1-meter wide bump at a range of speeds. The RIF-index is in units of g-force/meter on the left vertical axis, whereas the IRI is in units of m/km on the right vertical axis. The IRI for the simulated bump is as indicated at the marker crossing of its reference speed at 80 km/h. Output peaks of the IRI-transform are located at speeds that translate potential energy of bumps to the sprung- and unsprung-mass resonant modes of the Golden Car. Bump energy peaks that

coincide with the unsprung-mass resonance produce the largest excitation to the series mass-spring system. The RIF-index also approaches a maximum because it integrates energy from the quarter-car sprung-mass response. Overall, the RIF-transform is less sensitive to speed variations. This is a desirable feature because it accommodates a greater speed-band width when computing the TWIT-index.

4.2.2. Bump height relationship

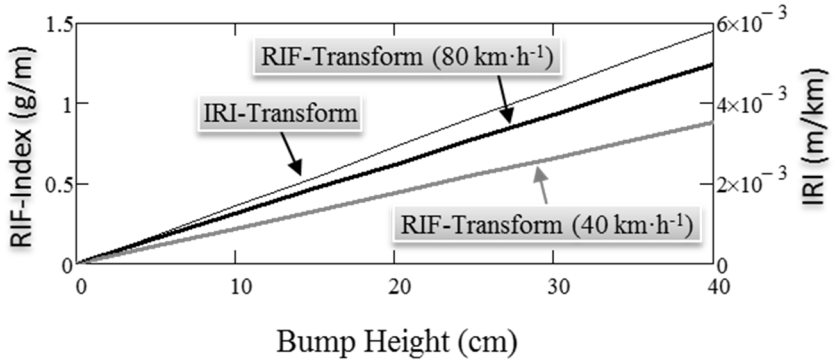

Figure 16. RIF-indices and IRI at two speeds for a 10-meter wide bump of varying heights

Both the RIF-index and the IRI are directly proportional to bump height. Figure 16 compares the RIF-index and the IRI for a 10-meter wide bump of varying heights. The plot shows the RIF-index at the IRI reference speed as well as half that speed. This result indicates that the RIF-index and IRI are directly proportional for a given bump width and traversal speed. The next section explores how the RIF/IRI proportionality constant varies with bump width at the IRI reference speed.

4.2.3. Bump width relationship

As demonstrated in Chapter 3, for a given speed the frequency of the peak potential energy of a bump increases as its width decreases and vice-versa. Bump widths of approximately 2 meters produce peak potential energy that coincides with the unsprung-mass resonant mode of the quarter-car. Therefore, the peak roughness indices occur when the peak

potential energy of bumps coincide with the quarter-car resonant modes. This phenomenon at a fixed traversal speed is responsible for the wavelength bias of the IRI.

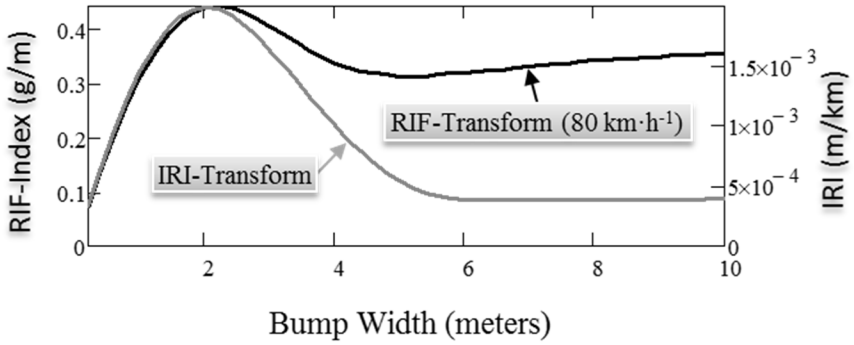

Figure 17. RIF/IRI for a 10-centimeter high bump of varying widths

Figure 17 plots the RIF-index and the IRI for a range of bump widths traversed at the 80 km/h reference speed. As the bump width increases beyond 5 meters, its peak potential energy moves away from the unsprung-mass mode and toward the sprung-mass mode. Therefore, the output of both transforms settle because the wider bumps produce less excitation at the unsprung-mass mode. This result demonstrates that for a fixed speed, the RIF/IRI proportionality varies with the bump width composition of the elevation profile. At a fixed speed, the RIF- and IRI-transforms integrate roughness energy from all bump widths of the profile. Figure 16 demonstrates that both transforms are directly proportional to the overall roughness intensity of the profile. Therefore, the ratio of RIF/IRI for any road segment must be a constant. However, this constant will vary among profiles that exhibit different distributions of bump widths. Therefore, applications that would extend the IRI datasets by switching to the RIF-index must characterize the constant before applying it. Real roads contain a broad range of bump sizes. Therefore, the shapes of their potential energy spectra are likely to remain relatively broadband over time, and that characteristic will lessen the need for periodic recalibration of the ratio.

4.3. Derivation of the RIF-IRI Proportionality Constant

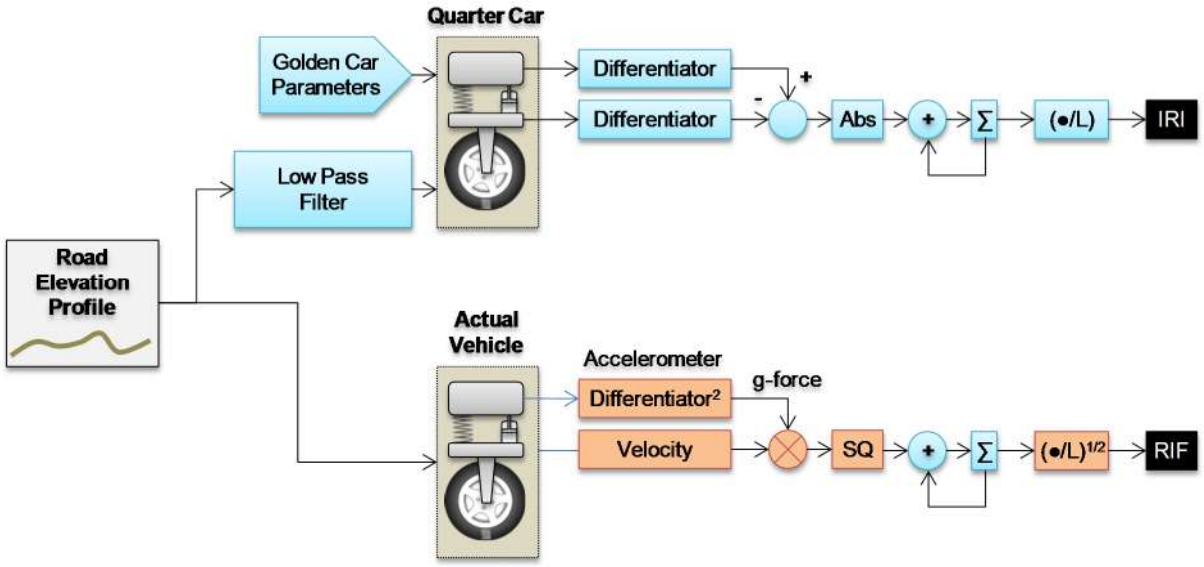

Figure 18. Functional decomposition of the RIF- and IRI-transforms

The RIF-index and the IRI are linear-time-invariant (LTI) transforms because they integrate the responses from a linear mass-spring system (C.-T. Chen 2004). The RIF- and IRI-transforms are a cascade of LTI transforms of the elevation profile along the wheel path as illustrated by the functional decomposition in Figure 18. The upper cascade illustrates the process steps that software packages use to produce the IRI. The procedure begins by applying a moving average filter to the samples of the elevation profile. This filter removes unwanted high frequency content such as electronic noise and spurious vibrations. The procedure then applies the filtered signal as a forcing function to the damped mass-spring model of the Golden Car. A numerical method then computes the sprung- and unsprung-mass motion rates by differentiation. The IRI is the accumulated absolute rate difference between the sprung- and unsprung-mass per unit length of the segment analyzed. The lower cascade represents how practitioners would produce the RIF-index in practice. An accelerometer mounted to the body of an actual vehicle samples the g-forces produced from body-bounces as it travels along a path of the elevation

profile. An algorithm then computes the square of the product of each g-force sample and the instantaneous velocity obtained from the speed sensor. The RIF-index is the square root of the accumulated result, normalized to the segment length. This functional decomposition demonstrates the similarities and differences of each transform. The underlying commonality of their LTI transforms explains their direct proportionality relationship. A proof of this relationship will utilize the theoretical impulse to provide a broadband excitation for each transform that would yield an expression that depends only on the fixed quarter-car parameters and other constants.

4.3.1. The IRI-transform of the Golden Car impulse response

Removing the low pass filter in the IRI cascade equalizes the inputs to both transforms. From Equation (15), the sprung-mass impulse response is

$$z_{\delta s}(t) = u(t)\frac{1}{\omega_s\sqrt{1-\zeta_s^2}}\exp\left(-\zeta_s\omega_s t\right)\sin\left(\omega_s t\sqrt{1-\zeta_s^2}\right) \tag{39}$$

and the unsprung-mass impulse response is

$$z_{\delta u}(t) = u(t)\frac{1}{\omega_u\sqrt{1-\zeta_u^2}}\exp\left(-\zeta_u\omega_u t\right)\sin\left(\omega_u t\sqrt{1-\zeta_u^2}\right) \tag{40}$$

The convolution of Equation (22) provides the quarter-car impulse response $q_z(t)$. Therefore, substituting the impulse response expressions from Equations (39) and (40) into Equation (22) yields the quarter-car impulse response. Table 2 in Chapter 3 provided the Golden Car sprung- and unsprung-mass parameters used to evaluate the expressions. Computing the sprung- and unsprung-mass vertical motion rates $\dot{z}_s(t)$ and $\dot{z}_u(t)$, respectively, and applying them to Equation (19) produces the IRI-transform $I_{\bar{v}}^{L}(t)$.

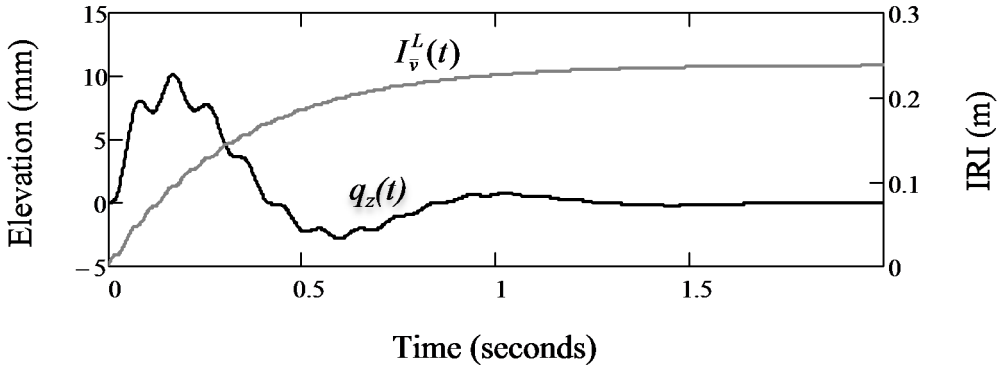

Figure 19. Impulse response of the Golden Car model and the IRI instants

Figure 19 plots the transform output as a function of time to observe its accumulation with the quarter-car impulse response.

The absolute value of the instantaneous rate difference in Equation (19) hinders a closed form expression for the integration. Evaluating the output instead using a numerical method of integration, the transform converges to a constant of 0.240 meters in the limit $t \to \infty$. A series expansion of the integration coupled with some heuristics yields the expression

$$\lim_{t\to\infty} I_{\bar{v}}^{L}(t) \cong \frac{1}{2}\left(\frac{1}{\omega_s \zeta_s} + \frac{1}{\omega_u \zeta_u}\right)^2 \frac{1}{\sqrt{\left(1-\zeta_s^2\right)\left(1-\zeta_u^2\right)}} \tag{41}$$

that approximates the converged numerical value within a fraction of a millimeter.

4.3.2. The RIF-transform of the Golden Car impulse response

Utilizing the distributive property of LTI systems, the convolution of the sprung- and unsprung-mass impulse responses is equivalent to a linear combination of their individual impulse responses where

$$q_z(t) = z_{\delta s}(t) * z_{\delta u}(t) = z_{\delta s}(t) + \rho_\delta z_{\delta u}(t). \tag{42}$$

For impulse excitations, the coefficient of linear combination ρ_δ is unity because an impulse identically excites all subsystem modes. However, their motions are in opposite phase because of the series mass-spring arrangement, hence ρ_δ = -1 for impulse excitation (Angeles 2011).

The vertical acceleration produced from the quarter-car impulse response is

$$a_{z\delta}(t) = \frac{d^2}{dt^2}\left[q_z(t)\right] = \ddot{z}_{\delta s}(t) + \rho_\delta \ddot{z}_{\delta u}(t) \tag{43}$$

From Equation (23), the g-force sensed for a quarter-car where W_z = 1 is

$$g_{z\delta}(t) = \frac{\gamma_g}{g} a_{z\delta}(t) = \frac{\gamma_g}{g}\left[\ddot{z}_{\delta s}(t) + \rho_\delta \ddot{z}_{\delta u}(t)\right] \tag{44}$$

Closed form solutions for the accumulated second derivative of the impulse responses of Equations (39) and (40) are

$$\int_0^{T_\varepsilon} \left|\ddot{z}_{\delta s}(t)\right|^2 dt = \omega_s\left(\zeta_s + \frac{1}{4\zeta_s}\right) \tag{45}$$

and

$$\int_0^{T_\varepsilon} \left|\ddot{z}_{\delta u}(t)\right|^2 dt = \omega_u\left(\zeta_u + \frac{1}{4\zeta_u}\right) \tag{46}$$

respectively, where $L/\bar{v}=T_\varepsilon$ such that $\left|g_{z\delta}(T_\varepsilon)\right|$ becomes negligibly small. The quarter-car impulse response becomes negligibly small for T_ε > 2.0 seconds as observed in Figure 19. Substituting Equations (44), (45), and (46) into Equation (29) yields the RIF-index for the quarter-car impulse response as

$$R_{\bar{v}}^L = \bar{v}\frac{\gamma_g}{g}\sqrt{\frac{1}{L}}\sqrt{\omega_s\left(\zeta_s + \frac{1}{4\zeta_s}\right) + \rho_\delta^2\omega_u\left(\zeta_u + \frac{1}{4\zeta_u}\right)}. \tag{47}$$

Therefore, the RIF/IRI proportionality constant κ_{RI} is

$$\kappa_{RI} = \frac{\bar{v}\frac{\gamma_g}{g}\sqrt{\frac{1}{L}}\sqrt{\omega_s\left(\zeta_s + \frac{1}{4\zeta_s}\right) + \rho_\delta^2\omega_u\left(\zeta_u + \frac{1}{4\zeta_u}\right)}}{\frac{1}{2}\left(\frac{1}{\omega_s\zeta_s} + \frac{1}{\omega_u\zeta_u}\right)^2 \frac{1}{\sqrt{\left(1-\zeta_s^2\right)\left(1-\zeta_u^2\right)}}}. \quad (48)$$

The κ_{RI} proportionality constant is for an impulse excitation, which is equivalent to a broadband elevation profile spectrum. This expression evaluates to a constant of 5.8 for the Golden Car parameters, the reference speed of 80 km/h, a sensor constant of $\gamma_g = 1$, and a segment distance of one kilometer per the standard unit of IRI measure. The theoretical impulse excitation is the largest possible; therefore, this ratio represents the theoretical bound. The RIF-index for the transient responses to the impulse excitation was 1.4 g-force/meter, whereas the IRI accumulated to 0.240 meters after 1 kilometer of theoretical travel at the IRI reference speed. The actual RIF/IRI constant of proportionality will be much smaller for practical road excitations.

4.4. Case Studies and Practical Applications

RIF and IRI data simultaneously collected with a laser-based Inertial Profiler provide validation of the consistency of their direct proportionality for an actual segment of road, using a real vehicle.

4.4.1. Equipment and test facilities

The North Dakota Department of Transportation (NDDOT) calibrates its Inertial Profiler annually at the MnROAD facility near Monticello Minnesota. The calibration procedure required only six to 10 traversals of Cell 37, which is a 500-feet (~153 meter) segment of the low-volume road. An industrial grade data logger (Appareo NaviCube™) aboard the NDDOT vehicle logged the inertial and GPS data while the Inertial Profiler instrumentation sampled the

elevation profile. The Appareo data logger sampled the vertical acceleration at approximately 125 hertz and updated the GPS coordinates at approximately 2 hertz. These update rates were about twice that of the iOS device used in Chapter 3 to validate the RIF-transform models.

The NDDOT Inertial Profiler is a modified model E350 Ford van. It is equipped with left wheel path (LWP) and right wheel path (RWP) laser-based height sensors and a GPS receiver. The height sensors measure the profile elevation at approximately 3.8-centimeter intervals when the vehicle moves at a fixed speed. The onboard equipment produced elevation profile samples using the standard **.erd* file format. The Profile Viewing and Analysis (ProVAL) software from The Transtec Group then converted LWP and RWP data to the IRI values.

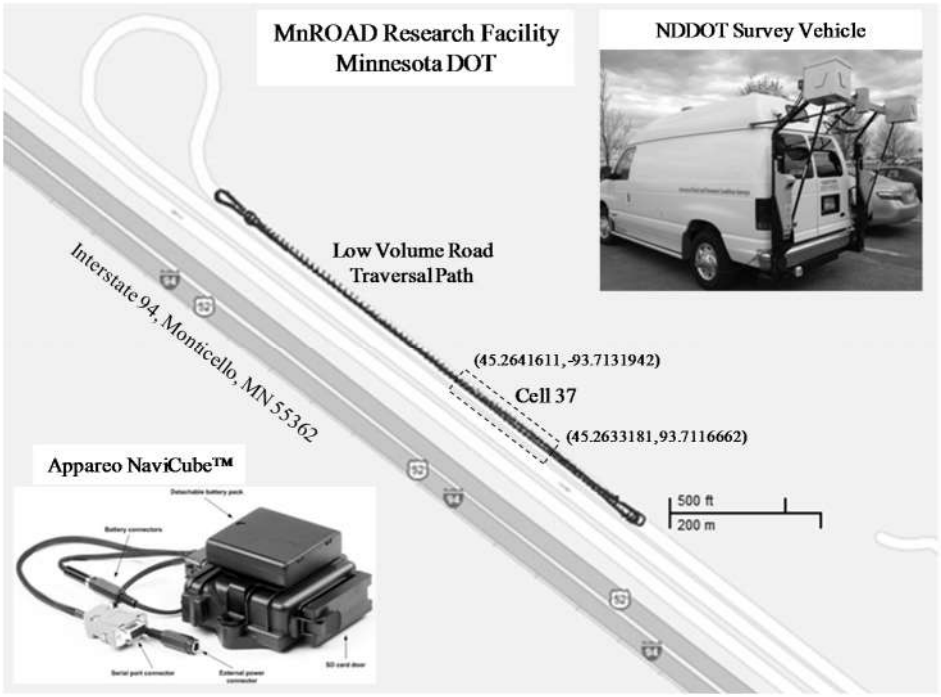

Figure 20. Traversal path for the instrumented vehicle

Figure 20 shows the location of the MnROAD facility and Cell 37. The data logger is in the bottom left inset and the Inertial Profiler is in the top right inset of the figure.

4.4.2. Results of direct RIF/IRI proportionality

The ProVAL software produced IRI separately for the elevation profile samples from the LWP and RWP. Agencies typically report the IRI as the average of the values transformed from the LWP and RWP elevation profiles. The Inertial Profiler has the ability to regulate the traversal speed. This capability minimizes speed variations to provide a consistent sample interval for the laser-based distance measurement system. The traversal speed was about 35 miles-per-hour. The onboard velocity sensor reported the speed in units of $m \cdot s^{-1}$ but converting this to km/h provides the more familiar units. The IRI reported was in units of m/km. The RIF-index was in units of g-force/meter.

Table 7. IRI and RIF-index data collected from the MnROAD experiments

Traversal	Speed	IRI	RIF	RIF/IRI
1	55.46	1.59	0.105	0.066
2	55.56	1.59	0.114	0.072
3	55.54	1.59	0.107	0.067
4	55.61	1.54	0.108	0.070
5	55.69	1.56	0.104	0.067
6	55.79	1.57	0.108	0.069
Average	55.61	1.57	0.108	0.068
$MOE_{0.95}$ (%)	0.22	1.38	3.41	3.35

Table 7 summarizes the data collected. The $MOE_{0.95}$ is the 95% confidence interval as a percentage of the average values. Even with only six data points, the $MOE_{0.95}$ of the IRI was within less than 2% of the mean.

The EAR-index for the 150-meter segment was 0.108 g-force/meter. The EAR/IRI ratio was approximately 68×10^{-3}. Although higher than the IRI variability, the $MOE_{0.95}$ of the RIF-index was within less than 4% of the mean. Hence, the RIF/IRI ratio was similarly consistent. Three significant factors accounting for the lower IRI variability are 1) the low pass filtering of

the sampled elevation profile 2) the fixed parameters of the Golden Car model, and 3) the fixed reference speed. Firstly, as shown previously in Figure 18, the procedure to produce the IRI begins by removing higher frequency variations in the elevation profile using a moving average filter. Conversely, the RIF-transform does not filter the inertial sensor data prior to producing the RIF-index. Secondly, the IRI transform simulates the motions of the sprung- and unsprung-mass of a fixed quarter-car, namely the Golden Car. Conversely, the RIF-transform responds to the sprung-mass motion of the actual vehicle. Thirdly, the ProVAL software translates the spatially sampled elevation profile data to the fixed IRI reference speed, with practically zero variance, before applying it to the Golden Car model. Conversely, the RIF-transform incorporates the instantaneous speed variations that the onboard sensor reports.

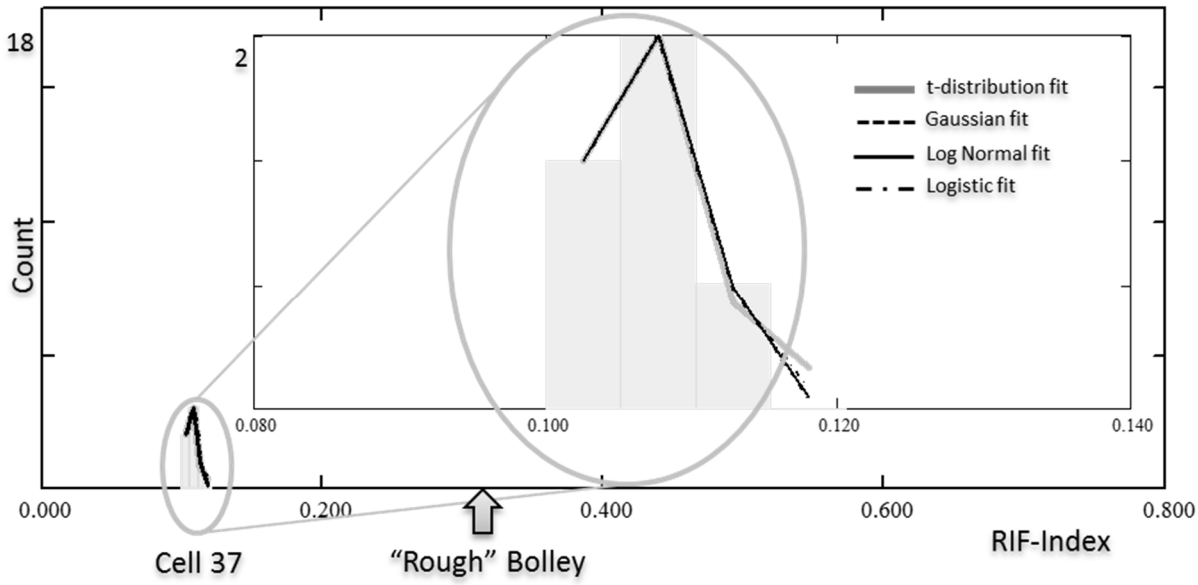

Figure 21. RIF-index distributions for MnROAD

Figure 21 plots the RIF-index histogram and distribution fit for traversals of the MnROAD Cell 37. The chart uses the same scale as those of Figure 14 in Chapter 3 for relative comparison. The inset enlarges the distribution plot for Cell 37 for visual clarity.

Table 8. Distribution parameters for the Bolley Dr. and MnROAD RIF-index histograms

	Rough Bolley	**MnROAD**
Gaussian		
df	3	1
χ^2 (α = 5%)	7.815	3.841
χ^2 Data	151.597	0.071
Significance α (%)	0	**79.049**
Amplitude	0.929	0.033
Mean	0.32	0.106
Standard Dev.	0.027	0.004
Student-t		
df	3	1
χ^2 (α = 5%)	7.815	3.841
χ^2 Data	1.636	0.356
Significance α (%)	**65.136**	**55.07**
Amplitude	1.022	0.043
Mean	0.32	0.106
Standard Dev.	0.027	0.004
Lognormal		
df	3	1
χ^2 (α = 5%)	7.815	3.841
χ^2 Data	47.872	0.085
Significance α (%)	0	**77.081**
Amplitude	0.927	0.032
LN(mean)	-1.139	-2.239
Standard Dev.	0.084	0.038
Logistic		
df	3	1
χ^2 (α = 5%)	7.815	3.841
χ^2 Data	6.746	0.161
Significance α (%)	**8.044**	**68.835**
Amplitude	0.972	0.034
Mean	0.32	0.106
Standard Dev.	0.017	0.003
EAR-Index	0.322	0.108
$MOE_{0.95}$ (%)	4.465	3.590
$\sigma_v / \overline{v}$ **(%)**	6.695	0.025

As observed, the "rough" Bolley Drive segment exhibits nearly three times the roughness density of the MnROAD cell. This relationship agrees with the subjective perception. Even with significantly fewer traversals, it is evident that the spread of the RIF-indices for the MnROAD traversals is smaller than that for the Bolley Drive traversals. The much smaller variance of the Inertial Profiler velocity and the smoother segment is a significant contributor to the reduction in variance of the EAR-index for the MnROAD traversals.

Another factor that reduced the variance of the EAR-index for the MnROAD segment over the Bolley Drive segment is the path length. The MnROAD segment is 80 meters longer than the Bolley Drive segment. Hence, the spreading of localized errors in GPS path distance evaluations across a longer segment reduced the overall path length variability.

Table 8 summarizes the parameters for each distribution fit using a least squares method. For the MnROAD distribution, the critical chi-squared values were much smaller than the distribution chi-squared values at 5% significance. In fact, the test statistics were sufficiently small such that the equivalent significance percentage is much larger than 5% as indicated. Even with relatively few traversals, the chi-squared test cannot reject the hypothesis that the data follows any of the tested distributions. The smaller variance in traversal speed for the MnROAD dataset accounted for the improved MOE over the Bolley Drive data, even for significantly fewer traversals and a lower EAR-index. This result provides a high degree of confidence in the measured EAR/IRI proportionality constant.

4.4.3. Extending IRI applications with EAR datasets

The direct proportionality relationship allows the EAR-index to extend applications that rely on historical IRI data. Present and future EAR indices computed from one or more speed bands, or their combination thereof via the TWIT transform, can provide an alternative to

collecting elevation profile samples and producing the IRI. For instance, a deterioration forecasting application may have estimated the coefficient β_L from IRI data collected during the period $0 \le P_j < 5$ years using the empirical model

$$I_{\bar{v}}^{L}(P_j) = I_{\bar{v}}^{L}(P_0)e^{\beta_L P_j}. \tag{49}$$

Future data on ride quality will continue to improve the estimate of β_L. Hence, agencies can continue to collect ride quality data in the form of RIF-indices and convert them to IRI.

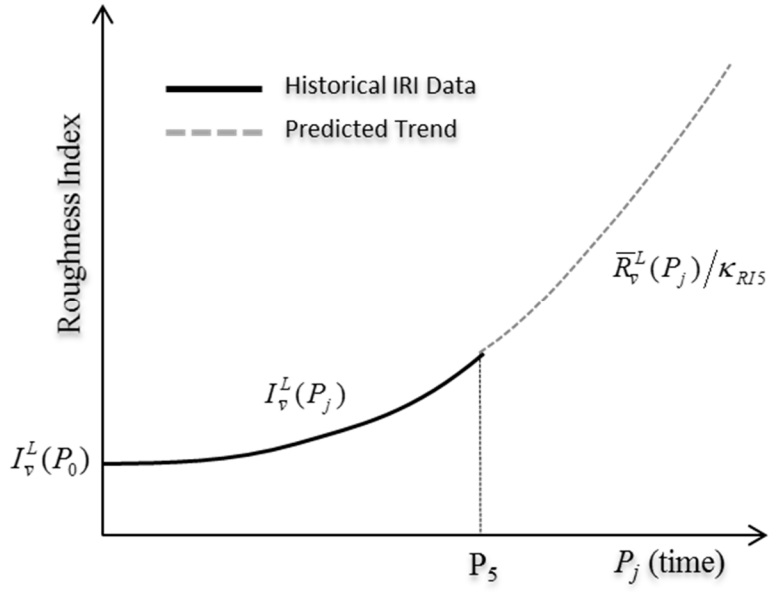

Figure 22. IRI application scenario extended with EAR indices

The solid line of Figure 22 illustrates a hypothetical IRI trend for periods prior to P_5. The dashed line represents a forecasted trend for periods after P_5. The forecasted trend uses the EAR indices $\bar{R}_{\bar{v}}^{L}(P_j)$ scaled by the EAR/IRI proportionality constant κ_{RI5} measured in year P_5. Therefore, the modified forecasting model is

$$\bar{R}_{\bar{v}}^{L}(P_j) = \kappa_{RI5} I_{\bar{v}}^{L}(P_0)e^{\beta_L P_j}. \tag{50}$$

That is, EAR indices collected in the future years $P_j > 5$ for a speed band around the speed limit of the segment will provide the coefficients $\beta_L[j]$ where

$$\beta_L[j] = \frac{1}{P_j} \ln\left[\frac{\overline{R}_{\bar{v}}^{L}(P_j)}{\kappa_{RI5} I_{\bar{v}}^{L}(P_0)} \right] \tag{51}$$

and the updated calibration coefficient β_L to forecast future EAR indices would be

$$\beta_L = \frac{1}{J_N} \sum_{j=1}^{J_N} \beta_L[j] \tag{52}$$

where J_N is the total number of time periods available in the overall dataset.

4.4.4. Estimating the IRI from EAR measurements

Practitioners who prefer not to transition to the EAR-index but cannot afford IRI characterizations using specialized Inertial Profiler vehicles could use regular vehicles to estimate IRI values from the EAR-index measurements. In such situations, the practitioner may use a quantitative or a qualitative approach. The former approach requires recent IRI characterizations of the facility to determine the proportionality factor, whereas the latter does not. The tradeoff is precision. The quantitative approach will provide an IRI value that is within a few percentage points of the actual IRI value. On the other hand, the qualitative approach will provide an IRI value that is within a larger window that would map to the typical qualitative descriptions of pavement conditions within that range.

The precision of the quantitative approach depends on the recentness of IRI values determined for the facility. As the bump width analysis indicated, any significant differences in the spectral profile characteristics from previous characterizations could require an update of the proportionality factor. FHWA analysis of long-term pavement performance (LTPP) data indicates that the PSD, or equivalently, the wavelength distribution remains relatively unchanged over time (Karamihas and Senn 2012). Therefore, changes in the proportionality factor would likely be insignificant for a majority of pavements. The qualitative approach is appropriate for

local and unpaved roads with no prior IRI assessments, and for which a gross estimate of the IRI would suffice. The next section provides a case study.

4.4.5. Case study of qualitative IRI estimates

The difficulty of maintaining a relatively constant speed, and the presence of anomalies that would distort the reference plane for laser-based height measurements, prevent agencies from using Inertial Profilers to assess the IRI for local roads such as Bolley Drive (NCHRP 2013).

Table 9. IRI estimates based on RIF-index measurements

	Bolley Drive (70-meter) Segments			**MnROAD**
	Smooth	Rough	Rail Grade	150-meter Cell
EAR-index (g-force/meter)	0.155	0.322	0.475	0.108
IRI estimate (m/km)	2.265	4.705	6.941	1.578
IRI estimate (in/mile)	143.511	298.133	439.792	99.995
Characteristic condition (IRI range in m/km)	New Pavements (1.5 – 3.5)	Worn Pavements (2.5 – 6.0)	Damaged Pavements (4.0 – 11.0)	Airport Runways (< 2.0)

Table 9 summarizes the IRI estimates for the three Bolley Drive segments based on their measured EAR-indices and the proportionality constant obtained from the MnROAD traversals. The table includes the World Bank descriptions of pavement conditions that would map to the range of IRI values shown (Gillespie, Sayers and Queiroz 1986). As expected, all the estimates correlated with the *relative* differences in roughness observed. The estimated IRI values corresponded to the characteristic conditions observed for each pavement section as pictured in Figure 12. This result indicates that the qualitative approach provides a viable alternative to roughness characterizations for facilities such as local and unpaved roads where IRI characterizations are not affordable or not feasible. Chapter 5 will examine the sensitivity of the EAR-index as a function of sensor and vehicle parameter variances.

4.5. Summary

This chapter examined the relative behavioral characteristics of the new transforms developed in Chapter 3 and the prevailing IRI transform that nearly all agencies currently use to report official ride quality data. Simulations of the models demonstrated their similarities and differences in roughness characterizations as a function of traversal speed, bump height, and bump width. The IRI is limited to characterizing roughness at a fixed speed by simulating the response of a fixed quarter-car. Conversely, the RIF-index characterizes roughness by reporting the average g-force actually experienced per unit distance and at any speed. The analysis demonstrated that relative to the IRI, the RIF-transform exhibits a lower sensitivity to speed variations. This characteristic accommodates wider speed bands without appreciably increasing the variance of the RIF-index.

With all other factors unchanged, the analysis found that both transforms are directly proportional to changes in bump height at any speed. Hence, the transforms are directly proportional to each other. The direct proportionality relationship dictates that the RIF-index and the IRI will change by the same proportions for a given change in the overall roughness intensity of the elevation profile. For example, with all other factors being equal, doubling the bump height will double both the RIF-index and the IRI. This direct proportionality relationship is significant because of the potential practical benefits. For instance, the EAR-index for a given speed band, such as the speed limit of the facility, can extend applications that rely on historical IRI data by applying a single proportionality constant to either dataset.

Frequency domain analysis provided further insights about the conditions that would require updating the proportionality factor. Changes in the bump width composition of the elevation profile will change the proportionality constant. However, IRI updates to recalibrate

the proportionality constant may be unnecessary for most applications because research demonstrated that the spatial frequency distribution of the elevation profile remains similar as the pavement ages.

An impulse excitation provided the broadband excitation for the quarter-car to characterize its response and to derive an expression for the theoretical bound of the RIF/IRI proportionality constant. The RIF- and IRI-transforms of the quarter-car impulse response converged to expressions that depended only on the fixed quarter-car parameters, the IRI reference speed, and the segment length. Subsequently, their constant ratio proved the RIF/IRI direct proportionality relationship for a given quarter-car and a specified speed band.

This chapter provided two case studies. The first demonstrated the repeatability of the RIF/IRI proportionality and the second demonstrated utility of the factor to estimate the IRI for any facility without sampling its elevation profile. The first case study used an inertial profile vehicle to collect IRI and RIF-index related data simultaneously from the MnROAD Cell 37. The proportionality factor derived from each traversal was consistent within a 4% margin-of-error of the 95% confidence interval. This result promoted high confidence in measuring the constant of proportionality with relatively few traversals of an Inertial Profiler. The second case study demonstrated the benefit of converting EAR-indices to IRI estimates by using the proportionality factor obtained from characterizing a different facility. The value ranges associated with the gross IRI estimates matched the qualitative condition description for those segments. This result indicated that the qualitative approach to IRI estimation by measuring EAR-indices provides a viable alternative for facilities such as local and unpaved roads where IRI characterizations are not affordable or not feasible.

CHAPTER 5. SELECTING THE BEST SENSOR SETTINGS

This chapter examines the effects of sensor installation, orientation, sample frequency, and update rate settings to establish recommended standards. The literature search reveals that studies utilizing accelerometers and GPS receivers to characterize road roughness tend to ignore analysis of the impact that their settings has on the quality of the data or the results. Sampling the output of sensors too frequently could result in an unnecessary increase in power consumption, memory requirements, and data upload time. Conversely, sampling too slowly will under represent the system and introduce large errors. This chapter determines the impact of sensor installation and parameter selection and then recommends the best settings.

5.1. Literature Review of Sensor Parameter Selection and Impact

The practical application of inertial and GPS sensors involves decisions about their installation characteristics and parameter settings. The earliest reported experiments used analog accelerometers constructed from multiple discrete components and circuits that were bulky. The sensing mechanism was a brick-sized device that researchers strapped directly to the driver's chest. This approach was an attempt to isolate vibrations from other parts of the vehicle that could cause the analog integrator to overflow (Rizenbergs 1965). Nearly all experiments conducted more recently use highly integrated data loggers such as smartphones with embedded digital accelerometers and GPS receivers that conveniently mount to a vehicle's dashboard (Astarita, et al. 2012), (Douangphachanh and Oneyama 2013). Such data loggers include noise filters to band-limit the signals for the selected sample rate (Android Open Source Project 2014). The pre-installed position and orientation of connected vehicle sensors would likely remain consistent because of normal manufacturing practices to specify standard modules and installation procedures for high-throughput assembly line operations. However, the parameters

for after-market probe devices, including smart phones, are likely to vary much more because of different manufacturer recommendations and user preferences.

The case studies of this research discovered that fixing the data logger to the dashboard of the vehicle provided the best combination of inertial sensing and GPS receiver data quality. The data processing algorithm accounted for the orientation of the device to produce a resultant vertical acceleration component of the tri-axial inertial signal. This is the first study to characterize the trade-off between inertial sensor sample rate, traversal volume, and variance of the RIF-index (Bridgelall 2014). Related studies simply selected the highest sample rate available from the inertial sensor used at the time (Tai, Chan and Hsu 2010), (Dawkins, et al. 2011), (Mednis, et al. 2011), (Douangphachanh and Oneyama 2013). There are no studies to guide the selection of the GPS update. For fast-moving vehicles, sub-optimum GPS update rate selection can result in position tagging errors of tens of meters or the need for more data memory and wireless bandwidth than is necessary.

5.2. Considerations for the Inertial Sensor Installation

Road roughness excites all the resonant vibration modes of a moving vehicle. The dominant vibration modes are from the individual mass-spring systems of each quarter-car. An actual vehicle will also exhibit vibration modes that potentially originate from other sources such as loose components, cargo, and the engine. However, vibration sources other than the quarter-car resonant modes are less important when characterizing road roughness; the signal processing algorithms can attenuate unwanted vibrations with an appropriate low-pass filter if necessary. However, the RIF- and EAR-transforms will tend to average the noise from random vibrations across many vehicle traversals. Hence, another benefit of the new transforms is that they obviate the need to apply additional signal processing such as low-pass filtering to the inertial data.

5.2.1. Sensor orientation

The resultant vertical acceleration for any sensor orientation is the product of the linear acceleration from each sensor axis and the magnitude of the axis component of the rotated vertical unit vector in Cartesian space. The vector rotation Π_{xyz} in three-dimensional space is

$$\Pi_{xyz}(u_{xyz},\Lambda,\theta,\phi)=\begin{bmatrix}1 & 0 & 0\\ 0 & \cos(\Lambda) & \sin(\Lambda)\\ 0 & -\sin(\Lambda) & \cos(\Lambda)\end{bmatrix}\begin{bmatrix}\cos(\theta) & 0 & -\sin(\theta)\\ 0 & 1 & 0\\ \sin(\theta) & 0 & \cos(\theta)\end{bmatrix}\begin{bmatrix}\cos(\phi) & \sin(\phi) & 0\\ -\sin(\phi) & \cos(\phi) & 0\\ 0 & 0 & 1\end{bmatrix}u_{xyz} \qquad (53)$$

where Λ, θ, and ϕ are the pitch, roll, and yaw angles produced by the integrated gyroscope sensor. The unit vector $u_{xyz} = [1\ 1\ 1]^T$ represents the composite of the lateral, longitudinal, and vertical directions, respectively. The notation T represents the transpose vector operator. Therefore, the resultant vertical acceleration g_z is

$$g_z(\Lambda,\theta,\phi)=\sqrt{\left[g_{xu}\cdot\Pi_{xyz}(u_z,\Lambda,\theta,\phi)_x\right]^2+\left[g_{yu}\cdot\Pi_{xyz}(u_z,\Lambda,\theta,\phi)_y\right]^2+\left[g_{zu}\cdot\Pi_{xyz}(u_z,\Lambda,\theta,\phi)_z\right]^2} \qquad (54)$$

where g_{xu}, g_{yu}, and g_{zu} are the accelerations registered for the individual sensor axis. The subscript x, y, or z represents the relative contributions from that accelerometer component to the resultant vertical acceleration. Incidentally, a similar method produces the resultant accelerations in the lateral and longitudinal directions.

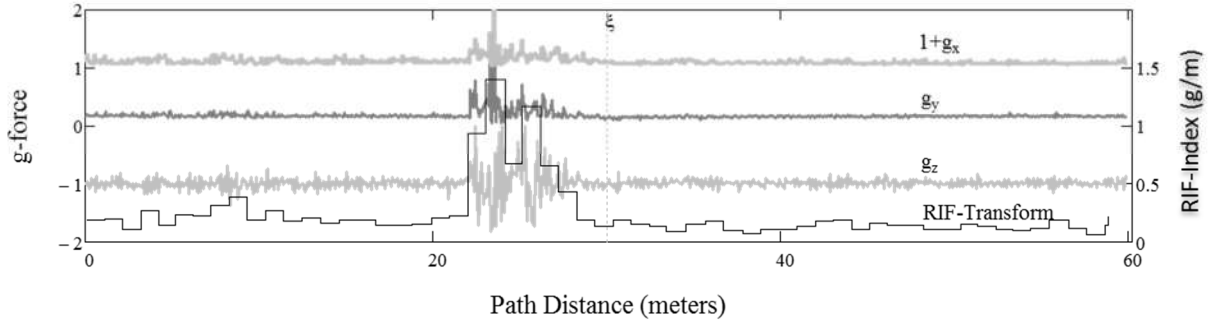

Figure 23. Accelerometer signals and RIF-index profile from a speed bump traversal

Figure 23 plots the RIF-index from a data logger secured to the dashboard of a sport utility vehicle (SUV), traversing a speed bump at 7 $m \cdot s^{-1}$. The labels g_x, g_y, and g_z are in units of g-forces, and they represent the lateral, longitudinal, and vertical accelerations, respectively. The g_z signal offset of approximately -1g is a result of the earth's constant downward gravitational force. The graph artificially offsets the g_x signal by +1g to separate it from the other plots on the same chart. The signal processing algorithm must remove all offset from the individual accelerometer sensors before producing the resultant vertical acceleration for any sensor orientation. This important step assures that the RIF-transform ignores static g-forces and represents only the energy produced from movements.

The first and second peaks of the RIF-indices in Figure 23 are an estimate of the positions of the sensor when the front and rear axles of the vehicle cross the bump, respectively. For this single traversal, the true position of the bump's center is about five meters ahead of the peak RIF-index as indicated by the vertical marker ξ shown at 30 meters. The offset comes from errors in tagging the inertial signal samples with geospatial coordinates. Chapter 7 provides a detailed analysis of this phenomenon and provides a case study.

5.2.2. Sensor placement

Each wheel-assembly contributes a portion of the total inertial energy sensed as described by Equations (23) and (24). The RIF-transform integrates all the roughness energy sensed at its position, regardless of the wheelbase producing it. Consequently, lateral offsets in sensor placement will emphasize roughness from the wheel path that is closest. Sensor installation toward the center of an axle would report the mean roughness sensed from each wheel path. The RIF-index would be insensitive to longitudinal variations in sensor placement when the resolution window L of the RIF-transform is greater than the maximum wheelbase of the vehicle.

A resolution window that is shorter than the wheelbase will emphasize roughness from the axle that is closest to the position of the inertial sensor. Therefore, the recommended sensor placement for ride quality characterizations would be toward the center of the wheel path and at any longitudinal position in the vehicle for resolution windows that exceed the wheelbase.

The recommended sensor installation is a rigid mount to the body frame of the vehicle. Any cushioning between the sensor and the body frame would result in artificial dampening of the vehicle body bounces. The case studies found that a dashboard mounting mechanism works best when using smartphone apps to log the data. Placement of the smartphone in someone's pocket effectively applies an additional set of mechanical filters to the sensor transfer function that could include dampening effects from the seat suspension and the human body. Nevertheless, it is likely that intensity variations from poor installations would become negligible after averaging the data from thousands of vehicle traversals. The data from sensors in connected vehicles will be significantly more consistent because their placement and orientation will be less random across vehicles.

5.3. Selecting the Best Inertial Sensor Sample Rate

To characterize the roughness energy from vehicle vibrations, the Nyquist Theorem (Oppenheim and Schaefer 1975) posits that a sensor must sample the inertial sensor response at a rate that is at least twice that of the highest mode frequency.

Table 10. Estimated quarter-car suspension parameters

	Parameter	Units	Sprung Mass	Unsprung Mass
Car	Resonant frequency (*f*)	hertz	1.739	11.210
	Damping Ratio (ζ)	-	0.282	0.059
Truck	Resonant frequency (*f*)	hertz	1.690	12.160
	Damping Ratio (ζ)	-	0.320	0.050

It is standard practice for vehicle manufacturers to attenuate the suspension motion between 4 and 8 hertz because vibration levels within that frequency range are the most harmful to humans (Griffin 1990). Table 10 lists the quarter-car parameters for a typical car (Kropáč and Múčka 2009) and a typical commercial heavy vehicle (Besinger, Cebon and Cole 1995) to demonstrate their similarities. The guidelines result in a sprung-mass resonant frequency between 0.9 and 1.5 hertz for all vehicle types (General Motors 1987). Consequently, the unsprung-mass resonance frequencies are typically about 10 times higher than the sprung-mass modes (T. D. Gillespie 2004), which is between 9 and 15 hertz.

5.3.1. Estimation of quarter-car response

Fourier transform theory posits that the DFT of an impulse response produces the transfer function of the system that it excites (Oppenheim and Schaefer 1975). The impulse is broadband and, therefore, excites all the vibration modes that the system exhibits. The energy from a sufficiently long sequence of inertial samples will approach the broadband characteristics of an impulse because of the randomness from micro- and macro-textures of a typical road profile.

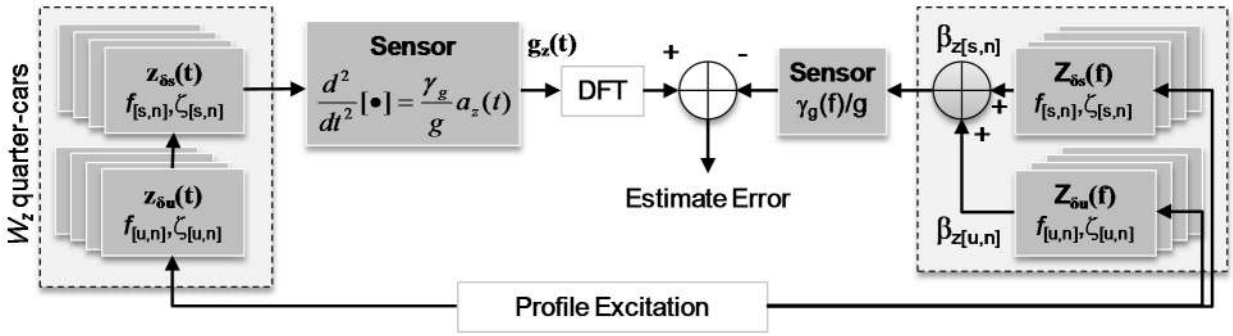

Figure 24. Estimation of the quarter-car response coefficients

The DFT of the accelerometer signal samples will produce a transfer function that reflects the full-car response to profile roughness. Hence, it would be possible to estimate the

suspension parameters by fitting a linear combination of quarter-car models to the DFT of the accelerometer signal samples. Figure 24 shows the framework used to produce a least squares approximation of the quarter-car parameters. The left portion of the diagram represents the DFT of the sensor signal samples $\{\boldsymbol{g}_z\}$. The full-car response is a parallel combination of W_z quarter-car responses. The individual quarter-car responses are a convolution of the sprung- and unsprung-mass system responses as described previously by Equation (42) in Chapter 4. Therefore, from Equation (43) the sensor output for a general profile excitation of all W_z wheel-assemblies is

$$g_z(t) = \frac{\gamma_g}{g} \sum_{n=1}^{W_z} \beta_{z[n]} \left[\ddot{z}_{s[n]}(t) + \rho_{z[n]} \ddot{z}_{u[n]}(t) \right] \tag{55}$$

Non-impulse profile excitations will produce an unsprung- to sprung-mass response magnitude ratio $\rho_{z[n]}$ that is different from unity. Finally, the sensor performs a second derivative of the composite quarter-car responses, applies a constant γ_g, and then produces the digital output in units of g-force.

The right portion of the diagram of Figure 24 is a frequency domain model of the full-car system. It is a linear combination of all the sprung- and unsprung-mass frequency responses. The resultant frequency response is a product of the sensor transfer function and the linear combination of quarter-car responses. The Fourier transform of the vertical acceleration sensed from each mass-spring response produces the frequency domain model such that

$$\Im\left[\ddot{z}_{[m,n]}(t)\right] = \gamma_g(f) Z_{[m,n]}(f) \tag{56}$$

where the subscripts $m = 1$ and $m = 2$ enumerate the sprung-mass (s) and unsprung-mass (u) subsystem parameters, respectively. Hence,

$$\beta_{z[u,n]} = \rho_{z[n]}\beta_{z[s,n]}. \tag{57}$$

The function $\gamma_g(f)$ is the sensor frequency response. It is the second derivative of the motion input signal. The magnitude of Equation (20) with $\omega = 2\pi f$ yields the impulse response magnitude of a quarter-car as

$$\left|Z_{\delta[m,n]}(f)\right| = \frac{1}{4\pi^2}\sqrt{\frac{1}{1-\zeta_{[m,n]}^2}}\frac{1}{\sqrt{\left(\left[f_{[m,n]}^2 - f^2\right]^2 + \left[2\zeta_{[m,n]}f_{[m,n]}f\right]^2\right)}}. \tag{58}$$

Therefore, the magnitudes of the quarter-car impulse responses are dependent only on the damping ratios such that

$$A_{[m,n]} = \frac{1}{4\pi^2\sqrt{\left(1-\zeta_{[m,n]}^2\right)}}. \tag{59}$$

Subsequently, the Fourier transform of Equation (55) is $G_z(f)$ where

$$G_z(f) = \frac{\left|\gamma_g(f)\right|}{g}\sum_{n=1}^{W_z}\sum_{m=1}^{2}\beta_{z[m,n]}A_{[m,n]}\frac{1}{\sqrt{\left(\left[f_{[m,n]}^2 - f^2\right]^2 + \left[2\zeta_{[m,n]}f_{[m,n]}f\right]^2\right)}}. \tag{60}$$

The least squares fit of Equation (60) to the DFT of the sensor output produces estimates for each of the quarter-car resonant frequencies $f_{[m,n]}$, the damping ratios $\zeta_{[m,n]}$, and the coefficients of their linear combination $\beta_{z[m,n]}$. The typical vehicle will exhibit similar quarter-car parameters because of their design symmetry for maximum performance and traction. This scenario simplifies the least squares fit to a single quarter-car and the estimation of values for the β_{zs}, ρ_z, f_s, ζ_s, f_u, and ζ_u parameters.

5.3.2. Sensor signal and noise energy

A vehicle traveling a segment of length L at a constant speed $\overline{v}$ will produce a finite time signal with longitudinal energy density E_{gz}^{L}. Sampling the time-limited signal $g_z(t)$ produces a vector $g_z[k]$ with samples at time instants k. From Parseval's Theorem (Chen 2004):

$$E_{gz}^{L} = \frac{1}{L}\sum_{k=0}^{N-1}\left|g_z[k]\right|^2 = \frac{1}{NL}\sum_{k=0}^{N-1}\left|G_z[k]\right|^2 \tag{61}$$

where $G_z[k]$ is the DFT of $g_z[k]$. At a sample rate of f_s both vectors contain $(L/\bar{v})f_s = N$ samples of the signal $s[k]$ plus noise $e_n[k]$ where $g_z[k] = s[k] + e_n[k]$. The noise or error sequence, e_n includes quantization noise, electronic noise, and randomness from wheel-path variations. The noise energy N_κ is:

$$N_\kappa = E\left\langle e_{[n,\kappa]}^2 \right\rangle \frac{1}{f_s} \tag{62}$$

where $E\left\langle e_{[n,\kappa]}^2 \right\rangle$ is the expected value of the squared sample-errors or, equivalently, the noise power (Skylar 2009) for traversal κ. For a given sample rate f_s the variance of the signal energy among traversals stems from the variance of the noise energy where:

$$Var\left[E_{gz}^{L}\right] = Var\left[N_\kappa\right] = Var\left[\frac{E\left\langle e_{[n,\kappa]}^2 \right\rangle}{f_s}\right] = \frac{1}{f_s^2} Var\left[E\left\langle e_{[n,\kappa]}^2 \right\rangle\right] \tag{63}$$

This expression shows that increasing the sampling rate decreases the variance of the signal, thereby improving the consistency of the sampled signal energy from one traversal to the next.

5.3.3. Variance of the RIF-index

From Equation (29), the RIF-index for a segment of length L, traveled at a mean speed $\overline{v}$ is

$$R_{\bar{v}}^{L} = \bar{v}\sqrt{E_{gz}^{L}} \tag{64}$$

From the theory of error propagation (Ku 1966), the standard deviation of the RIF-index, σ_R^L is:

$$\sigma_R^L = \sqrt{\left(\frac{\partial R_{\bar{v}}^L}{\partial \bar{v}}\right)^2 \sigma_{\bar{v}}^2 + \left(\frac{\partial R_{\bar{v}}^L}{\partial E_{gz}^L}\right)^2 Var\left[E_{gz}^L\right] + \left(\frac{\partial R_{\bar{v}}^L}{\partial \bar{v}}\right)\left(\frac{\partial R_{\bar{v}}^L}{\partial E_{gz}^L}\right)\sigma_{\bar{v}E}^2} \tag{65}$$

where $\sigma_{\bar{v}}^2$ is the batch variance of the mean speed among traversals. The covariance of the mean speed and the vertical acceleration signal energy is denoted $\sigma_{\bar{v}E}^2$. The random variables for mean speed and vertical acceleration signal energy are independent; therefore, the covariance factor is zero. Evaluating the partial derivatives indicated in Equation (65) and substituting the noise energy factor from Equation (63) yields:

$$\sigma_R^L = \sqrt{\bar{E}_{gz}^L \sigma_{\bar{v}}^2 + \left(\bar{\bar{v}}/2\right)^2 \frac{Var\left[E\left\langle e_{[n,\kappa]}^2 \right\rangle\right]}{\bar{E}_{gz}^L} \frac{1}{f_s^2}} \tag{66}$$

where $\bar{E}_{gz}^L$ and $\bar{\bar{v}}$ are the averages of the vertical acceleration signal energy and the batch mean speed among traversals. Hence, the variance of the RIF-index among traversals increases when the variance of the mean traversal speed increases, but decreases when the sample rate increases. Incidentally, the signal-to-noise (SNR) ratio is

$$SNR = \frac{\bar{E}_{gz}^L}{Var\left[E\left\langle e_{[n,\kappa]}^2 \right\rangle\right]} \tag{67}$$

The expression then becomes

$$\sigma_R^L = \sqrt{\bar{E}_{gz}^L \sigma_{\bar{v}}^2 + \left(\bar{\bar{v}}/2\right)^2 \left(\frac{1}{SNR}\right) \frac{1}{f_s^2}} \tag{68}$$

Therefore, the variance of the RIF-index among traversals diminishes with a proportional increase in SNR as expected.

5.4. Case Study for Inertial Sensor Settings

The following sections estimate parameters for the quarter-car equivalent of two different vehicle types. The first estimate is for a luxury sedan, and the second is for the Inertial Profiler van used in the case studies.

5.4.1. Vehicle response estimate

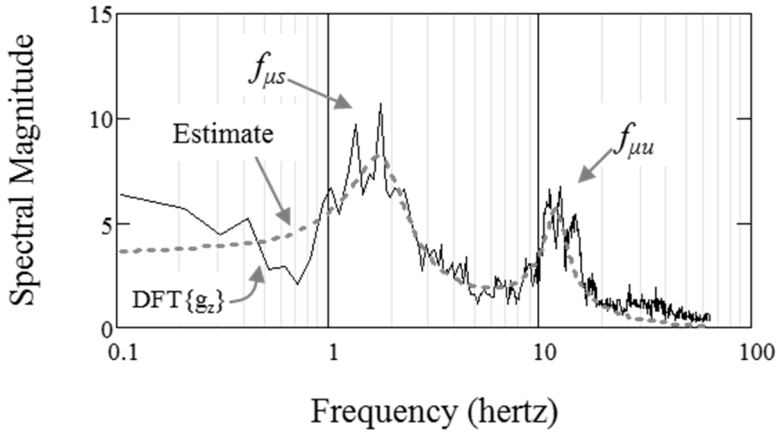

Figure 25. Frequency response estimate of the instrumented passenger car

Figure 25 shows the ensemble average DFT of signal samples $\{\boldsymbol{g}_z\}$ from 30 traversals using a 2007 Toyota Camry LE sedan. The ensemble average improves the SNR of the DFT and increases the accuracy of the estimation. The dotted line is a least squares fit of the quarter-car from Equation (60) with $W_z = 1$. The coefficient of determination for this fit was 91.8%. The estimate indicates that the sprung- and unsprung-mass resonant modes are near 2 and 12 hertz, respectively, and the corresponding damping ratios of approximately 0.3 and 0.1. The estimate for ρ_z was 2.4. The multiple peaks in the DFT response are from harmonics produced when tandem quarter-cars cross the same rough spots to create a semi-periodic waveform. Chapter 7 provides a simulation and a case study of the tandem quarter-car excitation that explains the appearance of harmonics in the response signal.

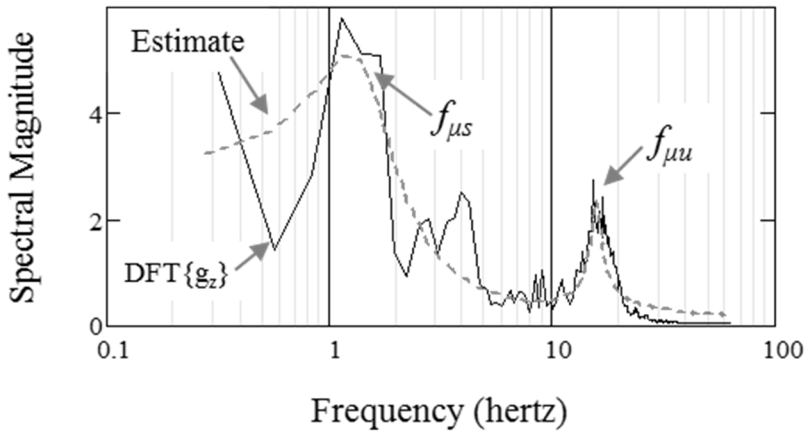

Figure 26. Frequency response estimate of the Inertial Profiler van

The ensemble average DFT reduces noise and hence improves the accuracy of the estimation. However, it is still possible to estimate the equivalent quarter-car parameters from single traversals. For example, Figure 26 shows the estimate from a single traversal of the Inertial Profile vehicle used to collect the IRI data. The estimate improves by including sufficiently long segments to integrate the excited responses of all the quarter-car response modes. It is apparent that the vibrations of equipment in the Inertial Profile van created additional resonant modes near 4 hertz.

Table 11. Parameter estimates for the instrumented vehicles

		Inertial Profiler Van		Passenger Vehicle	
Parameter	**Units**	**Sprung Mass**	**Unsprung Mass**	**Sprung Mass**	**Unsprung Mass**
Resonant frequency (f)	hertz	1.4	15.7	1.7	11.5
Damping ratio (ζ)	-	0.39	0.05	0.27	0.08
Response ratio (ρ_g)	-	4.3		2.4	

Table 11 summarizes the sprung- and unsprung-mass parameter estimates for the vehicles. The estimated parameters are within the ranges expected for typical vehicles and even trucks as indicated in Table 10. The appendix provides additional quarter-car equivalent estimates for the inertial responses of other vehicles used in the various case studies of this work.

5.4.2. Point of diminishing returns

Chapter 3 described the case study that compared roughness for the three Bolley Drive segments by setting the accelerometer sample rate to the highest available frequency of 93 hertz. This case study collected inertial samples $g_z[k]$ at the seven additional sample rates of 1, 2, 4, 8, 16, 32, and 64 hertz with 30 traversals for each.

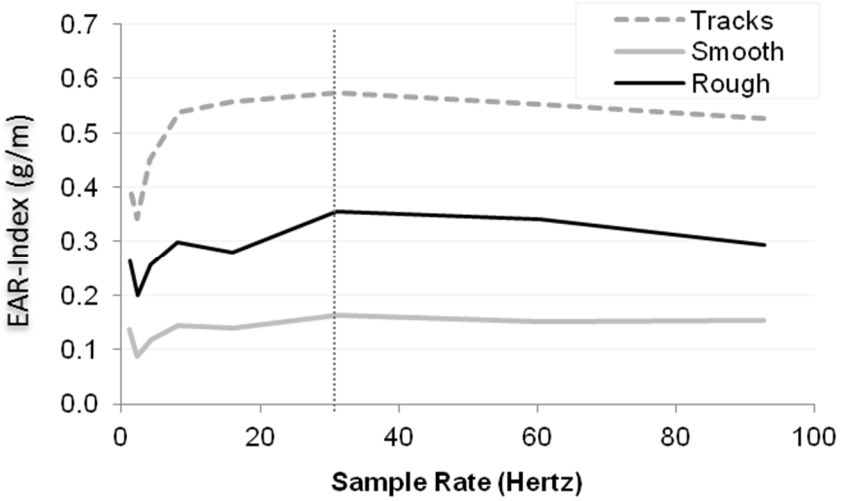

Figure 27. EAR-index convergence with sample rate

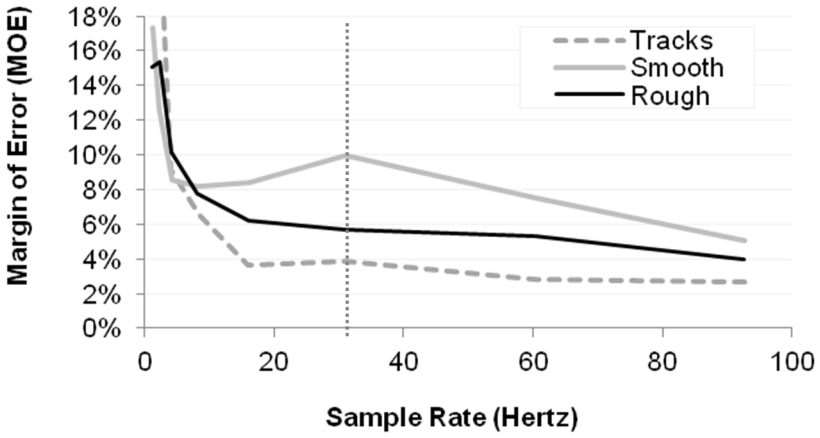

Figure 28. MOE declines with sample rate

Figure 27 plots the EAR-indices from 28 traversals, with two outlier datasets removed. For all sample rates, the relative differences in roughness for each segment corresponded to

roughness differences that the driver perceived. As expected, the roughness measure stabilized as the sample rate increased beyond 32 hertz, which was more than twice the frequency of the estimated unsprung-mass resonance of the vehicle.

Figure 28 plots the MOE_{95} as a percentage of the mean RIF-index. This implies that equal magnitude RIF-index variations will be a larger percentage of lower EAR-indices than for higher ones. For example, the standard deviation of the RIF-index is approximately 0.05 g/meter for each of the road segments sampled at 32 hertz. However, their corresponding MOE_{95} values are 10% for the smooth segment with an EAR-index of 0.16 g/meter, but only 4% for the rail-grade (tracks) segment that produces a much higher EAR-index of 0.57 g/meter.

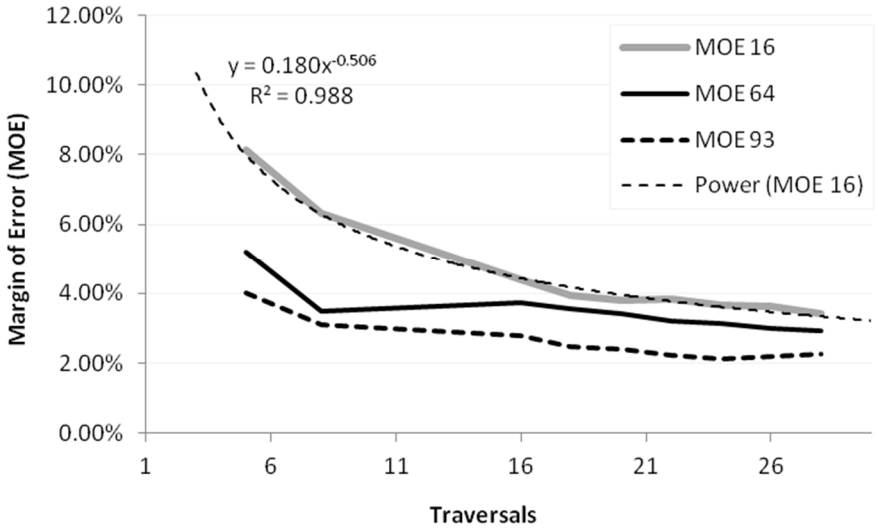

Figure 29. MOE declines with traversal volume

As anticipated from Equation (66), the MOE_{95} for all roughness categories declined as the sample rate increased. Increasing the sample rate beyond twice the dominant mode frequency provided diminishing returns in MOE_{95} reduction. The standard deviation of the RIF-indices measured from all sample rate datasets was within 5% of the theoretical value predicted

by Equation (66). The batch mean of the traversal speeds $\overline{\overline{v}}$ and its standard deviation across 28 traversals was 7.15 $m \cdot s^{-1}$ and 0.45 $m \cdot s^{-1}$, respectively.

5.4.3. Accelerometer sample rate selection

From the central-limit-theorem (Papoulis 1991) and Equation (38), the variance of the RIF-indices diminishes with increasing traversals. Figure 29 plots the MOE_{95} as a function of the traversal volume across a 200-meter section of Bolley Drive that includes all three segments. For sample rates of at least 64 hertz, the MOE_{95} drops below 5% after only six traversals. In general, as the traversal volume increased, the MOE diminished more slowly for higher sample rates than for the lower sample rates. This is because a higher sample rate reduces the noise energy, per Equation (62), thereby improving the signal consistency from one traversal to the next. The trend in error reduction with traversal volume is an inverse power function with exponent -0.51, which is approximately the inverse square root function of Equation (38).

5.5. Selecting the Best GPS Receiver Settings

Depending on the size and complexity of an anomaly, its position at some distance υ_p from a reference point will produce one or more maxima in the accelerometer signal. This analysis introduces a small bump into the wheel path at a known position to simulate a simple anomaly that produces one peak in the vertical acceleration signal. The position tagging system of the sensor integration platform associates each sample of the accelerometer signal with geospatial coordinates obtained from the associated GPS receiver. The position tag $\hat{\upsilon}_p$ of the first signal peak is an estimate of the true position υ_p of the bump's peak. The estimate includes distance biases such that

$$\hat{\upsilon}_p = \upsilon_p + \left(\bar{\varepsilon}_{DSP} + \bar{\varepsilon}_i\right) + \bar{\varepsilon}_b + \left(\bar{\varepsilon}_s + \bar{\varepsilon}_{GPS}\right). \tag{69}$$

This expression groups the biases into three categories: signal processing, vehicle response, and GPS receiver related. The position bias from digital signal processing (DSP) is the expected delay $\bar{\varepsilon}_{DSP}$ from digital filtering.

The accelerometer sample rate is generally several times greater than the GPS sample rate. Hence, the data processing algorithm interpolates the path distance between GPS position updates. This approach fills in path distance gaps that result when the GPS receiver loses line-of-sight conditions, for example, when traveling through a tunnel. Consequently, there is an error $\bar{\varepsilon}_i$ in locating a peak within the interpolation sub-interval.

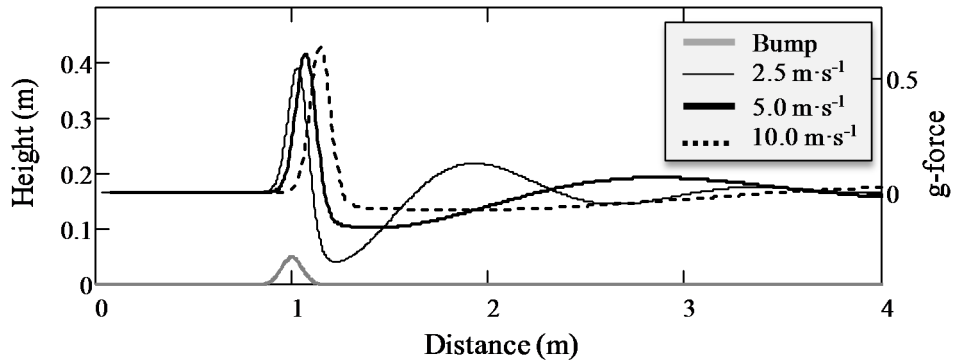

Figure 30. Accelerometer signal peaks relative to the bump peak at different vehicle speeds

The vehicle related bias $\bar{\varepsilon}_b$ results from the combined suspension and accelerometer frequency responses. These responses are essentially filters that delay the response from a bump excitation or forcing function. The GPS receiver related biases are its average longitudinal position $\bar{\varepsilon}_s$ of installation in the vehicle and the average position tag offset $\bar{\varepsilon}_{GPS}$. The RIF-transform has an expected signal processing related bias. The vehicle and sensor related biases vary randomly across vehicle manufacturers.

After traversing the isolated bump, the accelerometer signal output contains a first peak followed by transient oscillations from the vehicle body bounces as shown in Figure 30. Plots of the simulated inertial signal indicate the g-forces produced from the quarter-car responses at three different speeds. The next sections develop the error models in terms of the various signal-processing, vehicle, and sensor parameters.

5.5.1. Peak position delay

The modified radial basis function defined previously in Chapter 3 produced the simulated 5-cm-high bump plotted in Figure 30. The composite frequency response of the vehicle and the accelerometer transfer functions produce the first signal peak. The signal peak offset from the position of the bump's peak is a function of the phase response of the composite filter. Therefore, the peak delay increases proportionally with traversal speed as the frequency composition of the bump shifts toward higher frequencies.

The vertical acceleration produced by traversing the bump is the forcing function input to the composite filter representation of the vehicle and sensor. This simulated response uses the quarter-car suspension parameters estimated for the 2007 Toyota Camry LE used in the case studies. The results indicate that for the simulated suspension parameters, the first peak will offset at a rate that is approximately 1.5 cm per $m \cdot s^{-1}$ increase in longitudinal velocity. Therefore, the average offset $\bar{\varepsilon}_b$ of the first signal peak from the true position of the bump's peak is

$$\bar{\varepsilon}_b = 0.015\bar{v} \tag{70}$$

The corresponding variance $\sigma_{\varepsilon b}^2$ of the first peak offset is

$$\sigma_{\varepsilon b}^2 = (0.015)^2 \cdot \sigma_v^2 \tag{71}$$

The case study described later compares the relative contribution of this uncertainty to the overall precision of bump localization.

5.5.2. Digital signal processing related errors

The simulated vehicle response does not contain any modal responses or noisy vibrations beyond the quarter-car sprung-mass mode. Therefore, analysis of the case study data will apply a low pass finite impulse response (FIR) filter before identifying the position of the first peak in the signal after a bump traversal. The FIR filter delay $\bar{\varepsilon}_{DSP}$ is

$$\bar{\varepsilon}_{DSP} = N_{FIR} \frac{\bar{v}}{\bar{f}_A} \tag{72}$$

where N_{FIR} is the number of FIR filter taps and $\bar{f}_A$ is the average sample rate, which is the same as the inertial sensor sample rate.

The corresponding variance of the DSP filter delay $\sigma^2_{\varepsilon DSP}$ is

$$\sigma^2_{\varepsilon DSP} = \left(\frac{\partial \bar{\varepsilon}_{DSP}}{\partial \bar{v}} \sigma_v \right)^2 + \left(\frac{\partial \bar{\varepsilon}_{DSP}}{\partial f_A} \sigma_{fA} \right)^2 + 2 \cdot \mathrm{cov}[\bar{v}, f_A] = N_{FIR} \left[\left(\frac{1}{f_A} \sigma_v \right)^2 + \left(\frac{\bar{v}}{f_A^2} \sigma_{fA} \right)^2 \right] \tag{73}$$

where σ_v and σ_{fA} are the standard deviations of the vehicle speed and the inertial sensor sample rate, respectively. The covariance factors are zero because the accelerometer sample rate is independent of the vehicle's speed. The variance in accelerometer sample rate is a function of the signal processor's clock rate, which is negligibly small for most modern processors.

5.5.3. Sample interval related errors

The average sample interval is $\bar{\delta}_v = \bar{v} \cdot \bar{\tau}_A$ where the average sample period of the accelerometer signal is $\bar{\tau}_A$. Hence, the error in estimating the position of a signal peak within the

sample interval will be at most $\bar{\delta}_v$. If the distribution of the peak position is uniform within the sample interval, then the average error is

$$\bar{\varepsilon}_i = \frac{1}{2}\bar{v}\,\bar{\tau}_A = \frac{\bar{v}}{2\bar{f}_A} \tag{74}$$

Therefore, the variance $\sigma_{\varepsilon i}^2$ is

$$\sigma_{\varepsilon i}^2 = \left(\frac{\partial \bar{\varepsilon}_i}{\partial \bar{v}}\sigma_v\right)^2 + \left(\frac{\partial \bar{\varepsilon}_i}{\partial f_A}\sigma_{fA}\right)^2 + 2\cdot \mathrm{cov}[\bar{v}, f_A] = \left(\frac{1}{2f_A}\sigma_v\right)^2 + \left(\frac{\bar{v}}{2f_A^2}\sigma_{fA}\right)^2 \tag{75}$$

where the covariance factors are zero because the parameters are independent.

5.5.4. Sensor position

For ride quality monitoring applications, the inertial sensor position would be relative to the first axle that crosses the anomaly. Hence, distances behind the first axle are negative with respect to the velocity vector. When using a smartphone app to simulate a connected vehicle, the device would likely remain within reach of the driver. Hence, for an average arm span of 1.5 meters and an average operator position of 2 meters behind the first axle, the sensor's lateral position could range from -0.5 to -3.5 meters. If the distribution is normal then approximately six standard deviations will cover the entire range of reach such that the average distance $\bar{\varepsilon}_s$ is -2.0 meters. Hence, one standard deviation $\sigma_{\varepsilon s}$ must be approximately (-0.5 + 3.5)/6 = 0.5 meters. Eventually, connected vehicle applications are likely to have embedded inertial sensors at a standard position relative to the first axle that would minimize the position variance. However, this analysis will use the worst-case sensor position variance for a smartphone embodiment.

5.5.5. GPS tagging errors

The geospatial position tag $\bar{\varepsilon}_{GPS}$ reported by the GPS receiver and its associated embedded system consists of two error components such that the average position bias is

$$\bar{\varepsilon}_{GPS} = \bar{\varepsilon}_{dGPS} + \bar{\varepsilon}_{dlag} \tag{76}$$

The mean geospatial position bias is $\bar{\varepsilon}_{dGPS}$ and the mean position tag latency is $\bar{\varepsilon}_{dlag}$. The distribution of the geospatial position uncertainty from trilateration is Gaussian with zero mean (Gade 2010). Hence, the position bias becomes $\bar{\varepsilon}_{GPS} = \bar{\varepsilon}_{dlag}$.

From Equation (76), the total variance in geospatial position tagging σ^2_{GPS} is

$$\sigma^2_{GPS} = \sigma^2_{dGPS} + \sigma^2_{dlag} \tag{77}$$

The variance σ^2_{dGPS} of the geospatial position from errors in trilateration can be substantial because of random changes in atmospheric effects, multipath propagation, and GPS receiver performance. The variance also increases when the GPS receiver loses line-of-sight conditions with the satellites. GPS system administrators expect that the 95% confidence interval for horizontal position precision under direct line-of-sight conditions will be about 6.7 meters. However, this uncertainty could increase to more than 10 meters when multi-path reflections from buildings, large trees, and other tall structures distort the weak satellite signals.

System designers seldom report on the latency in position tagging $\bar{\varepsilon}_{dlag}$ or its variance σ^2_{dlag} because these parameters are highly dependent on the architecture and implementation details of a GPS receiver and its embedded host platform. Manufacturers generally retain such information as a trade secret. Some implementations provide a so-called “pulse-per-second” signal output that embedded platforms can use to estimate and remove some of the bias, although

not necessarily all of it (Solomon, Wang and Rizos 2011). The equivalent distance lag depends on the velocity of the vehicle such that

$$\bar{\varepsilon}_{dlag} = \bar{\tau}_{lag}\bar{v} \tag{78}$$

The average position tagging latency $\bar{\tau}_{lag}$ accumulates from delays through a cascade of processing blocks on the GPS electronic chip and the embedded platform. From Equation (78), the variance σ^2_{dlag} of the position tagging latency is

$$\sigma^2_{dlag} = \left(\bar{v}\sigma_{rlag}\right)^2 + \left(\bar{\tau}_{lag}\sigma_v\right)^2 \tag{79}$$

where σ_{rlag} is the tag latency standard deviation. The typical cascade of GPS processing blocks include hardware that receives and demodulates the satellite signals, synchronize carrier frequencies, measure the Doppler shift of the propagated radio wave, extract and decode satellite timing information, calculate the receiver position using trilateration techniques, and transfer the geospatial coordinates to the application host platform.

Satellites transmit their position and clock time once every six seconds. To provide position updates at a much faster rate, GPS receiver manufacturers incorporate a variety of techniques such as phase-locked-loops (PLLs) and Kalman Filters (USDHS 1996). Hence, a faster update rate does not necessarily improve the accuracy of the position estimate based on trilateration of the satellite's reported position and speed, but it does reduce the variability in position estimates.

The resulting latency in position tagging is the average time difference between locking on to at least four satellite signals and recording the position estimate from trilateration in application memory. Common GPS receivers in smartphones can update position estimates at a maximum rate of one hertz (Apple Inc. 2014) but require time for the satellite signals to

propagate through the various processing stages of the cascaded logic. GPS receivers that are more expensive can produce an estimate of position updates at rates higher than 10 hertz by implementing multiple GPS receiver channels and integrating additional sensors such as gyroscopes, accelerometers, and magnetometers to extend the Kalman Filter's predictive properties (O'Kane and Ringwood 2012). The tagging latency standard deviation σ_{tlag} is a function of time variations in the overall GPS signal processing chain. The asynchronous operation between the clocking of the application processor and the GPS receiver leads to variations in the geospatial coordinate "freshness" and fetch-to-tag times. The former is the time difference between coordinate deposit and retrieval from the output register of the GPS receiver. The fetch-to-tag time depends on the implementation of the application on the host platform and the number of active software threads that could affect the duration of an interrupt service. The freshness variance is likely to dominate when the GPS update interval is large relative to variations in the process duration of the interrupt service, for example, seconds versus tens of milliseconds. Hence, for a normally distributed coordinate freshness, the standard deviation will be approximately one-sixth of the GPS update interval $T_{\mu GPS}$ where

$$\sigma_{tlag} \cong T_{\mu GPS} / 6 \tag{80}$$

That is, the interval between nominal GPS updates is approximately six standard deviations. Substituting Equation (80) into Equation (79) and solving for the distance spread in tagging latency yields

$$\sigma_{dlag} = \sqrt{\left(\bar{v}\, T_{\mu GPS} / 6\right)^2 + \left(\bar{\tau}_{lag}\, \sigma_v\right)^2} \tag{81}$$

Hence, the distance spread from GPS tagging latency increases as the variance in vehicle velocity and the length of the GPS update interval increases.

5.5.6. Model for GPS update rate selection

From Equation (69) the position bias $\tilde{\upsilon}$ is a random variable where the average error is

$$\hat{\upsilon}_p - \upsilon_p = \tilde{\upsilon} = \left(\bar{\varepsilon}_{DSP} + \bar{\varepsilon}_i\right) + \bar{\varepsilon}_b + \left(\bar{\varepsilon}_s + \bar{\varepsilon}_{GPS}\right) = \left(\bar{\varepsilon}_{DSP} + \bar{\varepsilon}_i\right) + \bar{\varepsilon}_b + \left(\bar{\varepsilon}_s + \bar{\varepsilon}_{dlag}\right) \tag{82}$$

Hence, the variance of the peak position error σ_υ^2 is the sum of the variances of the individual uncertainties such that

$$\sigma_\upsilon^2 = \left(\sigma_{\varepsilon DSP}^2 + \sigma_{\varepsilon i}^2\right) + \sigma_{\varepsilon b}^2 + \left(\sigma_{\varepsilon s}^2 + \sigma_{GPS}^2\right) = \left(\sigma_{\varepsilon DSP}^2 + \sigma_{\varepsilon i}^2\right) + \sigma_{\varepsilon b}^2 + \left[\sigma_{\varepsilon s}^2 + \left(\sigma_{dGPS}^2 + \sigma_{dlag}^2\right)\right] \tag{83}$$

In scenarios where the GPS trilateration error dominates, the update rate selection should be such that the variance in position tagging remains smaller than the expected GPS position variance or

$$\sigma_{dlag}^2 \le \sigma_{dGPS}^2 \tag{84}$$

Substituting Equation (81) into Equation (84) and solving for the mean update interval yields

$$T_{\mu GPS} \le \frac{6}{\bar{v}} \sqrt{\sigma_{dGPS}^2 - \left(\bar{\tau}_{lag}\sigma_v\right)^2} \tag{85}$$

This result is intuitive because the application should decrease the update interval to accommodate larger variations in vehicle speed or smaller geospatial position spreads from trilateration. The next section quantifies this update rate for the case study application.

5.6. Case Study for GPS Receiver Selection or Adaptation

Isolated road bumps produce an easily detectable first peak response in the actual vertical acceleration signal. One of the main objectives of the case study is to characterize the distribution of the first peak position tags relative to the actual position of the bump along the traversal path. The selected bumps were a speed bump on a park road, a raised concrete-to-asphalt pavement joint on an airport access road, and an uneven rail grade crossing a local road.

Figure 31. Bumps traversed for this case study

Figure 31 shows street level views of the isolated bumps. Each bump interrupted relatively smooth, 30-meter road segments on either side to produce the localized roughness. The areas of uneven pavement joints and the rail grade crossing produced multiple signal peaks. However, the peak detection algorithm and selected thresholds indicated the position of only the first significant peak for each dataset. The technique to obtain and validate the coordinates of each bump involved resting the GPS receiver on top of them, computing the mean position reported, and then ensuring their agreement with coordinates reported in a local geographic information systems (GIS) database (North Dakota State Government 2014).

The park bump experiment incorporated a 2001 Ford Explorer SUV to collect inertial and GPS data at three different speeds. The airport access road experiments used a 2007 Subaru Legacy sedan to collect the eastbound (EB) and westbound (WB) traversal datasets. Traversals across the rail grade crossing used a 2007 Toyota Camry LE sedan to collect data. The smartphone data logging application (app) ran on an iPhone 4S with iOS® Version 7.1 and 8 GB memory. The app collected and stored the GPS coordinate updates, sensor orientation, vehicle velocity, the accelerometer samples, and a timestamp. The analysis excluded two data logs from the 30 traversals in each of the six datasets to remove outlier GPS position tags.

5.6.1. Distribution of first peak position

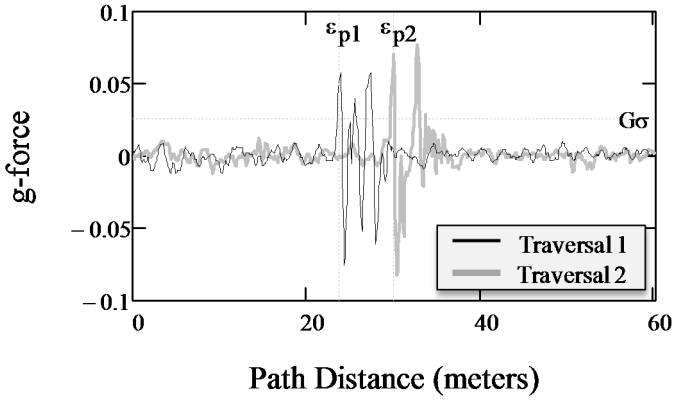

Figure 32. Accelerometer signal for two park bump traversals

Table 12. Parameters derived from the data of the six case studies

	Park Bump			Airport Road Bump		Tracks
Parameters	**2.5 m·s^{-1}**	**5 m·s^{-1}**	**7 m·s^{-1}**	**EB**	**WB**	**NB**
Batch mean speed, $\bar{\bar{v}}$ (m·s^{-1})	2.552	4.983	7.187	6.769	6.715	6.685
Batch mean spread, $\sigma_{\bar{v}}$ (m·s^{-1})	0.204	0.570	0.428	0.428	0.251	0.416
Suspension delay, $\bar{\varepsilon}_b$ (m)	0.038	0.075	0.108	0.102	0.101	0.100
Suspension delay, $\sigma_{\varepsilon b}$ (m)	0.003	0.009	0.006	0.006	0.004	0.006
DSP latency mean, $\bar{\varepsilon}_{DSP}$ (m)	0.246	0.481	0.693	0.654	0.648	0.649
DSP latency spread, $\sigma_{\varepsilon DSP}$ (m)	0.020	0.055	0.041	0.041	0.024	0.040
Interpolation, $\bar{\varepsilon}_i$ (m)	0.014	0.027	0.038	0.036	0.036	0.036
Interpolation, $\sigma_{\varepsilon i}$ (m)	0.001	0.003	0.002	0.002	0.001	0.002
Sensor position, $\bar{\varepsilon}_s$ (m)	-0.920	-0.920	-0.920	-0.710	-0.710	-0.710
G_z sample rate, f_A (hertz)	93.227	93.277	93.341	93.169	93.198	92.669
G_z rate spread, σ_{fA} (hertz)	0.097	0.070	0.101	0.073	0.103	0.077
GPS update rate, $T_{\mu GPS}$ (s)	1.009	1.004	0.993	0.986	0.988	1.015
GPS update spread, σ_{tlag} (s)	0.168	0.167	0.166	0.164	0.165	0.169
GPS tag spread, σ_{dlag} (m)	0.460	1.011	1.212	1.162	1.109	1.230
First peak offset, $\tilde{\upsilon}$ (m)	-2.712	-5.337	-3.944	-5.227	-2.334	-7.708
GPS tag lag, $\bar{\varepsilon}_{lag}$ (m)	-2.091	-4.999	-3.864	-5.309	-2.409	-7.784
GPS tag lag, $\bar{\tau}_{lag}$ (s)	**-0.819**	**-1.003**	**-0.538**	**-0.784**	**-0.359**	**-1.164**
First peak spread, σ_{υ} (m)	5.013	4.361	3.349	2.637	2.010	2.294
GPS spread, σ_{dGPS} (m)	**4.992**	**4.242**	**3.122**	**2.367**	**1.676**	**1.936**

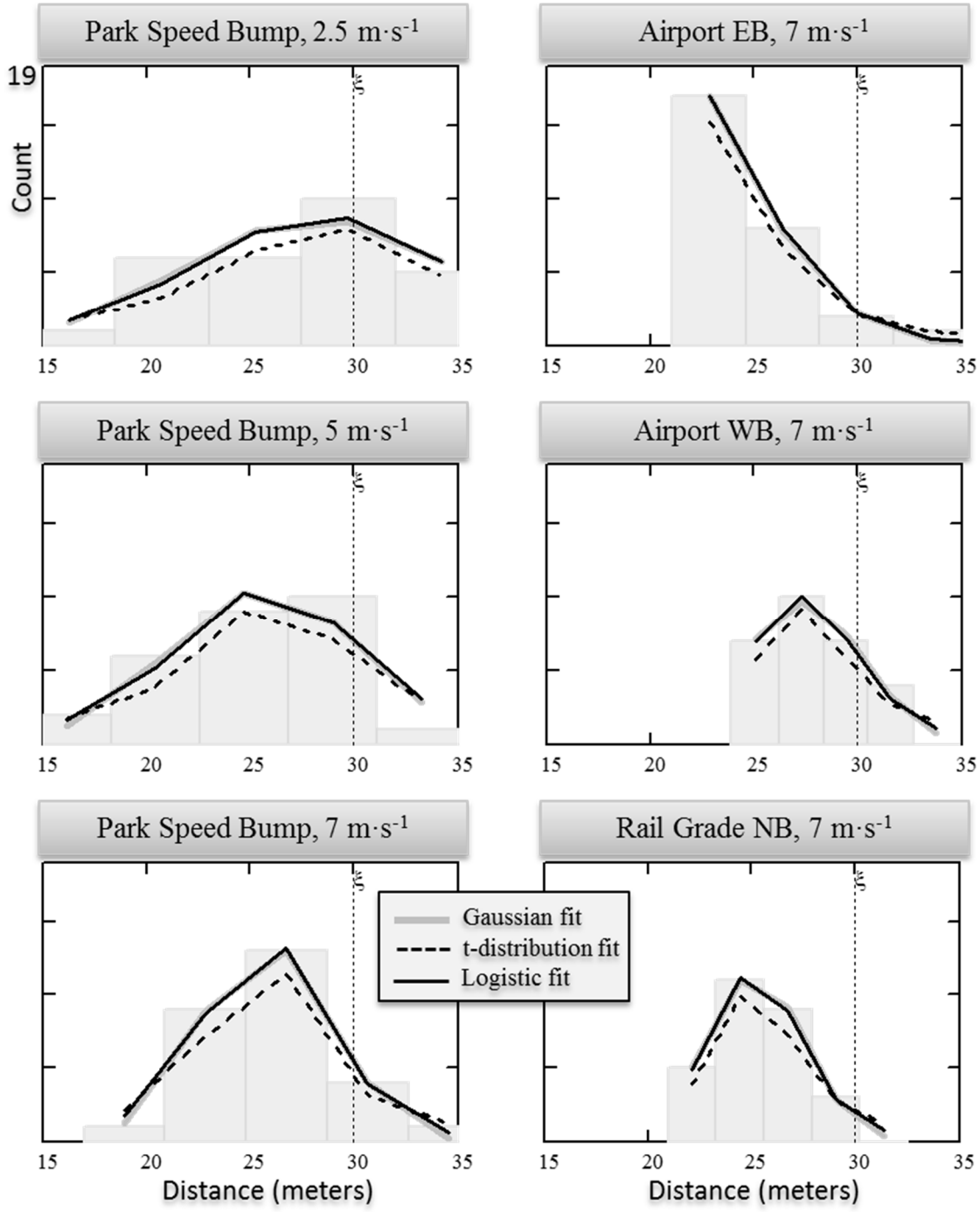

Figure 33. Distribution of first peak distribution and least squares fit

Table 12 summarizes the signal-processing, vehicle, and GPS receiver parameters derived for the six case studies. Figure 32 shows the FIR filtered accelerometer signal output

from two traversals of the park bump case study with traversal speeds of approximately 7 $m \cdot s^{-1}$. Figure 33 shows histograms of the first peak position tags for each case study.

Processing the data from all case studies required developing some custom software to determine the position tag of the first peak in the inertial signal. The algorithm located the first peak that exceeded a threshold $G\sigma$ set to about two standard deviations above the signal mean.

Table 13. Best fit parameters for distributions of the first peak position

	Park Bump			Airport Road Bump		Tracks
Parameters	**2.5 $m \cdot s^{-1}$**	**5 $m \cdot s^{-1}$**	**7 $m \cdot s^{-1}$**	**EB**	**WB**	**NB**
Gaussian						
df	2	2	2	2	2	2
$\chi 2$, α = 5%	5.991	5.991	5.991	5.991	5.991	5.991
$\chi 2$ Data	1.511	2.152	2.075	0.873	1.004	0.347
Significance α (%)	**46.986**	**34.103**	35.431	64.628	**60.527**	**84.062**
Amplitude	141.611	122.735	107.874	303.516	69.35	67.407
Mean	28.173	25.67	25.784	18.684	27.345	25.169
Standard Dev.	6.467	4.665	3.14	5.238	2.838	2.345
Student-t						
df	2	2	2	2	2	2
$\chi 2$, α = 5%	5.991	5.991	5.991	5.991	5.991	5.991
$\chi 2$ Data	3.071	3.574	1.534	1.064	2.626	2.135
Significance α (%)	21.534	16.744	46.438	58.745	26.901	34.391
Amplitude	166.519	143.144	120.988	130.934	81.315	77.353
Mean	28.59	26.102	25.542	23.254	27.262	25.191
Standard Dev.	6.415	4.658	2.839	2.661	2.835	2.255
Logistic						
df	2	2	2	2	2	2
$\chi 2$, α = 5%	5.991	5.991	5.991	5.991	5.991	5.991
$\chi 2$ Data	1.73	2.216	0.576	0.561	1.317	0.701
Significance α (%)	42.111	33.026	**74.974**	**75.53**	51.763	70.441
Amplitude	148.791	128.291	111.262	171.415	72.27	69.95
Mean	28.373	25.841	25.703	21.741	27.305	25.164
Scale	4.173	3.016	1.968	2.405	1.813	1.488

The plots of Figure 32 indicate the path distance tags of the first peaks from traversals 1 and 2 at the distance markers ε_{p1} and ε_{p2}, respectively. These positions are located at -6.2 and 0.1

meters relative to the actual position of the bump's peak at 30 meters. The position tags of the first peaks of the remaining 26 traversals randomly appear before or after the actual bump position. Table 12 indicates that the average position tag offset of the first peak $\tilde{\upsilon}$ from the true position of the bump's peak and the average spread σ_{υ} across all cases was -4.54 and 3.28 meters, respectively. The histogram plots of Figure 33 provide a visual indication of the average delay and spreads of the position tags for the inertial signal peak. The number of bins for each histogram is proportional to the typical guideline, which is the square root of the number of traversals available. A least squares fit of the Gaussian, Student-t, and logistic distributions superimpose each histogram. The fit for these three distributions are similar for all datasets.

Table 13 summarizes the parameters of the distribution fit and the associated chi-squared (χ^2) values for the hypothesis that the data are accordingly distributed. The table highlights the largest significance levels in bold font for each case study. The chi-squared method cannot reject the hypothesis that the distributions of the first peak follow the tested distributions. The mean distance lag persists across all datasets. These results promote a high level of confidence that the position tags distribute normally and that the mean value adequately characterize the distance lag in position tagging. The strong agreement with classic distributions indicates that the MOE for the mean distance lag will diminish with higher levels of vehicle traversals. The next sections evaluate the signal-processing, vehicle, and GPS receiver related biases and their spreads.

5.6.2. Digital signal processing related errors

Equations (72) and (73) provide the mean DSP filter delay $\bar{\varepsilon}_{DSP}$ and its standard deviation $\sigma_{\varepsilon DSP}$. The average delay and associated spread across all cases were 56 cm and 4 cm, respectively. Equation (74) provides the bias $\bar{\varepsilon}_i$ and (75) provides the uncertainty $\sigma_{\varepsilon i}$ in peak

position estimation given the sample rate of the accelerometer signal. The average sample rate was about 93 hertz, which was the highest rate practically achieved with the iOS data logger app. Across all cases, the average error bias and spread of the peak position in the signal were 31 and 2 millimeters, respectively.

5.6.3. Vehicle response related errors

For each case study, the first two rows of Table 12 list the batch means $\overline{\overline{v}}$ and the standard deviations $\sigma_{\bar{v}}$ of the average traversal speeds, respectively. The average speed variability across all case studies was 0.38 $m \cdot s^{-1}$ (less than 1 mph). Equations (70) and (71) provide the average response delay $\bar{\varepsilon}_b$ and delay spread $\sigma_{\varepsilon b}$, respectively, of the vehicle suspension relative to the first peak position. The average values across all case studies were 87 mm and 6 mm respectively.

5.6.4. Sensor position bias

The average bias in sensor position $\bar{\varepsilon}_s$ across all case studies was -0.82 meters. The driver of each vehicle fixed the sensor flat onto the dashboard for all traversals of each case study. Therefore, the position variance within each traversal set was zero. The three-dimensional rotation model of Equation (54) dynamically accounted for variations in the sensor orientation based on output from the integrated gyroscope of the smartphone to compute a resultant vertical acceleration from the three-axis accelerometer.

5.6.5. Geospatial position tag latency

Removing the expected biases from the mean of the first peak position bias provides an improved estimate for the position tagging latency as follows:

$$\bar{\varepsilon}_{dlag} = \tilde{\upsilon} - \left(\bar{\varepsilon}_{DSP} + \bar{\varepsilon}_i + \bar{\varepsilon}_b + \bar{\varepsilon}_s\right) \tag{86}$$

The residual offset was an average distance lag of -4.41 meters from tagging latency across all case studies. From Equation (78), the equivalent tagging latency was 0.78 seconds. Equation (81) provides the average spread in geospatial position tagging σ_{dlag} of 1.03 meters across all traversals.

5.6.6. Geospatial position spread

The geospatial position spread from trilateration errors is the residual variance after removing all the other quantifiable variances as follows:

$$\sigma^2_{dGPS} = \sigma^2_{\upsilon} - \left(\sigma^2_{\varepsilon DSP} + \sigma^2_{\varepsilon i} + \sigma^2_{\varepsilon b} + \sigma^2_{\varepsilon s} + \sigma^2_{dlag}\right) \tag{87}$$

The resultant is the geospatial position spread σ_{dGPS}. Its average value was 3.056 meters across all traversals. This uncertainty is consistent with the expected MOE for conventional GPS receivers (USDHS 1996). Systems that provide higher precision, such as differential GPS, use additional ground-based receivers at reference positions to derive and relay correction parameters that could yield sub-meter level precision in typical conditions, and even centimeter level precision in environments with less multi-path signal propagation.

5.6.7. Differential geospatial update spread

The position update intervals for a vehicle traveling at constant speed must be equidistant. Therefore, the difference in position update intervals for an error free system must be zero. The GPS receivers used for these case studies incorporate linear prediction using Kalman filtering to estimate position updates, based on the longitudinal velocity, longitudinal acceleration, and confidence intervals from past predictions. Therefore, the expected distribution of differential distance updates is zero mean and the variance will reflect variations in vehicle

speed and geospatial position tagging. The latter includes variances in position tagging latencies and the dilution of precision in geospatial position fixes from trilateration errors.

The embedded system must process interrupt requests more quickly for a faster GPS update rate setting. Therefore, the spread in position tag freshness must decrease accordingly. The vehicle speed is practically constant across sub-second intervals. Therefore, the minor speed variations across these short intervals will contribute negligibly to the differential distance spread. Given these considerations, the expected spread in differential distance updates will be lower for shorter GPS update intervals.

Table 14. Parameters measured for the intra-traversal geospatial position updates

		Park Bump		Tracks		MnROAD
Parameters	**2.5 m·s^{-1}**	**5 m·s^{-1}**	**7 m·s^{-1}**	**NB**	**SB**	**Cell 37**
Traversals, $N_{\bar{v}}$	28	28	28	7	5	6
GPS update rate, $T_{\mu GPS}$ (s)	1.009	1.004	0.993	0.500	0.500	0.499
GPS tag spread, σ_{dlag} (m)	0.460	1.011	1.212	1.997	1.527	1.383
Differential update, $\overline{\sigma}_{\Delta dn}$ (m)	1.760	2.975	2.904	**0.302**	**0.282**	**0.304**
Differential update, $\overline{\sigma}_{\Delta \tau n}$ (s)	0.690	0.597	0.404	0.038	0.044	0.018
First peak spread, σ_{υ}(m)	5.013	4.361	3.349	3.590	0.740	3.389
Ratio $\overline{\sigma}^2_{\Delta dn} / \sigma^2_{\upsilon}$	35.1%	68.2%	86.7%	8.4%	38.1%	9.0%
GPS tag latency, $\overline{\tau}_{lag}$ (s)	-0.819	-1.003	-0.538	-1.368	-1.914	-0.833

Table 14 summarizes the differential update spreads $\overline{\sigma}_{\Delta dn}$ for the park bump case studies at approximately one-second update intervals, and three others conducted with a more expensive GPS receiver capable of updating at approximately twice the rate, or equivalently approximately every half a second. The more expensive GPS receiver was available only for a limited time to collect data for a few traversals. Data collection included both northbound (NB) and southbound (SB) directions of the local road containing the rail grade crossing, and for Cell 37 of the

MnROAD facility (Bridgelall 2014). The data from each traversal contained thousands of differential distance updates to produce statistically significant measures. Therefore, it was unnecessary to include the data from all available traversals, but doing so nevertheless validated the consistency of the device operation across the available traversal sets.

The average of the differential distance update spread for the longer and shorter update intervals were 2.5 and 0.3 meters, respectively, thus supporting the theory. The equivalent time spreads $\overline{\sigma}_{\Delta m}$ were 600 and 30 milliseconds for the lower and higher update rates, respectively. The significantly smaller time spread of the higher performance receiver also reflects its greater consistency in processing interrupt service requests from the embedded GPS receiver.

The differential distance spread for the 2-hertz update rate cases were very consistent as highlighted in bold font in the table. The ratio of the differential distance update spread to the spread in first peak position $\overline{\sigma}^2_{\Delta dn} / \sigma^2_{v}$ is an indicator of its relative contribution to the overall spread in peak position tagging. The average ratio of differential distance update spread to first peak spread for the 1-hertz update cases was 63.3%, as compared with 18.5% for the 2-hertz update rate cases. The ratio for the SB traversal appears uncharacteristically high. However, this was because of the relatively low overall spread in position tagging (0.74 meters), even with only five traversals.

This experiment and the results validate the theory that, if affordable, increasing the GPS update rate will improve the geospatial coordinate freshness and reduce variations in the interrupt process time to minimize the overall spread in position tagging latency. The average latency bias, however, will not necessarily decrease and may even increase because higher quality GPS receivers tend to incorporate longer cascades of processing blocks to improve the navigational performance. Although some manufacturers of high performance GPS receivers

provide an additional signal (pulse-per-second) to aid in removing some of the latency in position tagging, most consumer-based platforms do not necessarily utilize that signal (Android Open Source Project 2014). As indicated on the last row of Table 14, the average latency in position tagging for the 1 hertz and 2 hertz update rate cases were -0.8 and -1.4 seconds, respectively. This indicates that, as expected, the higher update rate GPS receiver incorporated a longer cascade of processing blocks to enhance the precision of position updates.

5.6.8. Relative error contribution

Table 15. Summary of relative error contributions

	Park Bump			Airport Road Bump		Tracks
Parameters	**2.5 m·s^{-1}**	**5 m·s^{-1}**	**7 m·s^{-1}**	**EB**	**WB**	**NB**
First peak spread, σ_v (m)	5.013	4.361	3.349	2.637	2.010	2.294
Ratio, $\sigma_{sb}^2 / \sigma_v^2$	0.000%	0.000%	0.000%	0.001%	0.000%	0.001%
Ratio, $\sigma_{sDSP}^2 / \sigma_v^2$	0.002%	0.016%	0.015%	0.024%	0.014%	0.030%
Ratio, $\sigma_{si}^2 / \sigma_v^2$	0.000%	0.000%	0.000%	0.000%	0.000%	0.000%
Ratio, $\sigma_{dlag}^2 / \sigma_v^2$	0.842%	5.374%	13.097%	19.417%	30.442%	28.749%
Ratio, $\sigma_{dGPS}^2 / \sigma_v^2$	99.164%	94.617%	86.903%	80.571%	69.527%	71.224%

Table 15 summarizes the relative contribution of the individual error factors to the overall spread in geospatial position tagging. Variances in position tagging latency contributed 16.32% on average to the overall uncertainty in peak position while geospatial position spread from errors in trilateration contributed 83.668% of the uncertainty. Hence, for these case studies, the GPS trilateration errors were dominant. Applications have no control over the atmospheric and environmental factors that causes trilateration errors. Hence, to assure that no other error sources become dominant, the recommended GPS update interval for the case studies was at most 2.53 seconds. This value results from substituting the expected average GPS geospatial position

spread and position tagging latency for these cases, and a mean speed and standard deviation of 7 $m \cdot s^{-1}$ and 1 $m \cdot s^{-1}$, respectively, into Equation (85). Unlike the geospatial position spread from GPS trilateration, the tag latency error spread increases with vehicle speed. Hence, scanning for anomalies at highway speeds will increase the minimum update rate requirement. For example, at the worst-case speed of 35 $m \cdot s^{-1}$ and a speed variability of 1 $m \cdot s^{-1}$, the recommended update interval is 0.5 second.

Henceforth, to minimize energy consumption, data logging, and data transmission requirements, the GPS update rate may adapt in accordance with the model of Equation (85). Adaptation requires knowledge of the expected maximum geospatial error, the average position tagging latency of the sensor, the average traversal speed, and the expected velocity variations of the vehicle. This model and update rate recommendation is broadly applicable to applications that tag data from any sensor type with position coordinates derived from GPS receivers.

5.7. Summary

Sensor orientation and placement affects the signal quality. Applications that select a fixed sensor position and a rigid mount to some part of the vehicle's body will produce the best sensitivity to vehicle axle- and body-bounces. The sensor integrates roughness contributions from all wheel assemblies in proportion to its relative distance from them. A lateral position that is equidistant to each wheel path will average the roughness from each. An RIF-transform spatial resolution window that exceeds the wheelbase will desensitize the longitudinal position of the sensor. RIF-transforms that automatically produce and use the resultant vertical acceleration by accounting for the sensor orientation will produce the best quality signal for post-processing.

The EAR index derived from a fixed sample rate for the inertial sensors across all vehicle types will provide a more consistent characterization of ride quality. The minimum sample rate

should be at least twice the highest resonant mode of all vehicles traversing the segment. Frequency domain analysis of the inertial signal samples can provide a reliable estimate for the model parameters of a vehicle suspension system when their equivalent quarter-car model parameters are unknown. Given that standard design practices attenuate suspension responses to excitation frequencies above approximately 32 hertz, the sample rate recommended for standardization is 64 hertz.

The case study demonstrated that the margin-of-error of the RIF-index diminishes rapidly as the sample rate approaches this recommended rate and that further decreases beyond those rates provide diminishing returns. Given a sample rate and speed variance, the RIF-index variability diminishes as the inverse square root of the traversal volume. Therefore, the traversal volume needed for a desired level of EAR-index accuracy is proportional to the square of its standard deviation.

Selecting the maximum GPS update rate available will generally increase the receiver's power consumption and add to the data memory and wireless bandwidth requirements of the overall application. Conversely, a slower update rate could result in impractically large errors of anomaly localization, particularly when traveling at highway speeds. This chapter developed a model of the geospatial position tagging error for sensor integration applications and characterized the relative contributions from biases and variations in signal-processing, vehicle, and sensor parameters. The model selects a minimum update rate to minimize the overall localization error when expected values are available for delays in vehicle suspension responses and the processing latencies.

Specific case studies in roadway anomaly position tagging validated the overall model and quantified the achievable accuracy and precision under nominal conditions. Chi-squared

testing of the position tagging distribution for isolated road bumps showed excellent agreement with three classic distributions, namely the Gaussian, Student-t, and logistic. The data from vehicle traversals in six case studies provided a high level of confidence that the margin-of-error will diminish with larger vehicle traversal volume. For the scenario of traveling on local roads at the relatively low average speed and standard deviation of 7 $m \cdot s^{-1}$ and 1 $m \cdot s^{-1}$, respectively, the maximum recommended update interval was about 2.5 seconds. However, when monitoring for anomalies at maximum highway speeds, under typical conditions of satellite visibility and multipath, the recommended update interval was at most 0.5 seconds.

In general, sensor integration applications that tag sensed data with the geospatial coordinates of the sensor's position can benefit from an adaptive selection of the GPS update rate based on travel speed. Future work will examine the utility of the error models for applications involving remote sensing using unmanned aircraft systems (UAS).

CHAPTER 6. PERFORMANCE IN DETERIORATION FORECASTING

Transportation agencies rely on models to predict when pavements will deteriorate to an index of roughness that would trigger a maintenance action. The accuracy and precision of such forecasts are directly proportional to the frequency of monitoring. Roughness indices derived from connected vehicle data will enable transformational gains in both the accuracy and precision of deterioration forecasts because of the very high data volume and update rates achievable. This chapter develops precision bounds for the variance of the RIF-index and includes a case study to characterize performance as a function of variances in vehicle suspension and sensor parameters. The error bounds result from an analysis of the direct relationship between the inertial sensor signal and the vehicle mechanical responses.

6.1. Literature Review of Deterioration Forecasting Using Ride Indices

This is the first study to relate statistics of the RIF-indices to the precision of deterioration forecasts in connected vehicle environments (Bridgelall 2014). Consequently, literature on this specific method is limited. However, a significant volume of related work investigates the performance of the IRI and other measures of roughness as an explanatory variable in deterioration forecasting models. Related efforts calibrate the output of inertial sensor data from single vehicle traversals to estimate the IRI (Nagayama, et al. 2013) or attempt to train a neural network to produce an IRI estimate from accelerometer data (Dawkins, et al. 2011).

Numerous models of pavement deterioration forecasting exist. The most common are empirical regression of the IRI because they provide the greatest practical value and abstract the complexity of the underlying phenomena (Lu and Tolliver 2012). The scope of this chapter is to

study the utility of the RIF-index as an alternative to the IRI by applying it as an explanatory variable to a common regression model.

6.2. Sensor Output Variance

Models of pavement deterioration forecasting that use roughness indices as independent variables will exhibit uncertainties from the combined variances of those variables. Hence, a model that uses the EAR-index will inherit its statistics. Consequently, the precision of the forecasts will improve in proportion to the reduction in MOE of the EAR-index as the available traversal volume increases.

From Equation (64), the RIF-index is proportional to the product of the average traversal speed and the linear energy density of the inertial sensor signal energy. As described in Chapter 5, the signal energy from all wavelengths $E_{z\delta}$ would be the response to an impulse such that

$$E_{z\delta} = \int_0^\infty \left| g_{z\delta}(t) \right|^2 dt. \tag{88}$$

Substituting Equation (55) yields

$$E_{z\delta} = \frac{\gamma_g}{g} \int_0^\infty \left| \sum_{n=1}^{W_z} \beta_{z[n]} \left[\ddot{z}_{\delta s[n]}(t) + \rho_{\delta[n]} \ddot{z}_{\delta u[n]}(t) \right] \right|^2 dt. \tag{89}$$

For an impulse excitation $\rho_{\delta[n]}$= -1 and the expression becomes

$$E_{z\delta} = \frac{\gamma_g}{g} \int_0^\infty \left| \sum_{n=1}^{W_z} \sum_{m=1}^{2} \beta_{z[m,n]} \ddot{z}_{\delta[m,n]}(t) \right|^2 dt. \tag{90}$$

Using Fubini's theorem (Thomas and Finney 1995) to interchange the integration and summation operations yields

$$E_{z\delta} = \frac{\gamma_g}{g} \sum_{n=1}^{W_z} \sum_{m=1}^{2} \int_0^{\infty} \left| \beta_{z[m,n]} \ddot{z}_{\delta[m,n]}(t) \right|^2 dt \tag{91}$$

Substituting the closed-form solutions for the integration from Equations (45) and (46) yields

$$E_{z\delta} = \frac{\gamma_g}{g} \sum_{n=1}^{W_z} \sum_{m=1}^{2} \beta_{z[m,n]}^2 \omega_{[m,n]} \left(\zeta_{[m,n]} + \frac{1}{4\zeta_{[m,n]}} \right) \tag{92}$$

From the theory of error propagation (Ku 1966), the acceleration energy variance is

$$vE_{z\delta} = \sum_{n=1}^{W} \sum_{m=1}^{2} \left[\left(\frac{\partial E_{z\delta}}{\partial \omega_{[m,n]}} \right)^2 \sigma_{\omega[m,n]}^2 + \left(\frac{\partial E_{z\delta}}{\partial \zeta_{[m,n]}} \right)^2 \sigma_{\zeta[m,n]}^2 + \left(\frac{\partial E_{z\delta}}{\partial \omega_{[m,n]}} \right) \left(\frac{\partial E_{z\delta}}{\partial \zeta_{[m,n]}} \right) \sigma_{\omega\zeta[m,n]}^2 \right] \tag{93}$$

where $\sigma_{\omega[m,n]}^2$, $\sigma_{\zeta[m,n]}^2$ and $\sigma_{\omega\zeta[m,n]}^2$ are the variances of the mode resonant frequencies, damping ratios, and their covariance factors, respectively. The latter is zero because the resonant frequencies and damping ratios are statistically independent. Evaluating the partial derivatives indicated in Equation (93) and substituting the results yields

$$vE_{z\delta} = \sum_{n=1}^{W} \sum_{m=1}^{2} \beta_{z[m,n]}^4 \left[\left(\zeta_{\mu[m,n]} + \frac{1}{4\zeta_{\mu[m,n]}} \right)^2 \sigma_{\omega[m,n]}^2 + \omega_{[m,n]}^2 \left(\frac{1}{4\zeta_{\mu[m,n]}^2} - 1 \right)^2 \sigma_{\zeta[m,n]}^2 \right] \tag{94}$$

From Equation (64), the maximum RIF-index $R_{\bar{v}}^{\delta}$ from an impulse excitation is

$$R_{\bar{v}}^{\delta} = \bar{v} \sqrt{E_{z\delta}} \tag{95}$$

and from Equation (65) the standard deviation is

$$\sigma_{R\delta} = \sqrt{\bar{E}_{z\delta} \sigma_{\bar{v}}^2 + (\bar{v}/2)^2 \frac{vE_{z\delta}}{\bar{E}_{z\delta}}}. \tag{96}$$

The factors that account for the RIF-index variability are evident in this result. Intuitively, the expression indicates that when elevation profiles and vehicles are identical $vE_{z\delta} = 0$ and the

variance of the RIF-index $\sigma_{R\delta}^2$ is directly proportional to the average signal energy and the variance of the vehicle's speed. On the other hand, if the velocity is constant for all vehicle traversals such that $\sigma_{\bar{v}}^2 = 0$ then the standard deviation of the RIF-index is directly proportional to the average vehicle speed and the variance of the energy of the inertial signal relative to its average value.

6.3. Deterioration Forecasting Application

Research demonstrates that long-term evaluation of the IRI follows the exponential form (Haider, et al. 2010)

$$\psi(t) = \psi_0 \exp(\beta_L t) \tag{97}$$

where ψ_0 and $\psi(t)$ are respectively the initial and future values of ride-indices at time t. The calibration parameter β_L adjusts to best fit the historical ride-index measured for the segment of length L. Therefore, the expected time to reach a future index ψ_α is

$$\hat{T}(\psi_\alpha) = \frac{1}{\beta_L} \ln\left(\frac{\psi_\alpha}{\psi_0}\right). \tag{98}$$

The time window uncertainty or standard deviation $\sigma_{T\psi}$ of the forecasted roughness index is

$$\sigma_{T\psi} = \sqrt{\left[\frac{\partial T(\psi_\alpha)}{\partial \psi_\alpha}\right]^2 \sigma_{\psi\alpha}^2} = \frac{1}{\beta_L}\frac{\sigma_{\psi\alpha}}{\psi_\alpha} \tag{99}$$

where $\sigma_{\psi\alpha}$ is the precision of the future roughness index ψ_α.

6.3.1. Error bound of the RIF-index

When using the RIF-index, an impulse excitation produces the bound of the ratio $\sigma_{\psi\alpha}/\psi_\alpha$ where

$$\frac{\sigma_{\psi\alpha}}{\psi_{\alpha}} = \frac{\sigma_{R\delta}}{R^{\delta}_{\bar{v}}} \tag{100}$$

Substituting Equation (95) and (96) yields

$$\frac{\sigma_{\psi\alpha}}{\psi_{\alpha}} = \sqrt{\frac{\sigma^2_{\bar{v}}}{\bar{v}^2} + \frac{1}{4}\frac{vE_{z\delta}}{\overline{E}^2_{z\delta}}}. \tag{101}$$

This result is intuitive. It states that the maximum RIF-index spread as a percentage of its mean value is directly proportional to the sum of the respective spread proportions for the speed and inertial signal energy.

6.3.2. Precision as a function of traversal volume

The time MOE, ΔT_{ψ} is

$$\Delta T_{\psi} = \frac{\sigma_{T\psi} \times q_{1-\alpha/2}}{\sqrt{N^{P_j}_{\bar{v}[w]}}} \tag{102}$$

where $N^{P_j}_{\bar{v}[w]}$ is the traversal volume defined in Equation (31), and $q_{1-\alpha/2}$ is the standard normal quantile for a (1-α)% confidence interval (Papoulis 1991). Substituting $\sigma_{\psi\alpha}$ from Equation (99) yields

$$\Delta T_{\psi} = \frac{q_{1-\alpha/2}}{\sqrt{N^{P_j}_{\bar{v}[w]}}}\frac{1}{\beta_L}\frac{\sigma_{\psi\alpha}}{\psi_{\alpha}} \tag{103}$$

Solving for $N^{P_j}_{\bar{v}[w]}$ and substituting the results from Equation (101) yields

$$N^{P_j}_{\bar{v}[w]}(\Delta T_{\psi}) = \left(\frac{1}{\Delta T_{\psi}}\frac{1}{\beta_L}\frac{q_{1-\alpha/2}\sigma_{\psi\alpha}}{\psi_{\alpha}}\right)^2 = \left(\frac{1}{\Delta T_{\psi}}\frac{1}{\beta_L}\Delta R^{\delta}_{1-\alpha}\right)^2 \tag{104}$$

where $\Delta R^{\delta}_{1-\alpha}$ is the largest expected MOE of the RIF-index from an impulse excitation and a speed band. Hence $N^{P_j}_{\bar{v}[w]}(\Delta T_\psi)$ is the minimum traversal volume needed to achieve a minimum desired precision (maximum ΔT_ψ) of the estimated time when the pavement will deteriorate to a future ride-index that is lower than the bound such that $R^{L}_{\bar{v}} < R^{\delta}_{\bar{v}}$. Alternatively, given a deterioration rate parameter β_L, a mean RIF-index in the future, and its error band as a standard deviation, the precision ΔT_ψ within the desired confidence interval is

$$\Delta T_\psi = \frac{1}{\sqrt{N^{P_j}_{\bar{v}[w]}}}\left(\frac{1}{\beta_L}\right)\left(\frac{q_{1-\alpha/2}\times\sigma_{R\delta}}{R^{\delta}_{\bar{v}}}\right) = \frac{1}{\sqrt{N^{P_j}_{\bar{v}[w]}}}\left(\frac{1}{\beta_L}\right)\Delta R^{\delta}_{1-\alpha} \tag{105}$$

Intuitively, Equation (104) states that the minimum number of vehicle traversals needed for a given precision of forecast $N^{P_j}_{\bar{v}[w]}(\Delta T_\psi)$ is directly proportional to the square of the largest MOE expected of the future ride index. The minimum number of vehicle traversals needed is also inversely proportional to the square of the desired precision. Similarly, Equation (105) states that the achievable forecast precision is directly proportional to the largest MOE expected of the future ride index and inversely proportional to the vehicle volume needed. The precision improves with increasing vehicle volume.

6.4. Case Study of Deterioration Forecasting Precision Bounds

The case study utilized statistics of vehicle parameters available for a model year. Safety guidelines for suspension system designs provide the models to translate vehicle weight statistics to quarter-car parameter statistics. The resulting parameter spreads provide a quantification of the maximum RIF-index MOE that subsequently enables a scenario analysis for typical vehicle volumes.

6.4.1. Vehicle suspension statistics

Automotive engineers distribute the sprung- and unsprung-masses so that they account for 90% and 10%, respectively, of the gross vehicle weight (T. D. Gillespie 2004). This design guideline achieves the desired suspension system response that complies with international standards for human comfort and safety. The average curb weight of vehicles increased steadily since 1985 and peaked in 2007 (Bastani, Heywood and Hope 2012). Trends indicate that they are likely to return to 1990 levels by 2015. Table 16 lists the average and standard deviation of the gross mass for vehicles manufactured in 2007 (Woodyard 2007).

Engineers also design the sprung-mass resonant frequency between 0.9 and 1.5 hertz for all vehicle types (General Motors 1987). Similarly, vehicle suspension shock absorbers produce sprung-mass damping ratios in the range of 0.3 to 0.4. These ranges represent approximately six standard deviations for a normal distribution.

Table 16. Statistics for typical vehicles manufactured in 2007

Parameter	Value
Gross mass, average ($m_{\mu G}$)	2226 kilograms
Gross mass, standard deviation (σ_{mG})	483.7 kilograms
Sprung mass resonant frequency, mean ($\omega_{\mu s}/2\pi$)	1.2 hertz
Sprung mass resonant frequency, standard deviation ($\sigma_{\omega s}/2\pi$)	0.1 hertz
Sprung mass damping ratio, mean ($\zeta_{\mu s}$)	0.35
Sprung mass damping ratio, standard deviation ($\sigma_{\zeta s}$)	0.02
Unsprung-mass resonant frequency, mean ($\omega_{\mu u}/2\pi$)	9.97 hertz
Unsprung-mass resonant frequency, standard deviation ($\sigma_{\omega u}/2\pi$)	1.53 hertz
Unsprung-mass damping ratio, mean ($\zeta_{\mu u}$)	0.23
Unsprung-mass damping ratio, standard deviation ($\sigma_{\zeta u}$)	0.08

Table 16 summarizes the mean and standard deviation of the resonant frequency parameters. The derivations that follow provide the values listed in Table 16 for the unsprung-mass statistics. A tire at its rated load will experience a deflection of approximately 25 mm

(Gillespie 2004). Therefore, an estimate of the average unsprung-mass spring stiffness $k_{\mu u}$, in units of $N \cdot m^{-1}$ for four-wheeled vehicles is

$$k_{\mu u} = \frac{\left(m_{\mu G}/4\right)g}{0.025} \tag{106}$$

where g is the g-force constant of 9.8 $m \cdot s^{-2}$ and $m_{\mu G}$ is the average gross mass of the vehicles.

The mean unsprung-mass resonant frequency, $\omega_{\mu u}$, is therefore

$$\omega_{\mu u} = \sqrt{\frac{k_{\mu u}}{m_{\mu u}}} \tag{107}$$

where $m_{\mu u}$ is the average unsprung-mass. From the gross mass statistics listed in Table 16, the associated average resonant frequency of the unsprung-mass mode is approximately 10 hertz. Its standard deviation $\sigma_{\omega u}$ is

$$\sigma_{\omega u} = \sqrt{\left(\frac{\partial \omega_{\mu u}}{\partial k_{\mu u}}\right)^2 \sigma_{ku}^2 + \left(\frac{\partial \omega_{\mu u}}{\partial m_{\mu u}}\right)^2 \sigma_{mu}^2 + \left(\frac{\partial \omega_{\mu u}}{\partial k_{\mu u}}\right)\left(\frac{\partial \omega_{\mu u}}{\partial m_{\mu u}}\right)\sigma_{km}^2}\,. \tag{108}$$

For this scenario, both $k_{\mu u}$ and $m_{\mu u}$ depend on the gross vehicle mass statistics, therefore, the covariance factor is unity and the expression becomes

$$\sigma_{\omega u} = \sqrt{\frac{1}{4k_{\mu u}m_{\mu u}}\sigma_{ku}^2 + \frac{k_{\mu u}}{4m_{\mu u}^3}\sigma_{mu}^2 - \frac{1}{4m_{\mu u}^2}}\,. \tag{109}$$

The average damping-ratio for the unsprung-mass $\zeta_{\mu u}$ is

$$\zeta_{\mu u} = \frac{c_{\mu u}}{2\sqrt{m_{\mu u}k_{\mu u}}} = \frac{c_{\mu u}}{2m_{\mu u}\omega_{\mu u}}\,. \tag{110}$$

The unsprung-mass damping coefficient $c_{\mu u}$ is typically $\eta = 15\%$ of the sprung-mass damping coefficient $c_{\mu s}$ (Türkay and Akçay 2008). Therefore,

$$\zeta_{\mu u} = \frac{\eta c_{\mu s}}{2 m_{\mu u} \omega_{\mu u}} = \frac{\eta \left(2 m_{\mu s} \omega_{\mu s} \zeta_{\mu s} \right)}{2 m_{\mu u} \omega_{\mu u}} = \eta \zeta_{\mu s} \frac{m_{\mu s}}{m_{\mu u}} \frac{\omega_{\mu s}}{\omega_{\mu u}} \tag{111}$$

where $m_{\mu s}$, $\omega_{\mu s}$, and $\zeta_{\mu s}$ are the means of the sprung-masses, their resonant frequencies, and their damping ratios, respectively. Hence, the standard deviation of the unsprung-mass damping ratio $\sigma_{\zeta u}$ is

$$\sigma_{\zeta u} = \sqrt{\left(\frac{\partial \zeta_{\mu u}}{\partial \zeta_{\mu s}} \right)^2 \sigma_{\zeta s}^2 + \left(\frac{\partial \zeta_{\mu u}}{\partial \omega_{\mu s}} \right)^2 \sigma_{\omega s}^2 + \left(\frac{\partial \zeta_{\mu u}}{\partial \omega_{\mu u}} \right)^2 \sigma_{\omega u}^2 + \left(\frac{\partial \zeta_{\mu u}}{\partial m_{\mu s}} \right)^2 \sigma_{ms}^2 + \left(\frac{\partial \zeta_{\mu u}}{\partial m_{\mu u}} \right)^2 \sigma_{mu}^2 + \Delta_{cv}} \tag{112}$$

where the covariance term Δ_{cv} is

$$\Delta_{cv} = \left(\frac{\partial \zeta_{\mu u}}{\partial m_{\mu s}} \right) \left(\frac{\partial \zeta_{\mu u}}{\partial m_{\mu u}} \right) \sigma_{msmu}^2 + \left(\frac{\partial \zeta_{\mu u}}{\partial m_{\mu s}} \right) \left(\frac{\partial \zeta_{\mu u}}{\partial \omega_{\mu u}} \right) \sigma_{ms\omega u}^2 + \left(\frac{\partial \zeta_{\mu u}}{\partial m_{\mu u}} \right) \left(\frac{\partial \zeta_{\mu u}}{\partial \omega_{\mu u}} \right) \sigma_{mu\omega u}^2 \tag{113}$$

The guidelines for typical vehicle suspension designs link the variables $m_{\mu s}$, $m_{\mu u}$, and $\omega_{\mu u}$. Therefore, the covariance factors σ_{msmu}, $\sigma_{ms\omega u}$, and $\sigma_{mu\omega u}$ are each unity. Evaluating the partial derivatives indicated, and simplifying yields

$$\Delta_{cv} = \left(\eta^2 \zeta_{\mu s}^2 \frac{m_{\mu s}}{m_{\mu u}} \frac{\omega_{\mu s}^2}{\omega_{\mu u}^2} \right) \left[\frac{m_{\mu s} - m_{\mu u} - \omega_{\mu u}}{m_{\mu u}^2 \omega_{\mu u}} \right] \tag{114}$$

Table 17. Ratio of standard deviation to mean value for typical vehicles

Parameter	Sprung Mass	Unsprung Mass
Resonant Frequency (ω)	8.3%	15.4%
Damping Ratio (ζ)	4.8%	35.7%
Spring Stiffness (k)	27.4%	21.7%
Damping Coefficient (c)	18.1%	18.1%

Table 17 summarizes the ratios of standard deviations to mean values for the sprung- and unsprung-mass parameters of this case study. The energy variance to mean ratio $vE_{z\delta} / \bar{E}_{z\delta}$ of Equation (96) is now quantifiable with these typical quarter-car statistics. Subsequently,

Equation (104) will produce the maximum number of sensor readings needed for a specified level of forecast precision and confidence interval for a speed band and the historical rate of pavement deterioration. The next section provides a quantification for this typical scenario.

6.4.2. Application of the forecasting precision bounds

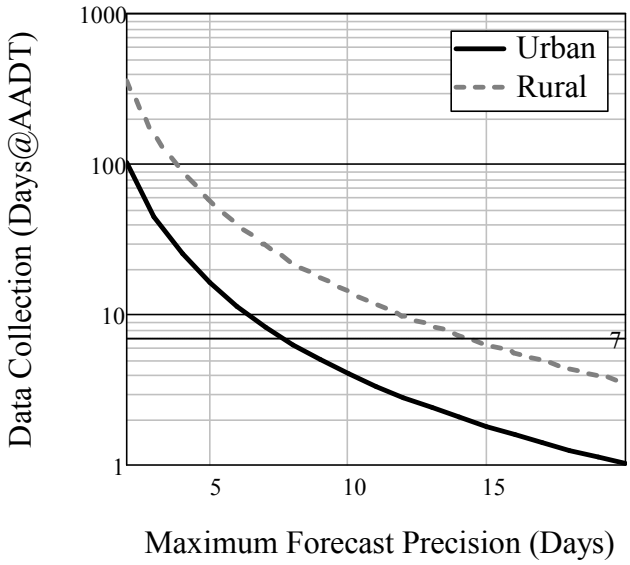

Figure 34. Data collection time needed for forecast precision at 95% confidence

Evaluating Equation (104) using the parameters of Table 16 for the typical vehicle mix illustrates the fundamental trade-off in data collection time and achievable forecast precision. Figure 34 plots the data collection time in terms of the number of data collection days required for a desired maximum forecast precision, within a 95% confidence interval.

This result uses a speed band where the average speed is 24.6 m/s (55 mph) and the standard deviation is 5%. The number of data collection days depend on the Annual Average Daily Traffic (AADT) volume medians of 10,965 and 39,093 passenger cars per lane for rural and urban interstate facilities respectively (Hausman and Clarke 2012), and a scenario where only 20% of the vehicles provide the inertial data. The result also incorporates typical rural and urban interstate highway deterioration rates (Anastasopoulos, Mannering and Haddock 2009)

that correspond to β_L values of 0.056 and 0.055 respectively. The plot indicates that one week of data collection under these circumstances will forecast RIF-indices with a worst-case precision of one and two weeks for the typical urban and rural interstates, respectively. The actual precision achieved will be better than this bound which represents an impulse excitation or equivalently, broadband potential energy from the elevation profile. Precision will also improve for the same data collection period as more vehicles participate.

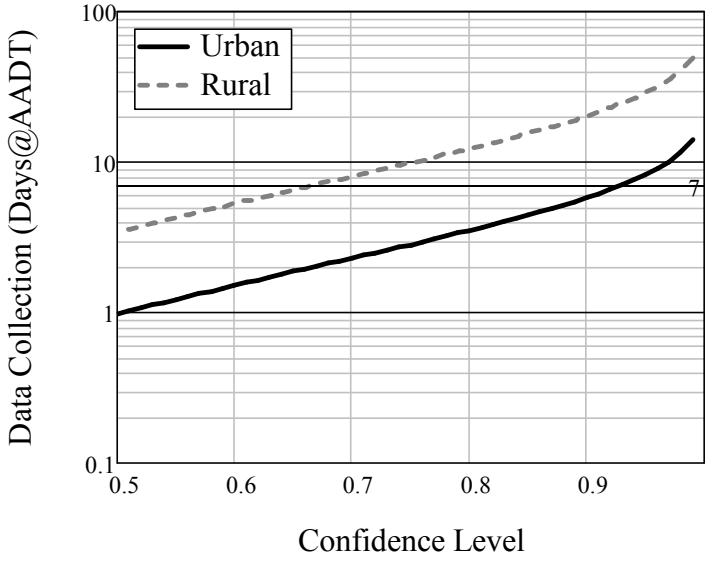

Figure 35. Data collection needed for a precision of one week with varying confidence

For the same AADT scenario, Figure 35 plots the data collection time needed to achieve a precision of one week within confidence levels ranging from 50% to 99%.

6.5. Summary

The ability to collect and process data from a large number of inertial sensors in a connected vehicle environment will provide transformational gains in the precision and accuracy of forecasting pavement deterioration. Fundamentally, the accuracy and precision of a regression model's ability to predict pavement deterioration is directly proportional to the rate of its recalibration with updated ride quality data. As observed in the model, statistical properties

of the RIF-index inherently improves forecast precision as data volume increases, making it ideal for application in a connected vehicle environment.

This analysis provides theoretical insights that relate the statistics of vehicle motion parameters to bounds of the forecast precision. The maximum possible excitation from an impulse provided the theoretical maximum MOE for RIF-index variability. An inversion of the empirical model to forecast deterioration provided the precision in time units as a function of the MOE for the RIF-index. The supporting case study used suspension parameter variances available for vehicles manufactured in 2007. The analysis incorporated a scenario of 20% sensor participation rate from passenger cars traveling a typical U.S. interstate highway, at a common speed limit. The model indicated that after collecting RIF-index data for about one week, the future ride-index is predictable within one weeks of the time expected to reach that value, within a 95% confidence interval. The accuracy is a function of the calibration parameter fit to the historical ride-index data for the segment. In general, increasing the level of desired precision would require an exponential increase in the number of data collection days. Consequently, the lower data volume of rural roads will require more data collection time to achieve the same precision of forecasting deterioration as for urban roads.

CHAPTER 7. PERFORMANCE FOR ANOMALY LOCALIZATION

With infrequent assessments of ride quality, transportation agencies miss important vulnerabilities such as frost heaves that appear and disappear between monitoring cycles. Most agencies rely on the public to report the location and type of defects for unmonitored facilities such as local and unpaved roads. Unfortunately, agencies often learn about these anomalies after they begin to cause congestion or crashes. The unexpected appearance of anomalies can cause drivers to reduce speed and/or direction abruptly. Such actions tend to create dynamic capacity bottlenecks and unsafe roadway conditions (FHWA 2011).

The multi-resolution feature of the RIF-transform identifies localized roughness within an adjustable spatial resolution window. Increases in traversal volume improve the precision of anomaly localization by reducing the variance of the RIF-index. This chapter derives the precision bounds of the RIF-transform to localize roadway anomalies when using standard GPS receivers. Error factors include variances from GPS location tagging, vehicle speed, suspension parameters, and sensor characteristics (Bridgelall 2014). The first case study of this chapter incorporates data from traversals across a rough rail grade crossing to demonstrate and characterize the localization capabilities of the multi-resolution feature. Six additional case studies use the multi-resolution model to characterize its localization accuracy for narrower anomalies such as road bumps. The case studies revealed that vehicle suspension transient motion and sensor latencies are the dominant factors in estimating the position of anomalies.

7.1. Literature Review of Roadway Anomaly Position Estimates

Connected vehicles provide immense opportunities to enable new participatory sensing approaches that could substantially lower the cost of network-wide roadway performance monitoring. The probe data will become inexpensive, real-time, and available for all facilities by

collecting and processing time, inertial, and geospatial position data from onboard sensors (Bridgelall 2014). This realization has motivated researchers worldwide to develop smartphone applications that simulate the probe data that connected vehicles would provide. Smartphones embed the accelerometers and GPS receivers needed for anomaly identification. However, the techniques developed and their performances vary widely. Most of the reported research focuses on the accuracy of various algorithms to detect anomalies from their features in the inertial data of individual traversals (Ayenu-Prah and Attoh-Okine 2009). Algorithms range from blind signal data mining of heuristic features (Chen, Zhang and Lu 2011) to complex temporal template matching using Wavelet transforms (Wei, Fwa and Zhe 2004). Other ongoing research focuses on the accuracy of classifying anomaly types by the shape of their inertial signatures (Gónzalez, Martínez and Carlos 2014). However, there are no reports of sensor data integration and compression methods that merge multiple streams of inertial data to improve the localization precision by capitalizing on statistical properties of the data. Only one study attempted to fuse the data from multiple traversals, but the focus was on increasing signal quality, not localization accuracy (Ndoye, et al. 2011). In general, the literature lacks information about the localization accuracy of algorithms to identify anomalies using inertial and GPS probe data.

7.2. Multi-resolution Feature

The RIF-transform reports localized g-forces by replacing the segment length L in Equation (28) with a resolution window ΔL such that the short-time transform becomes

$$R_{\bar{v}}^{\Delta L} = \sqrt{\frac{1}{\Delta L}\int_{0}^{\Delta L/\bar{v}} \left| g_z(t)v(t) \right|^2 dt} \tag{115}$$

and the EAR-index $\overline{R}_{\bar{v}}^{\Delta L}$ becomes

$$\overline{R}_{\bar{v}}^{\Delta L} = \frac{1}{N_v} \sum_{\rho=1}^{N_v} R_{\bar{v}}^{\Delta L}[\rho]. \tag{116}$$

The data processing algorithm tags the RIF-index with an interpolated path distance derived from the GPS receiver, the timer, and the velocity updates. The EAR-index is the average of RIF-indices at the same position tag across all traversals. Therefore, EAR-index peaks are position estimators for anomalies.

The multi-resolution RIF-transform provides a data compression functionality that reduces the time, inertial, and geospatial dataset by integrating the accelerometer signal energy within each resolution window for all traversals in the selected speed band. Anomalies produce inertial signal peaks followed by the transient responses of the vehicle suspension system. The RIF-transform integrates roughness from both the inertial signal peak and the vehicle transient responses that follow. Therefore, the position of the anomaly causing the inertial event will precede EAR-indices that represent only transient responses. Equation (70) provides the offset of the inertial signal peak from the position of the anomaly. The duration of the transient response is a function of the vehicle suspension parameters. Hence, without *a priori* information about anomalies, the tagged position of peak EAR-indices provides the best estimate for the position anomalies.

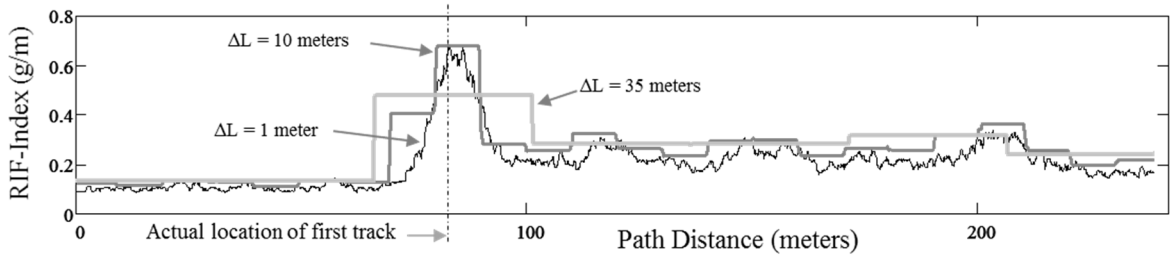

Figure 36. The EAR of Bolley Drive at resolutions of 1, 10, and 35 meters

The intensity of the EAR-index peak provides an indication of relative roughness of the anomaly that produced it. The next section investigates the expected error magnitude of the

position estimate for the peak EAR-index. Figure 36 is an example of the multi-resolution RIF-transform and associated EAR-indices for the Bolley Drive rail grade crossing. Windows of length 1, 10, and 35 meters illustrate the average g-force sensed within those distances, respectively. The minimum window size is a function of the accelerometer sample rate because it is the minimum distance resolution from interpolating between GPS receiver updates. Practically, a spatial resolution that is better than one meter may be unnecessary for the visual identification of anomalies in the field. The maximum window size is the length of the entire segment for which contiguous samples are available. Each of the plots of Figure 36 averages the RIF-indices from 28 traversals. The EAR-indices distribute about the true position of the rail grade crossing as indicated. For this case study, peak EAR-index was located within one meter of the first track position. The standard deviation of the EAR-indices about the peak was 3.6 meters. Hence, the spatial distribution of the EAR-indices provides a visual representation of the localization uncertainty for anomalies. Color or grayscale coding the intensity of the EAR-indices for GIS integration will provide a suitable visualization of the roughness intensity levels along a route. An important and desirable feature of this method of ensemble averaging is that the delineation between rough spots will become sharper with additional traversal volume because of the associated MOE reduction.

7.3. Anomaly Position Estimate

The position of the peak EAR-index $\hat{\upsilon}_r$ includes biases relative to the true peak position υ_p such that

$$\hat{\upsilon}_r = \upsilon_p + \left(\Delta L + \bar{\varepsilon}_r\right) + \left(\bar{\varepsilon}_s + \bar{\varepsilon}_{GPS}\right) + \bar{\varepsilon}_d \tag{117}$$

That is, the position estimator $\hat{\upsilon}_r$ contains biases from signal processing, sensor, and vehicle related parameters. The biases are: a) the integration window ΔL of the RIF-transform and the average interpolation sub-interval $\bar{\varepsilon}_r$, b) the average longitudinal sensor position $\bar{\varepsilon}_s$ and the average latency $\bar{\varepsilon}_{GPS}$ of the position tag, and c) the average transient response distance $\bar{\varepsilon}_d$ that contains roughness from the system transient responses. The next sections derive the model for each error factor.

7.3.1. Signal processing biases

Before performing an ensemble average, the algorithm interpolates the RIF-indices of each traversal to produce a higher resolution grid for GIS map registration and data visualization. The user sets the display resolution preference that determines the length of each interpolation sub-interval δ_r. Hence, the error in estimating the position of a peak EAR-index within the interpolated sub-interval will be at most δ_r. The case studies of this chapter set the RIF-transform integration window ΔL to 1 meter and the interpolation sub-interval δ_r to 0.1 meters. If the distribution of the EAR-indices is uniform within the sub-interval then the average error is

$$\bar{\varepsilon}_r = \frac{1}{2}\delta_r \tag{118}$$

The variance of the position of peak EAR-indices $\sigma^2_{\varepsilon r}$ within the sub-interval is practically zero for a typical high-resolution display.

7.3.2. Transient response bias

At the position of the sensor, the g-forces from vehicle body bounces dominate those of the axle bounces. Equations (3) and (23) in Chapter 3 provide the bump and quarter-car response models, respectively. The quarter-car parameters used for this simulation are estimates

for the Toyota Camry 2007 LE sedan used for data collection. Chapter 5 describes the procedure used to estimate the quarter-car parameters from the inertial data.

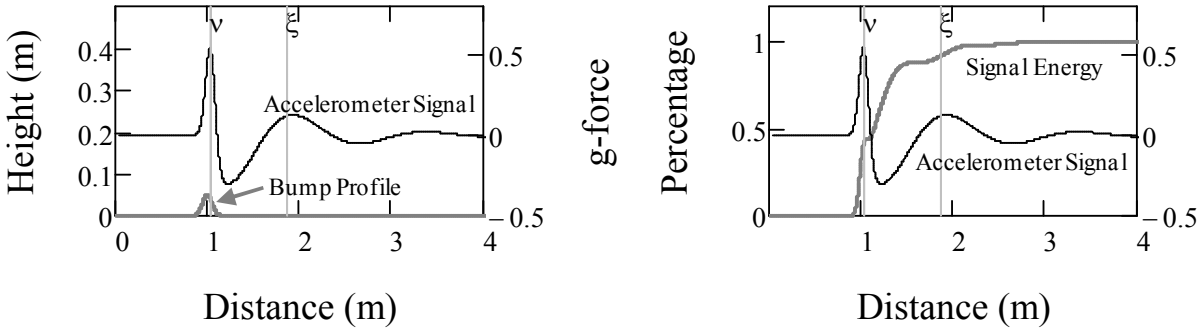

Figure 37. a) Simulated g-force and b) signal energy for a bump response

The first chart of Figure 37 shows the simulated g-forces that a quarter-car produces when traversing a 5 cm × 30 cm bump at 2.5 $m \cdot s^{-1}$. The second chart of the figure shows the accumulated accelerometer signal energy as a percentage of the maximum signal energy. The first peak of the accelerometer signal shown at the distance marker υ in Figure 37 is the vertical acceleration during the time that the bump is producing a forcing function on the damped mass-spring system. The phase response of the composite quarter-car and sensor filters briefly delays this first peak from the actual position of the bump's peak.

Figure 30 in Chapter 5 showed the first peak delay as a function of vehicle speed. Starting from the first dip, the remaining signal represents the g-forces from the transient response motion of the sprung-mass. At higher speeds, the mechanical filtering action of the quarter-car absorbs the forcing function portion of the inertial signal. Figure 7 in Chapter 3 demonstrated this situation for the 8 × $\bar{v}$ traversal where the quarter-car produced only the transient response portion of the bump excitation. The RIF-transform integrates the inertial response energy within the resolution window, and this will often include the energy from transient responses that extend beyond the actual position of the inertial event. Hence, for

relatively small resolution windows, the position of the peak EAR-index could be associated with the transient response from roughness encountered at some distance behind.

As indicated in the second chart of Figure 37, the duration to the first peak of the transient response portion of the signal, indicated at marker ξ, contains more than 90% of the inertial response energy. Therefore, this first peak of the transient response portion of the inertial signal will tend to dominate the position bias of the peak EAR-index. The second derivative of the sprung-mass impulse response $\ddot{z}_{\delta s}(t)$ characterizes the maximum transient response duration. Taking the second derivative of Equation (39) provides the sprung-mass transient response as

$$\ddot{z}_{\delta s}(t) = u(t)\omega_s \exp\left(-\zeta_s \omega_s t\right)\left[\frac{2\zeta_s^2 - 1}{\sqrt{1-\zeta_s^2}}\sin\left(\omega_s t\sqrt{1-\zeta_s^2}\right) - 2\zeta_s \cos\left(\omega_s t\sqrt{1-\zeta_s^2}\right)\right]. \tag{119}$$

From trigonometric identities (Thomas and Finney 1995), the combination of the two sinusoids of Equation (119) is equivalent to a single sinusoid of the same frequency and an average phase shift of $\overline{\vartheta}_{dr}$ radians where

$$\overline{\vartheta}_{dr} = \left[\pi - \arctan\left(\frac{2\zeta_{\mu s}}{2\zeta_{\mu s}^2 - 1}\sqrt{1-\zeta_{\mu s}^2}\right)\right]. \tag{120}$$

Therefore, the average position of the first peak of the transient response is the product of one resonant mode cycle distance $\overline{v}/\left(f_{\mu s}\sqrt{1-\zeta_{\mu s}^2}\right)$ and the phase shift portion of a full cycle, which is $\overline{\vartheta}_{dr}/2\pi$. Therefore, transient response bias is

$$\overline{\varepsilon}_d = \frac{\overline{v}}{f_{\mu s}\sqrt{1-\zeta_{\mu s}^2}}\left[\frac{1}{2} - \frac{1}{2\pi}\arctan\left(\frac{2\zeta_{\mu s}}{2\zeta_{\mu s}^2 - 1}\sqrt{1-\zeta_{\mu s}^2}\right)\right]. \tag{121}$$

Hence, the variance of the transient response bias $\sigma_{\varepsilon d}^2$ is

$$\sigma_{\varepsilon d}^2 = \left(\frac{\partial \bar{\varepsilon}_d}{\partial \bar{v}}\sigma_v\right)^2 + \left(\frac{\partial \bar{\varepsilon}_d}{\partial f_{\mu s}}\sigma_{fs}\right)^2 + \left(\frac{\partial \bar{\varepsilon}_d}{\partial \zeta_{\mu s}}\sigma_{\zeta s}\right)^2 + 2\cdot \mathrm{cov}\left[\bar{v}, f_{\mu s}, \zeta_{\mu s}\right] \tag{122}$$

where $\sigma_{\zeta s}$ and σ_{fs} are the standard deviations of the sprung-mass damping ratio and resonance frequency, respectively. The last term of Equation (122) contains the covariance factors. These parameters are independent for nominal suspension system operation; hence, the covariance is zero. After evaluating the partial derivatives, Equation (122) becomes

$$\begin{aligned}\sigma_{\varepsilon d}^2 = &\left(\frac{\bar{v}}{2\pi f_{\mu s}}\right)^2 \left(\frac{\arctan\left[\frac{2\zeta_{\mu s}\sqrt{1-\zeta_{\mu s}^2}}{2\zeta_{\mu s}^2-1}\right]-\pi}{\sqrt{1-\zeta_{\mu s}^2}}\right)^2 \left(\frac{\sigma_v}{\bar{v}}\right)^2 + \\ &\left(\frac{\bar{v}}{2\pi f_{\mu s}}\right)^2 \left(\frac{\arctan\left[\frac{2\zeta_{\mu s}\sqrt{1-\zeta_{\mu s}^2}}{2\zeta_{\mu s}^2-1}\right]-\pi}{\sqrt{1-\zeta_{\mu s}^2}}\right)^2 \left(\frac{\sigma_{fs}}{f_{\mu s}}\right)^2 + \\ &+\left(\frac{\bar{v}}{2\pi f_{\mu s}}\right)^2 \left(2\zeta_{\mu s}+4\zeta_{\mu s}^3+\frac{2\zeta_{\mu s}^3-4\zeta_{\mu s}^5}{\zeta_{\mu s}^2-1}+\frac{\pi\zeta_{\mu s}^2-\zeta_{\mu s}^2\arctan\left(\frac{2\zeta_{\mu s}\sqrt{1-\zeta_{\mu s}^2}}{2\zeta_{\mu s}^2-1}\right)}{\left(\sqrt{1-\zeta_{\mu s}^2}\right)^3}\right)^2 \left(\frac{\sigma_{\zeta s}}{\zeta_{\mu s}}\right)^2\end{aligned} \tag{123}$$

In this form, the expressions that multiply each of the variances relative to their means directly represent the sensitivities of those parameters.

7.3.3. Sensor related biases

Chapter 5 quantifies the variances in sensor position and GPS receiver tag latencies. Rewriting their expressions in the sensitivity form of Equation (123) yields

$$\sigma_{\varepsilon s}^2 = \left(\bar{\varepsilon}_s\right)^2 \left(\frac{\sigma_{\varepsilon s}}{\bar{\varepsilon}_s} \right)^2 \tag{124}$$

and

$$\sigma_{dlag}^{\ 2} = \left(\bar{v}\,\bar{\tau}_{lag}\right)^2 \left(\frac{\sigma_{\tau lag}}{\bar{\tau}_{lag}} \right)^2 + \left(\bar{v}\,\bar{\tau}_{lag}\right)^2 \left(\frac{\sigma_v}{\bar{v}} \right)^2 \tag{125}$$

respectively.

7.4. Full-Car Response Simulation

For the case studies of Chapter 5, the bumps extended uniformly across both wheels of an axle. Hence, each quarter-car response is the combined g-forces sensed from both of their wheel assemblies. The g-forces sensed from the rear quarter-car will be a time-delayed and attenuated version of the g-forces sensed from the front quarter-car. The time delay is equal to the ratio wheelbase/$\bar{v}$. The measured amplitude was about one-third of the magnitude sensed from the front-axle. Therefore, simulating tandem axle traversals requires two identically wide bumps where the second is one-third the height of the first and placed one wheelbase behind.

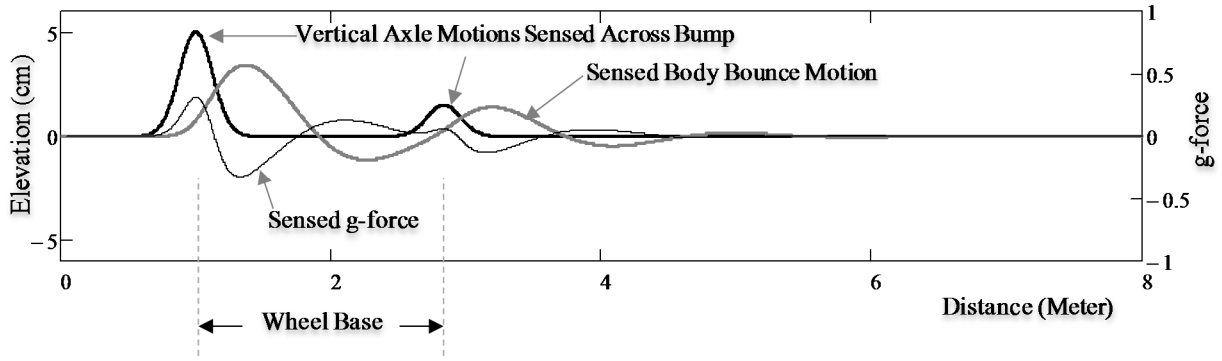

Figure 38. Simulated bump profile, vehicle body bounce response, and sensor signal

Tire deflection creates a contact path length of approximately 15 cm (6 in). The convolution of the patch length with the bump profile effectively widens the bump by twice the patch length. Figure 38 plots the body bounce and corresponding vertical acceleration from one

wheel path of a tandem quarter-car traveling over the simulated park bump at approximately 2.5 $m \cdot s^{-1}$ (5 mph).

Table 18. Spatial parameters of the tandem quarter-car simulation

Parameter	Units	Value
Axle separation (wheelbase)	m	2.834
First bump height	cm	5.0
Second bump height proportion	-	35%
Bump width	cm	30.0
Tire patch length	cm	15.0

Table 18 summarizes the spatial parameters of the simulation.

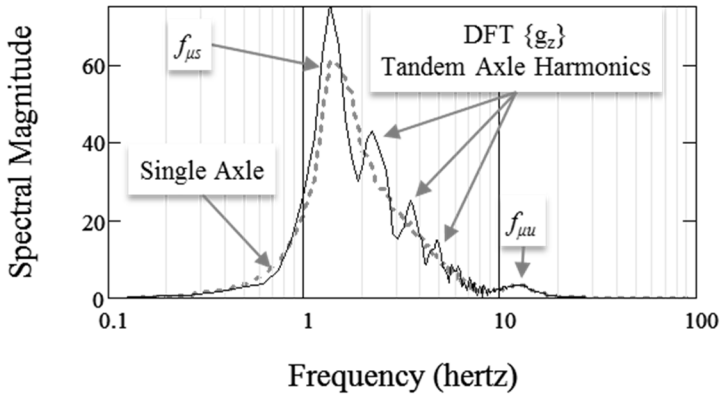

Figure 39. DFT of simulated accelerometer signals for single- and double-axle traversals

Figure 39 compares the frequency responses from the simulated single- and tandem-axle traversals. Adding the response from the rear axle crossing creates a semi-periodic pulse train that produces energy at the odd harmonics of $\overline{v}$ /wheelbase. The DFT of the simulated sensor output shown in Figure 39 indicates that the first three odd harmonics are located at approximately 2.1, 3.6, and 4.9 hertz as expected. This simulation result corresponds to the shape of the frequency response of the vehicle traversals shown for the case study revealed later in this chapter.

7.5. Precision Bounds of Position Estimate

From Equation (117), the position error $\tilde{\upsilon}_r$ (accuracy) is a random variable where

$$\tilde{\upsilon}_r = \hat{\upsilon}_r - \upsilon_p = (\Delta L + \varepsilon_r) + (\varepsilon_s + \varepsilon_{GPS}) + \varepsilon_d \tag{126}$$

Hence, the variance of the peak EAR-indices σ^2_{EAR} is the sum of the variances of the error components where

$$\sigma^2_{EAR} = \sigma^2_{\varepsilon r} + \sigma^2_{\varepsilon d} + \sigma^2_{\varepsilon s} + \sigma^2_{GPS} = \sigma^2_{\varepsilon r} + \sigma^2_{\varepsilon d} + \sigma^2_{\varepsilon s} + \left(\sigma^2_{dGPS} + \sigma^2_{dlag}\right) \tag{127}$$

This expression characterizes the error contribution from each factor that dilutes the precision of estimating the position of anomaly from the position of peak EAR-indices. The case study of the next section quantifies and compares the relative magnitudes of each factor.

7.6. Case Study of Anomaly Position Estimate

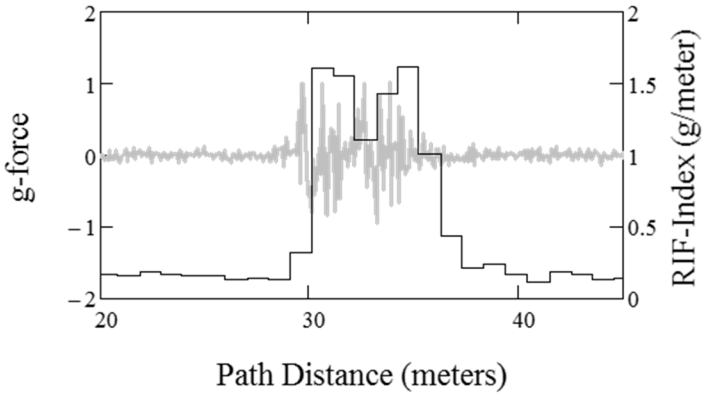

Figure 40. Accelerometer signal and windowed RIF-indices

Without prior information about the various parameter biases, the position of a peak EAR-index or TWIT index provides the best estimate for the position of an anomaly. Figure 40 shows the RIF-indices from a 1-meter resolution window transform. The corresponding inertial signal output exhibits the transient responses of the double axel crossing of the vehicle as well as

noise. The delay of the first peak RIF-index from the position of the first peak of the inertial signal is evident.

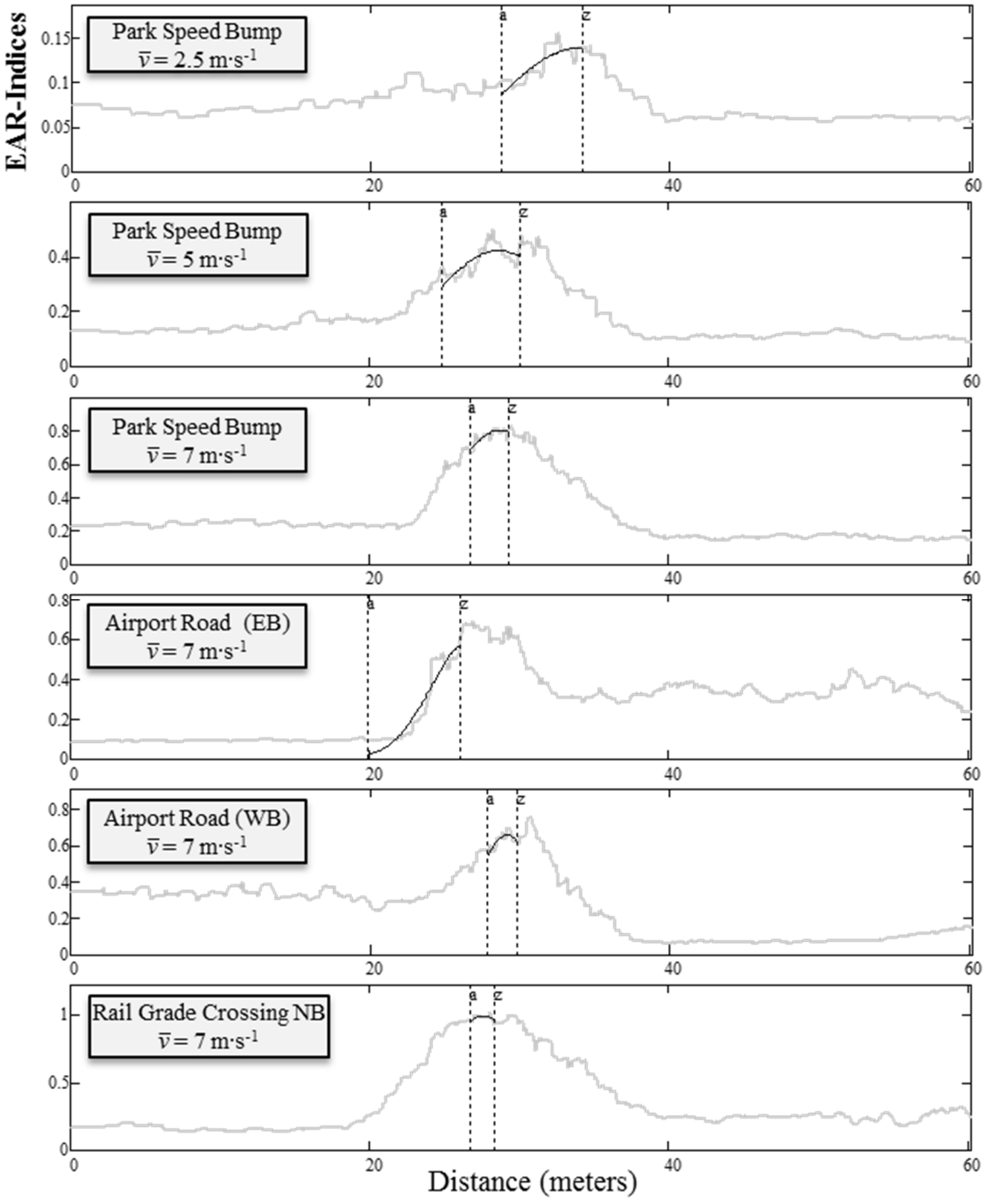

Figure 41. The EAR-indices for three bump types, speeds, and vehicles

Conceptually, the EAR-index is a single index summary of roughness for traversals within a specified speed band by combining the data from multiple onboard sensors, integrating the resultant vertical acceleration longitudinally, and then averaging the resulting RIF-indices from multiple traversals. The TWIT produces a speed-independent index of roughness by integrating the EAR indices for the range of speeds that users travel the segment.

As anticipated, the RIF-indices include energy from the bump, the transient response peaks, and noise from other vehicle response modes. If available, the application can remove known biases from the position of the peak EAR-index to improve the localization accuracy. The signal processing biases are available for known algorithms. It is also possible to estimate the nominal bias from vehicle suspension transient responses. Once standardized for all vehicles, statistics of the position of the embedded sensor would become available. However, the geospatial position error of *standard* GPS receivers will likely remain the dominant factor in position uncertainties.

7.6.1. Distributions of the ensemble average RIF

The charts of Figure 41 show the EAR-indices for 1-meter resolution RIF-transforms of the datasets for the six case studies conducted in Chapter 5. The distance indicated on the horizontal axis of each graph is relative to the geospatial coordinates of the reference position on the traversal path. The anomaly produces a peak EAR-index after each axle crossing. The second peak, when discernible such as in the 5 $m \cdot s^{-1}$ park bump case, occurs after the rear axle crosses the anomaly. The charts also overlay a Gaussian distribution fit to the EAR-indices between the *a* and *z* vertical markers that border the approximate position of the first peak. The least-squares method used to fit the function to the data is the Levenberg-Marquardt algorithm (Marquardt 1963).

The leading edge of the EAR-indices before the peak value provides the best approximation of the distribution because the transient responses included in the trailing edge tends to overestimate the spread of the peak position. The average offset of the position of the peak EAR-index across all case studies, including all biases, was -2.0 meters. The average of the spreads σ_{EAR} was 3.4 meters. The chi-squared (χ^2) significance for a Gaussian distribution fit of the EAR-indices near the peak was significantly greater than 5% for all cases.

Table 19. Parameters derived from the data of the six case studies

	Park Bump			Airport Road Bump		Tracks
Parameters	**2.5 m·s^{-1}**	**5 m·s^{-1}**	**7 m·s^{-1}**	**EB**	**WB**	**NB**
Sprung Mass Res., $f_{\mu s}$ (hertz)	1.371	1.933	2.588	2.154	2.159	1.896
Damping Estimate, $\zeta_{\mu s}$	0.20	0.13	0.26	0.09	0.09	0.18
Transient dist., $\overline{\varepsilon}_d$ (m)	0.977	1.410	1.681	1.669	1.651	2.006
Transient dist., $\sigma_{\varepsilon d}$ (m)	0.078	0.161	0.100	0.106	0.062	0.125
GPS tag lag, $\overline{\varepsilon}_{lag}$ (m)	-2.091	-4.999	-3.864	-5.309	-2.409	-7.784
GPS tag spread, σ_{dlag} (m)	0.460	1.011	1.212	1.162	1.109	1.230
GPS position, σ_{dGPS} (m)	4.992	4.242	3.122	2.367	1.676	1.936
EAR peak offset, $\tilde{\upsilon}_r$ (m)	2.450	-1.950	-0.750	-5.390	-1.290	-5.200
EAR spread, σ_{EAR} (m)	5.184	4.412	3.571	2.649	2.016	2.795
χ^2 Gaussian fit to σ_{EAR}	100.0%	100.0%	96.7%	100.0%	100.0%	54.9%
Residual spread, $\sigma_{\varepsilon R}$ (m)	1.315	0.645	1.236	0.235	0.144	1.591
Ratio $\sigma_{\upsilon}^2 / \sigma_{EAR}^2$	93.5%	97.7%	88.0%	99.1%	99.4%	67.4%
Ratio $\sigma_{pGPS}^2 / \sigma_{EAR}^2$	92.7%	92.4%	76.4%	79.8%	69.1%	48.0%
Ratio $\sigma_{lag}^2 / \sigma_{EAR}^2$	0.8%	5.3%	11.5%	19.2%	30.3%	19.4%
Ratio $\sigma_{\varepsilon d}^2 / \sigma_{EAR}^2$	0.0%	0.1%	0.1%	0.2%	0.1%	0.2%
Ratio $\sigma_{\varepsilon R}^2 / \sigma_{EAR}^2$	6.4%	2.1%	12.0%	0.8%	0.5%	32.4%

Table 19 summarizes the analysis results and includes the offset $\tilde{\upsilon}_r$ of the peak EAR-index from the position of the true peak and the estimated spread σ_{EAR}. The average χ^2

significance across all cases was 91.9%. Therefore, the analysis cannot reject the hypothesis that the distribution of EAR-indices about the peak value follows a Gaussian distribution.

7.6.2. Transient response estimate

The harmonics from the tandem axle crossings observed in the simulation results of Figure 39 are evident in the DFT of the actual signal. Hence, the data from real vehicle traversals match the simulated results and provide confidence that the tandem quarter-car model combined with the sensor transfer function adequately characterizes the system. The first seven rows of Table 19 list the vehicle and sensor parameters estimated previously in Chapter 5. The first two rows of the table summarize the estimated sprung-mass suspension parameters for each test vehicle.

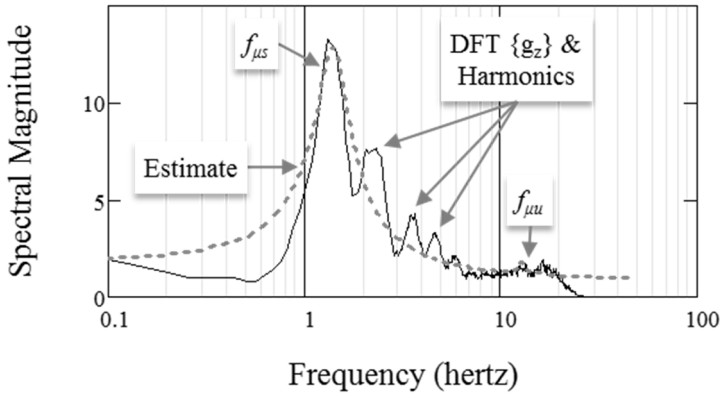

Figure 42. DFT of sensor output and quarter-car response estimate

Figure 42 shows the least squares fit of the combined quarter-car suspension and sensor transfer functions to the DFT of the inertial sensor signal from the 2.5 $m \cdot s^{-1}$ speed bump traversal case. The same vehicle produced the data for all traversals of a dataset. The resonant frequencies and damping ratios of a regular vehicle will likely vary during traversals. However, those variances are unknown. Hence, setting the theoretical variances to zero and lumping the residual variances into a single parameter will capture those nonlinearities. Substituting the

estimated suspension parameters into Equations (121) and (123) provides an estimate for the average transient response distance bias $\bar{\varepsilon}_d$ and the associated standard deviation $\sigma_{\varepsilon d}$. The average values across all case studies were 1.6 and 0.1 meters, respectively.

7.6.3. Relative uncertainties of bias factors

Chapter 5 derived the variance of the position of the first peak σ_v^2 in the inertial response. It represents the best achievable precision of the position estimate for the anomaly because of the *a priori* knowledge about its actual position. The average ratio $\sigma_v^2/\sigma_{EAR}^2$ of the first peak position variance to the variance of the EAR-index is within 5% for these case studies. This result indicates that the distribution of the EAR about the peak value approaches the performance of the best position estimator for anomalies. This is a very promising result because the EAR-index includes energy from all modal responses, transient responses, and noise.

Isolating the variances estimated for the transient response delay, the tag latency, and the GPS related errors derived in Chapter 5 from the variance of the EAR-indices about the peak value σ_{EAR}^2 yields the residual variance $\sigma_{\varepsilon R}^2$ such that

$$\sigma_{\varepsilon R}^2 = \sigma_{EAR}^2 - \left(\sigma_{\varepsilon r}^2 + \sigma_{\varepsilon s}^2 + \sigma_{\varepsilon d}^2 + \sigma_{dGPS}^2 + \sigma_{dlag}^2\right) \tag{128}$$

The residual variance captures differences between the true behavior of the system and the error model. Hence, the residual error could include non-linear effects from variations in the resonant frequencies and damping ratios of a vehicle's suspension system.

The last four rows of Table 19 summarize the relative error magnitudes from GPS trilateration, GPS position tagging latencies, vehicle transient responses, and the residual error. The error from GPS trilateration was the largest contributor with an average of 76% across all case studies. The position variance from GPS tag latency contributed the next largest error with

an average of 14.4% across all case studies. The position variance from transient responses was by far the least contributor, with an average of 0.1% across all cases. The average residual error across all cases was 9.0%. The largest residual is for the case with the poorest Gaussian fit to the spread of EAR-indices about the peak value. Nevertheless, the relatively large χ^2 significance for the Gaussian distribution provides a high level of confidence that the residual errors will diminish with higher traversal volumes.

Although relatively small for these case studies, the variance in suspension parameters for a single vehicle could increase from any non-linear behavior. In fact, the GPS related errors still dominate even if all the residual errors are attributable to suspension variances. Transient response related variances would increase with a larger spread in vehicle types that use the facility. However, the magnitude of that increase will likely remain insignificant because the suspension systems of nearly all vehicles respond similarly to comply with international standards that minimize vibration hazards to humans. In conclusion, the position uncertainty from *standard* GPS receivers will likely continue to dominate the achievable precision of estimating the actual position of pavement anomalies. Therefore, using higher accuracy systems such as differential GPS will improve the precision significantly.

7.6.4. Precision bounds

The $MOE_{1-\alpha}$ of the position estimate for the peak EAR-index is denoted $\Delta\varepsilon_{1-\alpha}$ where

$$\Delta\varepsilon_{1-\alpha} = \pm\frac{\sigma_{EAR}\cdot q_{1-\alpha/2}}{\sqrt{N_{\bar{v}[w]}^{P_j}}} \tag{129}$$

The standard normal quantile is $q_{1-\alpha/2}$ for a confidence interval of (1-α)%. The number of vehicle traversals is $N_{\bar{v}[w]}^{P_j}$ as defined in Equation (31). Hence, the 95% confidence interval is

$2 \times \Delta\varepsilon_{0.95}$ and $q_{1-\alpha/2} = 1.96$. The MOE_{95} diminishes with increasing traversal volume in the manner described by Equation (129).

Table 20. Vehicle parameters to compare precision bounds

Parameter	Single Vehicle	Typical Mix	Worst Case
GPS geospatial position spread, σ_{dGPS} (m)	3.056	3.056	10
GPS mean update period, $T_{\mu GPS}$ (s)	1.0	1.0	1.0
Sensor position standard deviation, $\sigma_{\varepsilon S}$ (m)	0	0.5	0.5
Vehicle batch mean speed, $\overline{\overline{v}}$ ($m \cdot s^{-1}$)	7	7	35
Batch speed standard deviation, $\sigma_{\bar{v}}$ ($m \cdot s^{-1}$)	1.0	1.0	1.0
Body bounce mean, $f_{\mu s}$ (hertz)	1.2	1.2	1.2
Body bounce standard deviation, σ_{fs} (hertz)	0	0.1	0.1
Damping ratio mean, $\zeta_{\mu s}$	0.35	0.35	0.35
Damping ratio standard deviation, $\sigma_{\zeta s}$	0	0.02	0.02

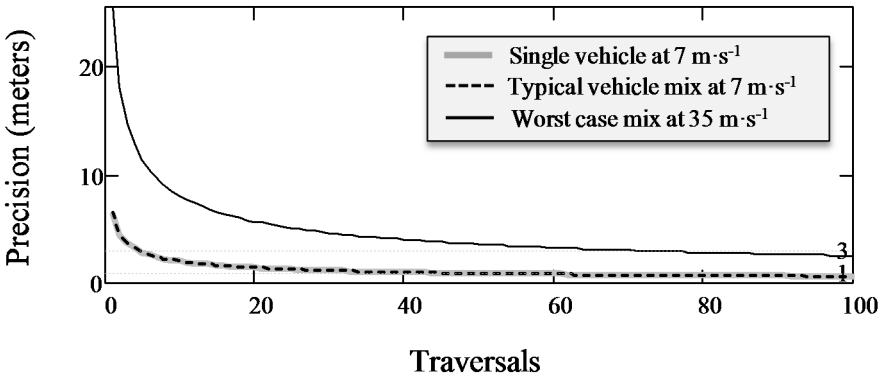

Figure 43. Precision bounds of peak position estimation

Figure 43 compares the MOE for three cases. Table 20 summarizes the parameters. Table 16 in Chapter 6 provides the mean values and standard deviations of the typical vehicle suspension parameters used. In theory, the sensor position and suspension variances for a single vehicle scenario are zero, hence Equation (128) becomes

$$\sigma_{EAR}^2 = \sigma_{\varepsilon R}^2 + \left(\sigma_{dGPS}^2 + \sigma_{dlag}^2\right). \tag{130}$$

The typical mix scenario incorporates the same error spreads as the single vehicle scenario except for the typical variances expected for the sensor position and the suspension parameters. The worst-case scenario incorporates the same sensor and suspension parameter statistics as the typical mix scenario but simulates the precision at a maximum speed of 35 $m \cdot s^{-1}$ and a worst-case geospatial position standard deviation of 10 meters. The GPS update rate for all scenarios is set to one second.

Figure 43 shows that the achievable precision for the single and the typical vehicle mix scenarios are indistinguishable. This is an expected result because the expected GPS related errors are identical and they dominate. For these scenarios, about 5 and 30 traversals will provide an estimate of the anomaly's position within 3 meters and 1 meter, respectively. The precision improves rapidly as the traversal volume grows toward five vehicles. Traversal volumes beyond 20 vehicles provide diminishing returns.

Both the speed and traversal volume are likely to increase for highways. The worst-case scenario uses the highest anticipated GPS position variance and vehicles traveling at a maximum speed of 35 $m \cdot s^{-1}$. Higher speeds stretch the uncertainties in the position estimate and, therefore, require a greater number of traversals to achieve the same precision as lower speed traversals. For instance, 70 traversals will localize anomalies within 3 meters for the worst-case scenario; on the other hand, the typical case and a five-fold speed reduction require only five traversals to achieve the same precision.

7.6.5. Error sensitivity of factors

Equation (123) directly indicates the sensitivity factors of each parameter deviation with respect to their mean value.

Table 21. Typical position error sensitivity and parameter spreads

	Typical Vehicle Mix Scenario		
Parameter	**Sensitivity (m)**	**CI_{95}**	**Uncertainty (m)**
Sensor position	1.00	97.99%	0.98
Transient peak			
Velocity factor	3.82	19.60%	0.75
QC resonance	3.82	16.33%	0.62
QC damping ratio	1.27	9.52%	0.12
GPS tag			
Latency variance	10.5	21.78%	**2.29**
Velocity variance	10.5	19.60%	2.06

Table 21 summarizes the distance sensitivity for parameters of the typical scenario. It lists the MOE_{95} as a percentage of the mean value and the associated uncertainty. The 95% confidence interval (CI_{95}) listed is a percentage of the mean value. The uncertainty shown normalizes the comparison of each error factor by taking the product of the sensitivity and the confidence interval. As indicated in bold font, the position uncertainty is most sensitive to variations in GPS related parameters. In fact, the uncertainty interval from GPS receiver related errors are more than three times greater than that from variations in vehicle suspension parameters. Finally, large variations in sensor position relative to the first axle can significantly dilute the precision of anomaly localization. Hence, this study recommends that vehicle manufacturers strongly consider standardizing the distance relative to the front-axle for inertial sensor installation.

7.7. Summary

The emergence of connected vehicles and smartphones offer lucrative opportunities to use them as dynamically distributed sensors to reduce the cost of network-wide monitoring by locating automatically and continuously anomalies that could pose risks to drivers. Methods that identify anomalies in the data streams of individual vehicle traversals lack the potential of statistical methods to improve precision of localization by combining the data streams from

many vehicles. The RIF-transform offers an adjustable spatial resolution window to localize inertial events along the traversal path. The EAR-index is an ensemble average of the RIF-indices at the position tags of each spatial window. Variations in the position tags from GPS receiver errors, sensor placement, and embedded system latencies create uncertainties in anomaly localization.

Six case studies to characterize the statistics of the spatially distributed EAR-indices could not reject the hypothesis that they follow a Gaussian distribution about the position of the anomaly. For normally distributed errors, the peak EAR indices inherently provide the best estimate for the position of anomalies. The spread of EAR-indices directly indicate the confidence interval of their localization. Furthermore, increases in traversal volume will reduce the MOE and increase the precision of localization. The case studies additionally demonstrated the benefit of using the spread of EAR-indices about the peak as a measure of uncertainty in the position estimate. Its performance approached that of an estimator that uses *a priori* knowledge about the position of an anomaly.

GPS related uncertainties dominated the overall position tagging error for the case studies. The uncertainties from suspension variability and vehicle transient responses were substantially smaller. It was possible to remove the bias errors from suspension transient responses by estimating the vehicle suspension parameters from discrete Fourier transform of the inertial data. A least squares fit of the quarter-car model provided estimates for the two primary mode frequencies and their associated damping ratios. However, the position errors from variances in vehicle suspension parameters were relatively small for these case studies because the same vehicle provided data for all traversals of a dataset. Nevertheless, a sensitivity analysis that included typical variations expected for the suspension parameters revealed that GPS

receiver related errors would still be more than three times those attributable to variations in vehicle transient responses.

This chapter characterized the precision bounds of estimating the position of anomalies from the distribution of EAR-indices. In general, the precision of estimating the position of anomalies increases rapidly as traversal volume grows beyond 20 vehicles. The model for MOE indicated that for the typical vehicle mix, 5 and 30 traversals would provide an estimate of the anomaly's position within 3 meters and 1 meter, respectively. For the worst case scenario of GPS related errors and a speed of 35 $m \cdot s^{-1}$, approximately 70 traversals would provide a precision of anomaly localization within 3 meters. Finally, the sensitivity analysis revealed that position estimates would be most sensitive to variations in the position of the sensor relative to the first axle. Therefore, this study recommends a connected vehicle standard to implement the inertial sensor at one or relatively few fixed distances from the front-axle of a vehicle.

CHAPTER 8. CONCLUSIONS AND RECOMMENDATIONS

Roadways are critical to the economic prosperity of all nations. Hence, their continuous deterioration in response to traffic loads and environmental factors poses significant challenges. Agencies must assess roadway performance regularly to enable effective pavement preservation programs. However, the scaling of existing methods for more frequent and network-wide characterizations of ride quality is cost prohibitive. A method of using onboard sensor data from connected vehicles offers the potential for both cost reduction and the continuous monitoring of all roadways. With limited access to standardized connected vehicles at present, researchers have been retrofitting regular vehicles with smartphones to log and transmit time, inertial, and geospatial position data. Methods presently available to produce roughness indices from onboard sensor data do not scale for practical deployment because they require calibration with individual vehicle responses. This research produced a scalable approach to transform voluminous sensor data from connected vehicles into a reliable single-index summary of road roughness. Agencies will benefit by integrating the computationally simple models into decision-support platforms. The solution will enable deterioration forecasting that is more reliable. The methods and models provide an ability to localize anomalies that could pose hazards to the traveling public.

The research goals were to develop the models, characterize their performance relative to the prevailing methods, and to demonstrate their performance and utility through case studies. The objectives achieved in pursuing the goals were as follows:

1. development of a computationally simple and effective model to transform time, inertial, and geospatial position data streams to a single index summary of roughness, namely the road impact factor (RIF) index

2. establishment of a direct proportionality relationship between the RIF-index and the prevailing standard, namely the international roughness index (IRI)
3. preservation of the IRI utility while eliminating its deficiencies by defining a speed independent model, namely the time-wavelength-intensity-transform (TWIT)
4. quantification of the trade-off in accuracy and precision of ride quality characterizations relative to the practical variances in traversal volume, vehicle suspension parameters, and sensor characteristics
5. quantification of the model performance that would use RIF-indices as independent variables to forecast pavement deterioration
6. characterization of the accuracy and precision of the new models in anomaly localization

The case studies demonstrated the practical use of the new models and methods.

8.1. Summary of Models and Methods

The continuous differentiability and practically finite extent of the modified Gaussian radial basis function provided the theoretical framework for roughness simulation and characterization. The translation, dilation, and amplification features provided an ability to study the manifestations of roughness energy in both the time and frequency domains. The insights gained led to the definitions of the RIF-transform and the TWIT. Initiating the notion of vertical acceleration potential and kinetic energies provided the distinction to characterize profile roughness in the spatial and temporal domains, respectively. These notions explained the transformation of spatial elevation profiles to vertical accelerations that vehicle occupants experience when traveling in various vehicles at different speeds. Representing vehicle suspension systems as mechanical filters with dual resonance modes uncovers the non-linear sensitivity to profile roughness at different speeds. These characterizations lead to mathematical

explanations of the various IRI limitations that practitioners detected. The square-law of differentiation illustrated how bumps of different heights and widths could produce identical roughness intensities. Similarly, the square-law also demonstrated how traversing the same bump at different speeds could produce differences in roughness magnitude that the IRI masks but riders actually experience. These theoretical characterizations explain the gap in previous attempts to transform inertial signals to a single-index summary of roughness.

The RIF-transform is a compression of the inertial signal per unit of distance traveled. Its derivation stems from the physical principle that the accelerometer signal energy is a complete representation of the vibration energy experienced. Parseval's Theorem produces an equivalent quantification of the signal energy in the temporal and spectral domains. The theorem points to a simple time-domain computation of the RIF-transform. Subsequently, the RIF-index is a summary of the average g-force experienced after traveling a segment of road. The RIF-index is a more intuitive summary of roughness than the IRI because it is a *measure* of the average g-forces that a rider experienced rather than a *simulation* of the accumulated suspension motion from a pre-defined quarter-car model. The RIF-transform requires significantly lower computational resources than the IRI or the PSD transforms. The simplicity of its scalar multiply-and-accumulate (MAC) operations allows almost any sensor to compute the RIF-transform directly, using negligible amounts of energy.

The ensemble average of the RIF-indices (EAR) for any desired spatial resolution window, within a specified speed band, represents a vertical compression of the roughness indices from multiple vehicle traversals. The case studies validated that the distribution of the RIF-indices from multiple traversals result in an excellent fit with classic distributions such as the Gaussian and t-distributions. Therefore, the margin-of-error (MOE) will expectedly diminish

with higher vehicle traversal volumes. The TWIT is a weighted average, by traversal volume, of the RIF-indices from all speed bands reported for a segment. Hence, the TWIT-index reflects the average g-force that riders experienced at the typical range of speeds that they traveled the segment.

The onboard inertial sensor produces six parameters: one set of tri-axial accelerometer values, and one set of tri-axial orientation values. The onboard GPS receiver produces a pair of geospatial coordinates and a ground speed. An integrated clock produces a timestamp for the sensor samples at regular intervals. Hence, the integrated sensor unit produces a data file containing 10 parameters per row. The application updates each row at the selected sample interval setting for the inertial sensor. At the recommended settings for the update rates, one gigabyte of sensor memory stores about 109 hours of pre-processed data.

The data integration algorithm combines the inertial sensor parameters to produce a resultant vertical acceleration that is sensor orientation independent. The RIF-transform then combines the resultant vertical acceleration, the velocity, the timestamp, and the geospatial coordinates into a single roughness index for each spatial resolution window. Producing the RIF-index for spatial resolution windows of about one kilometer will provide an IRI equivalent summary of roughness.

The variations of sensor and vehicle suspension parameters and the volume of traversals available establish practical bounds for the precision of the RIF-index. Therefore, establishing the best settings for all onboard sensors will enhance consistency. Aftermarket sensor installation, such as smartphones, produce the best results when secured anywhere on the dashboard of the vehicle. This placement provides good mechanical coupling to sense the vehicle vibrations. The dashboard surface is also a good location for satellite signal reception.

The frequency response of nearly all vehicles points to a minimum sample rate for the inertial sensor of 64 hertz. The case studies validate this result by demonstrating diminishing returns beyond that sample rate. The minimum GPS update rate setting should be such that the variance in position tags for the inertial samples would be no greater than the expected error from GPS trilateration. The position tagging error arises from two factors. They are the embedded system latency in retrieving the updated GPS coordinates and the latency in tagging the inertial samples with equivalent path distances. The case study incorporated a signal processing method to isolate the trilateration distance errors from those of the tagging delays by tracking the distribution of the first inertial response peak from traversing an anomaly at a reference position. The results from six case studies indicated that the trilateration errors were within the spread of 3 meters that GPS operators expect. The spread in differential distance updates for devices set at two different rates indicated that the variance in distance lag is a direct function of the GPS update rate selection. Traversal velocity variations amplify the errors in position tagging. The analysis indicated that for the case studies, the minimum GPS update rate recommended for detecting anomalies would be 1 hertz, and twice that rate for highway speeds.

The accuracy and precision of deterioration forecasts improves continuously with traversal volume when employing empirical models with RIF-indices as the explanatory variable. The rate of precision improvement with traversal volume depends on the overall spread in vehicle suspension parameters and the selected boundaries for each speed band. The case study used suspension system parameter spreads derived for typical vehicles to illustrate the achievable precision trade-off with data collection volume. For a scenario where 20% of the vehicles traveling a segment are connected, one week of sensor data collection will forecast RIF-index threshold with a worst-case precision of three and seven weeks for the typical urban and

rural interstates, respectively. Within the same confidence interval, the precision bounds improve or require fewer data collection days with additional vehicle participation.

The EAR provides a multi-resolution tool for observing roughness at both the network and local levels. The peak EAR values are inherently best estimators for both the roughness intensity and the position of anomalies. The EAR spread characterizes the MOE for the position estimate of an anomaly. Therefore, color-coding the EAR for GIS implementation will provide a viable method of data visualization to examine clusters and patterns of localized roughness at any spatial resolution. For the typical traffic mix and speeds, the precision of anomaly localization will improve rapidly as the available traversal volume grows beyond five and become asymptotic beyond 20. Six case studies demonstrated that GPS related errors tend to dominate the interval of uncertainty, whereas, variances in vehicle suspension parameter tend to be three-fold less significant.

8.2. Summary of Research Contributions

The methods and models developed in this research breaks through long-standing constraints to reduce the cost, expand the reach, and increase the frequency of ride quality characterizations. The techniques developed enable the first statistical approach to pavement performance evaluation using connected vehicles. The direct proportionality relationship with the IRI at fixed speeds will extend investments in IRI datasets through simple scaling. Therefore, agencies have the flexibility of continuing to use the IRI while expanding applications that utilize the RIF- and TWIT-indices. Unlike the IRI or the PSD, the computational simplicity of the RIF-transform and the TWIT provides flexibility for onboard devices to compute them directly for real-time observation. Their computational simplicity minimizes the cost of continuous scaling for widespread adoption.

The new models address the IRI utility gaps by extending their application to all facility types and all speeds. Inertial sensors directly measure the actual roughness energy that riders experience on either paved or unpaved roads. The IRI data collection and simulation procedure limits its application to paved highways and a fixed speed. Simulating a fixed quarter-car model at a fixed speed produces an IRI that is spatial wavelength biased. The TWIT precludes this bias by integrating roughness from all wavelengths and traversal speeds. Moreover, multiple traversals to characterize roughness produce a more statistically significant measure. Agencies typically produce the IRI based on elevation profile measurements taken from a single traversal, and often from only one lane, and in one direction. Sampling the inertial response of vehicles that actually use all the facilities provides a more complete characterization of their performance. Furthermore, the accuracy and precision of applications that forecast pavement deterioration and localize anomalies will improve continuously with higher data volume as more connected vehicles participate. In-depth analysis identified the best inertial sensor sample rate and GPS update rate settings for standardization. The case studies conducted validated those selections of sensor settings.

The new approach to ride quality characterization has a broad reach. The methods and models will enable cost-reduced, continuous situational awareness, and objective asset management for all roads worldwide. Nations that cannot afford laser-based probe vehicles to compute the IRI will have a substantially lower cost alternative by using smartphones to enable connected vehicles that are compatible with their existing communications infrastructure. Agencies that utilize the TWIT to visualize roughness will have enhanced data visualization capabilities and reduce their training requirements to interpret roadway performance data. By integrating these models into decision-support platforms, agencies throughout the world will be

able to realize enormous savings by making effective data-driven decisions to optimize their pavement preservation practices.

8.3. Limitations and Future Research

Methods that use probe vehicles to sample the condition of pavements do not necessarily characterize the roughness of sections outside the wheel path. Although differences in driving habits and lane changes will allow connected vehicles to provide a broader spatial assessment than the IRI would, drivers are not likely to traverse the road shoulders. Furthermore, drivers will tend to avoid anomalies such as potholes when their location has become familiar. Therefore, other methods must complement probe vehicles to characterize all aspects of pavement condition.

Anomalies such as utility covers, concrete pavement joints, and precipitation will produce roughness that does not necessarily require remediation. Therefore, future research will incorporate remote sensing techniques to complement probe vehicle methods of roughness characterization. Methods of remote sensing, such as hyperspectral, are capable of providing both high spatial and spectral resolutions to discern pavement cracks, estimate the age of asphalt pavements, identify metallic objects such as utility covers, and measure geometric features of the facility. Consequently, remote sensing methods will help to enhance the situational awareness of pavement condition in general while identifying anomalies that do not necessarily warrant attention. The invention of new techniques to mine the probe data for anomaly classification will enable the removal of select roughness features from the characterization of ride quality. Future work will examine the feasibility of these and other related ideas that emerge as the author further develops the method for technology transfer.

REFERENCES

AASHTO. 2009. *Rough Roads Ahead: Fix Them Now or Pay for It Later.* Washington, DC: American Association of State Highway and Transportation Officials (AASHTO) and The Road Information Program (TRIP).

AASHTO. 2010. *Standard Equipment Specification for Inertial Profiler.* Standard M328-10, Washington, DC: American Association of State and Highway Transportation Officials (AASHTO).

Agresti, Alan, and Barbara Finlay. 2008. *Statistical Methods for the Social Sciences.* 4th. Pearson.

Ahlin, Kjella, and N.O. Johan Granlund. 2002. "Relating Road Roughness and Vehicle Speeds to Human Whole Body Vibration and Exposure Limits." *International Journal of Pavement Engineering* (Taylor & Francis) 3 (4): 207-216. doi:10.1080/10298430210001701.

Al-Omari, Bashar, and Michael I Darter. 1994. "Relationships Between International Roughness Index and Present Serviceability Rating." *Transportation Research Record* (Transportation Research Board) (1435): 130-136.

Anastasopoulos, Panagiotis Ch., Fred L. Mannering, and John Haddock. 2009. *Effectiveness and Service Lives/Survival Curves of Various Pavement Rehabilitation Treatments.* Publication FHWA/IN/JTRP-2008/12. Joint Transportation Research Program, Indiana: Indiana Department of Transportation and Purdue University. doi:10.5703/1288284314292.

Andrén, Peter. 2006. "Power spectral density approximations of longitudinal road profiles." *International Journal of Vehicle Design* (Inderscience Publishers) 40 (1/2/3): 2-14. doi:10.1504/IJVD.2006.008450.

Android Open Source Project. 2014. "SensorManager." *Android Developers.* Google. 5 20. Accessed 5 26, 2014. http://developer.android.com/reference.

Angeles, Jorge. 2011. *Dynamic Response of Linear Mechanical Systems: Modeling, Analysis and Simulation.* New York: Springer.

Apple Inc. 2014. *Location and Maps Programming Guide.* Applications Programmer Guide, Cupertino, CA: Apple Inc., 88. https://developer.apple.com/library/ios/documentation/UserExperience/Conceptual/LocationAwarenessPG/LocationAwarenessPG.pdf.

Astarita, Vittorio, Maria Vittoria Caruso, Guido Danieli, Demetrio Carmine Festa, Vincenzo Pasquale Giofrè, Teresa Iuele, and Rosolino Vaiana. 2012. "A mobile application for road surface quality control: UNIquALroad." *15th meeting of the EURO Working Group on Transportation (EWGT 2012).* Paris, France: Elsevier Ltd. 1135-1144. doi:10.1016/j.sbspro.2012.09.828.

ASTM. 1997. *Standard Terminology Relating to Vehicle-Pavement Systems.* Standard E867. West Conshohocken, PA: American Society of Testing and Materials (ASTM).

Ayenu-Prah, A. Y., and N. O. Attoh-Okine. 2009. "Comparative study of Hilbert–Huang transform, Fourier transform and wavelet transform in pavement profile analysis." *International Journal of Vehicle Mechanics and Mobility* (Taylor & Francis) 47 (4): 437-456. doi:10.1080/00423110802167466.

Bastani, Parisa, John B. Heywood, and Chris Hope. 2012. *U.S. CAFE Standards -- Potential for Meeting Light-duty Vehicle Fuel Economy Targets, 2016-2025.* MIT Energy Initiative, Boston, Massachusetts: Massachusetts Institute of Technology.

Besinger, F. H., D. Cebon, and D. J. Cole. 1995. "Force Control of a Semi-Active Damper." *Vehicle System Dynamics: International Journal of Vehicle Mechanics and Mobility* (Taylor & Francis) 24 (9): 695-723.

Bogsjö, K. 2007. "Evaluation of stochastic models of parallel road tracks." *Probabilistic Engineering Mechanics* (Elsevier Ltd.) 22 (4): 362-370. doi:10.1016/j.probengmech.2007.08.002.

Bouret, Megan. 2013. "PAVVET Roughness Intensity Monitor." *NDSU Computer Science Capstone Projects.* Fargo, ND: Upper Great Plains Transportation Institute.

Boyadjis, Mark. 2013. *Emerging Technologies: Big Data in the Connected Car.* Market Insight, Douglas County, Colorado: IHS Inc.

Bridgelall, Raj. 2014. "A participatory sensing appproach to characterize ride quality." *Proceedings of SPIE Volume 9061 on Sensors and Smart Structures Technologies for Civil, Mechanical, and Aerospace Systems.* San Diego: SPIE. (in press).

—. 2014. "A participatory sensing approach to characterize ride quality." *Proceedings of SPIE Volume 9061, Sensors and Smart Structures Technologies for Civil, Mechanical, and Aerospace Systems.* San Diego: SPIE. doi:10.1117/12.2046854.

Bridgelall, Raj. 2014. "Connected Vehicle Approach for Pavement Roughness Evaluation." *Journal of Infrastructure Systems* (American Society of Civil Engineers) 20 (1): 04013001. doi:10.1061/(ASCE)IS.1943-555X.0000167.

Bridgelall, Raj. 2004. "Inertial Sensor Sample Rate Selection for Ride Quality Measures." *Journal of Infrastructure Systems* (American Society of Civil Engineering) 04014039. doi:10.1061/(ASCE)IS.1943-555X.0000225.

Bridgelall, Raj. 2014. "Inertial Sensor Sample Rate Selection for Ride Quality Measures." *Journal of Infrastructure Systems* (American Society of Civil Engineering) 04014039. doi:10.1061/(ASCE)IS.1943-555X.0000225.

Bridgelall, Raj. 2014. "Precision Bounds of Pavement Deterioration Forecasts from Connected Vehicles." *Journal of Infrastructure Systems* (American Society of Civil Engineers) 04014033: Online Version.

Bridgelall, Raj. 2014. "Precision Bounds of Pavement Distress Localization with Connected Vehicle Sensors." *Journal of Infrastructure Systems* (American Society of Civil Engineers) 04014045. doi:10.1061/(ASCE)IS.1943-555X.0000234.

Brookner, Eli. 1998. *Tracking and Kalman Filtering Made Easy.* John Wiley and Sons.

Brown, Doug, Wei Liu, and Theunis F. P. Henning. 2010. *Identifying Pavement Deterioration by Enhancing the Definition of Road Roughness.* Research Report 430, Wellington, New Zealand: NZ Transport Agency, 66.

Brown, H., U. Gerz, and P. Sulten. 1991. *Collecton and Evaluation of Road Unevenness.* Report 598, Building and Housing, Dusseldorf, Germany: Federal Minister for Transport, 223.

BTS. 2013. *Compiled from Commmodity Flow Survey Data and the Freight Analysis Framework (FAF) Models, 2004 - 2012.* Washington, D.C.: Bureau of Transportation Statistics (BTS), USDOT.

Buhmann, Martin Dietrich. 2008. *Radial Basis Functions: Theory and Implementations.* Massachusetts: Cambridge University Press.

CAR. 2013. *Pavement Condition Monitoring with Connected Vehicle Data.* Michigan Department of Transportation (MDOT) State Planning and Research, Detroit, Michigan: Center for Automotive Research (CAR), 35.

Carey, W. N. Jr., H. C. Huckins, and R. C. Leathers. 1962. "Slope Variance as a Measure of Roughness and the Chloe Profilometer." *Highway Research Board Conference on the AASHO Road Test.* Washington, D.C.: Highway Research Board. 126-137.

Carey, William N. Jr., and Paul E. Irick. 1960. *The Pavement Serviceability - Performance Concept.* Bulletin 250, National Research Council, Washington, D.C.: Highway Research Board, 40-58.

Chen, Chi-Tsong. 2004. *Signals and Systems.* 3rd. New York: Oxford University Press.

Chen, Kongyang, Mingming Lu, Xiaopeng Fan, Mingming Wei, and Jinwu Wu. 2011. "Road condition monitoring using on-board Three-axis Accelerometer and GPS Sensor." *6th International ICST Conference on Communications and Networking in China.* Harbin, China: Chinacom. 1032-1037. doi:10.1109/ChinaCom.2011.6158308.

Chen, Kongyang, Xiaolin Zhang, and Mingming Lu. 2011. *Data mining system for road pothole detection with on-board sensors.* Bulletin of advanced research, Shenzhen, China: Shenzhen Institutes of Advanced Technology.

Chen, Kongyang, Xiaolin Zhang, and Mingming Lu. 2011. "Data mining system for road pothole detection with on-board sensors." *Bulletin of Advanced Technology Research* (Shenzhen Institutes of Advanced Technology) 5 (12): 28-36.

Christin, Delphine, Andreas Reinhardt, Salil S. Kanhere, and Matthias Hollick. 2011. "A survey on privacy in mobile participatory sensing applications." *Journal of Systems and Software* (Elsevier Science Inc.) 84 (11): 1928-1946. doi:10.1016/j.jss.2011.06.073.

Cohan, Peter. 2013. "Four Reasons Google Bought Waze." *Forbes.com.* June 11. Accessed May 5, 2014. www.forbes.com.

Cristofaro, Emiliano De, and Claudio Soriente. 2013. "Participatory Privacy: Enabling Privacy in Participatory Sensing." *IEEE Network* (Institute of Electrical and Electronic Engineers (IEEE)) 27 (1): 32-36.

Davis, B. R., and A. G. Thompson. 2001. "Power Spectral Density of Road Profiles." *Vehicle System Dynamics* (Taylor & Francis Group) 35 (6): 409-415. doi:10.1076/vesd.35.6.409.2039.

Dawkins, Jeremy, David Bevly, Buzz Powell, and Richard Bishop. 2011. *Investigation of Pavement Maintenance Applications of Intellidrive.* Virginia: University of Virginia: DOT Pooled Fund Study.

Delanne, Yves, and Paulo A. A. Pereira. 2001. "Advantages and Limits of Different Road Roughness Profile Signal-Processing Procedures Applied in Europe." *Transportation Research Record: Journal of the Transportation Research Board* (Transportation Research Board of the National Academies) 1764 (26): 254-259. doi:10.3141/1764-26.

Dodds, C. J., and J. D. Robson. 1973. "The description of road surface roughness." *Journal of Sound and Vibration* (Elsevier Ltd.) 31 (2): 175-183. doi:10.1016/S0022-460X(73)80373-6.

Doré, Guy, Martin Flamand, and Pierre Pascale. 2002. "Analysis of the Wavelength Content of the Longitudinal Profiles for C-LTPP Test Sections." *Canadian Journal of Civil Engineering* 29 (1): 50-57. doi:10.1139/l01-075.

Douangphachanh, Viengnam, and Hiroyuki Oneyama. 2013. "A Study on the Use of Smartphones for Road Roughness Condition Estimation." *Journal of the Eastern Asia Society for Transportation Studies* (Eastern Asia Society for Transportation Studies) 10: 1551-1564. doi:10.11175/easts.10.1551.

Du, Yuchuan, Chenglong Liu, Difei Wu, and Shengchuan Jiang. 2014. "Measurement of International Roughness Index by Using Z-Axis Accelerometers and GPS." *Mathematical Problems in Engineering* (Hindawi Publishing Corporation) 10. doi:http://dx.doi.org/10.1155/2014/928980.

Dyer, Stephen A., Ryan Boyd, and Justin S. Dyer. 2005. *Refinement of Measurement Techniques of Road Profile and International Roughness Index (IRI) to Support the KDOT Pavement Management System (PMS) Annual Road-Condition Survey Research.* Research Report K-

TRAN: KSU-99-7, Manhattan, Kansas: Kansas State University (Department of Civil Engineering) for the Kansas Department of Transportation (KDOT), 149.

Eriksson, Jakob, Lewis Girod, Bret Hull, Ryan Newton, Samuel Madden, and Hari Balakrishnan. 2008. "The pothole patrol: using a mobile sensor network for road surface monitoring." *Proceedings of the 6th international conference on Mobile systems, applications, and services.* New York: Association for Computing Machinery (ACM). 29-39. doi:10.1145/1378600.1378605.

FHWA. 2011. *2010 Status of the Nation's Highways, Bridges, and Transit: Conditions & Performance.* Report to Congress, Federal Highway Administration and Federal Transit Administration (FHWA), Washington, DC: U.S. Department of Transportation.

FHWA. 2010. *Beyond the Short Term: Transportation Asset Management for Long-Term Sustainability, Accountability and Performance.* Washington, D.C.: Federal Highway Administration.

FHWA. 2013. *Highway Statistics.* Washington, D.C.: Federal Highway Administration (FHWA).

Fitzpatrick, Kay, and William H. Schneider IV. 2005. *Turn Speeds and Crashes Within Right-Turn Lanes.* FHWA/TX-05/0-4365-4, Austin, Texas: Texas Department of Transportation, 87.

Gade, Kenneth. 2010. "A Non-singular Horizontal Position Representation." *The Journal of Navigation* (The Royal Institute of Navigation) 63 (3): 365-417.

Galehouse, Larry, James S. Moulthrop, and R. Gary Hicks. 2003. "Principles of Pavement Preservation: Definitions, Benefits, Issues, and Barriers." *TR News* (Transportation Research Board (TRB)) 4-15.

Garcia-Pozuelo, Daniel, Antonio Gauchia, Ester Olmeda, and Vicente Diaz. 2014. "Bump Modeling and Vehicle Vertical Dynamics Prediction." *Advances in Mechanical Engineering* (Hindawi Publishing Corporation) 2014: 1-10. doi:10.1155/2014/736576.

General Motors. 1987. *Suspension Rates and Frequency.* Suspension Design Guidelines 1070, General Motors.

Gillespie, T. D., M. W. Sayers, and C. A. V. Queiroz. 1986. *The International Road Roughness Experiment: Establishing Correlation and Calibration Standard for Measurement.* Technical Report No. 45, Washington, D.C.: The World Bank, 464.

Gillespie, Thomas D. 2004. *CarSim Data Manual.* Ann Arbor, Michigan: Mechanical Simulation Corporation.

—. 1992. "Everything You Always Wanted to Know about the IRI, But Were Afraid to Ask!" *Road Profile Users Group Meeting.* Lincoln, Nebraska: The University of Michigan Transportation Research Institute.

Gillespie, Thomas D. 1981. *Technical Considerations in the Worldwide Standardization of Road Roughness Measurement.* World Bank Technical Report UM-HSRI-81-28, Ann Arbor, Michigan: University of Michigan Transportation Research Institute.

Gónzalez, L. C., F. Martínez, and M. R. Carlos. 2014. "Identifying Roadway Surface Disruptions Based on Accelerometer Patterns." *IEEE Latin America Transactions* (Institute of Electrical and Electronic Engineers) 12 (3): 455-461.

Griffin, M. J. 1990. *Handbook of Human Vibration.* New York: Elsevier.

Haider, Sayed Waqar, Gilbert Y. Baladi, Karim Chatti, and Christopher M. Dean. 2010. "Effect of Pavement Condition Data Collection Frequency on Performance Prediction." *Transportation Research Record: Journal of the Transportation Research Board* (Transportation Research Board) (2153): 67-80.

Haider, Syed Waqar, and Monther B. Dwaikat. 2011. "Estimating Optimum Timing for Preventive Maintenance Treatment to Mitigate Pavement Roughness." *Transportation Research Record: Journal of the Transportation Research Board* (Transportation Research Board of the National Academies) 2235: 43-53. doi:10.3141/2235-06.

Haider, Syed Waqar, Karim Chatti, Gilbert Y. Baladi, and Nadarajah Sivaneswaran. 2011. "Impact of Pavement Monitoring Frequency on Pavement Management System Decisions." *Transportation Research Record: Journal of the Transportation Research Board* (Transportation Research Board of the National Academies) 2225: 43-55. doi:10.3141/2225-06.

Hausman, Joseph, and Justin Clarke. 2012. *FHWA Functional Classification Guidance Update.* Report, Federal Highway Administration, Washington, DC: U.S. Department of Transportation.

Hautakangas, Hannu, and Jukka Nieminen. 2011. *Data mining for pothole detection.* Pro Gradu Seminar, Finland: University of Jyväskylä.

Hesami, Reyhaneh, and Kerry J. McManus. 2009. "Signal Processing Approach to Road Roughness Analysis and Measurement." *TENCON 2009 -- IEEE Region 10 Conference.* Swinburn University of Technology. 1-6.

HPMS. 2012. *Highway Performance Monitoring System (HPMS) Field Manual for the Continuing Analytical and Statistical Database.* Field Manual, Office of Highway Policy Information Federal Highway Administration, Washington, DC: Federal Highway Administration.

Hudson, W. Ronald, Dan Halbach, John P. Zaniewski, and Len Moser. 1983. "Root-Mean-Square Vertical Acceleration as a Summary Roughness Statistic." Edited by Thomas D. Gillespie and Michael Sayers. *Measuring Road Roughness and Its Effects on User Cost and Comfort: A Symposium Sponsored by ASTM Committee E-17 on Traveled Surface Characteristics.* Bal Harbour, Florida: American Society for Testing and Materials (ASTM). 3-24.

Hveem, F. N. 1960. "Devices for Recording and Evaluating Pavement Roughness." *Highway Research Board Bulletin 264* 1-26. http://www.dot.ca.gov/newtech/researchreports/1959-1960/60-09.pdf.

Industry Experts Group. 2013. *Global Automotive Sensors Market with Special Focus on MEMS Sensors.* Market Report, London, U.K.: Industry Experts Group, 448.

ISO 8608. 1995. *Mechanical Vibration -- Road Surface Profiles -- Reporting of Measured Data.* International Standard, Geneva, Switzerland: International Organization for Standardization (ISO).

Janoff, Michael S. 1990. "The Prediction of Pavement Ride Quality from Profile Measurements of Pavement Roughness." In *Surface Characteristics of Roadways: International Research and Technologies*, edited by W. E. Meyer and J. Reichert, 259-276. Philadelphia: American Society of Testing and Materials (ASTM).

Johannesson, Pär, Krzysztof Podgórski, and Igor Rychlik. 2014. *Modelling roughness of road profiles on parallel tracks using roughness indicators.* Preprint 2014:4, Department of Mathematical Sciences, Gothenburg, Sweden: Chalmers University of Technology and University of Gothenburg, 32.

Jordan, P. G., and D. R. C. Cooper. 1989. *Road Profile Deterioration as an Indicator of Structural Condition.* Research Report, Pavement Design and Maintenance Division, Highways Group, Washington, DC: Transport and Road Research Laboratory, 9.

Karamihas, Steven M., and Kevin Senn. 2012. *Curl and Warp Analysis of The LTPP SPS-2 Site in Arizona.* FHWA-HRT-12-068, Washington, D.C.: Federal Highway Administration (FHWA), 114. http://www.fhwa.dot.gov/publications/research/infrastructure/pavements/ltpp/12068/12068.pdf.

Katicha, Samer W., John El Khoury, and Gerardo W. Flintsch. 2015. "Assessing the Effectiveness of Probe Vehicle Acceleration Measurements in Estimating Road Roughness." *International Journal of Pavement Engineering* (Taylor & Francis) Online. doi:10.1080/10298436.2015.1014815.

Khosla, N. P. 1985. *Investigation of Premature Distresses in Flexible Pavements.* FHWA/NC/85-001, Washington, D.C.: Federal Highway Administration, 436.

Kropáč, O., and P. Múčka. 2009. "Effects of longitudinal road waviness on vehicle vibration response." *Vehicle System Dynamics: International Journal of Vehicle Mechanics and Mobility* (Taylor & Francis) 47 (2): 135-153.

Kropáč, Oldřich, and Peter Múčka. 2005. "Be careful when using the International Roughness Index as an indicator of road unevenness." *Journal of Sound and Vibration* (Elsevier Ltd.) 287 (4-5): 989-1003. doi:10.1016/j.jsv.2005.02.015.

Ksaibati, Khaled, Ronald McNamara, William Miley, and Jamshid Armaghani. 1999. "Pavement Roughness Data Collection and Utilization." *Transportation Research Record: Journal of the*

Transportation Research Board (Transportation Research Board of the National Academies) 1655: 86-92. doi:10.3141/1655-12.

Ku, Harry H. 1966. "Notes on the Use of Propagation of Error Formulas." *Journal of Research of the National Bureau of Standards, Section C: Engineering and Instrumentation* (National Bureau of Standards) 70C (4): 263-273. http://www.itl.nist.gov/div898/handbook/mpc/section5/mpc552.htm; http://nvlpubs.nist.gov/nistpubs/jres/70C/jresv70Cn4p263_A1b.pdf.

Lak, Mohammad Amin, Geert Degrande, and Geert Lombaert. 2011. "The influence of the pavement type on ground-borne vibrations due to road traffic." Edited by G. De Roeck, G. Degrande, G. Lombaert and G. Müller. *Proceedings of the 8th International Conference on Structural Dynamics.* Leuven, Belgium: EURODYN 2011. 777-784.

Leduc, Guillaume. 2008. *Road Traffic Data: Collection Methods and Applications.* JRC Technical Notes, Joint Research Centre (JRC), European Commission, Luxembourg, Luxembourg: Institute for Prospective Technological Studies, 55.

Loizos, Andreas, and C Plati. 2008. "An Alternative Approach to Pavement Roughness Evaluation." *International Journal of Pavement Engineering* (Taylor & Francis) 9 (1): 69-78. doi:10.1080/10298430600949894.

Lu, Pan, and Denver Tolliver. 2012. "Pavement Pre- and Post-Treatment Performance Models Using LTPP Data." *Journal of the Transportation Research Forum* (Transportation Research Forum) 51 (3): 67-81.

Mann, A. V., K. J. McManus, and J. C. Holden. 1997. "Power spectral density analysis of road profiles for road defect assessment." *Road and Transport Research* (ARRB Group Limited) 6 (3): 36-47.

Marcondes, Jorge, Gary J. Burgess, R. Harichandran, and Mark B. Snyder. 1991. "Spectral Analysis of Highway Pavement Roughness." *Journal of Transportation Engineering* 117 (5): 540–549.

Marquardt, Donald W. 1963. "An Algorithm for Least-Squares Estimation of Nonlinear Parameters." *Journal of the Society for Industrial and Applied Mathematics* (Society for Industrial and Applied Mathematics) 11 (2): 431-441.

Mednis, Artis, Girts Strazdins, Reinholds Zviedris, Georgijs Kanonirs, and Leo Selvano. 2011. "Real Time Pothole Detection using Android Smartphones with Accelerometers." *2011 International Conference on Distributed Computing in Sensor Systems and Workshops (DCOSS).* Barcelona, Spain: University of Latvia. 1-6.

Mohan, Prashanth, Venkata N. Padmanabhan, and Ramachandran Ramjee. 2008. "Nericell: Rich Monitoring of Road and Traffic Conditions using Mobile Smartphones." *Proceedings of the 6th ACM conference on Embedded network sensor systems - SenSys '08.* Bangalore, India: Microsoft Research India. 323.

Múčka, Peter. 2015. "Current Approaches to Quantify the Longitudinal Road Roughness." *International Journal of Pavement Engineering* (Taylor & Francis) Online. doi:10.1080/10298436.2015.1011782.

Múčka, Peter, and Johan Granlund. 2012. "Comparison of Longitudinal Unevenness of Old and Repaired Highway Lanes." *Journal of Transportation Engineering* (American Society of Civil Engineers (ASCE)) 138 (3): 371-380. doi:10.1061/(ASCE)TE.1943-5436.0000297.

Nagayama, Tomonori, Akira Miyajima, Shunya Kimura, Yuuki Shimada, and Yozo Fujino. 2013. "Road condition evaluation using the vibration response of ordinary vehicles and synchronously recorded movies." *Proceedings of the SPIE 8692, Sensors and Smart Structures Technologies for Civil, Mechanical, and Aerospace Systems 2013.* doi:10.1117/12.2010074.

Nakamura, Velma F., and Harold L. Michael. 1963. "Serviceability Ratings of Highway Pavements." *42nd Annual Meeting of the Highway Research Board.* Washington, D.C.: Highway Research Record. 1-36.

NCHRP 775. 2014. *Applying GPS Data to Understand Travel Behavior.* Report 775, Transportation Research Board, The National Academies, Washington, D.C.: National Cooperative Highway Research Program (NCHRP).

NCHRP. 2013. "Measuring, Characterizing, and Reporting Pavement Roughness of Low-Speed and Urban Roads." *Research in Progress.* National Cooperative Highway Research Program (NCHRP). Vols. 10-93. Edited by Amir N. Hanna. Washington, D.C.: Transportation Research Board of the National Academies, October 1.

Ndoye, Mandoye, Alan M. Barker, James V. Krogmeier, and Darcy M. Bullock. 2011. "Correlation-Averaging Algorithm for an Automated Distributed Road-Condition-Monitoring System." *IEEE Transactions on Intelligent Transportation Systems* (Institute of Electrical and Electronic Engineers) 12 (3): 795-808.

NHTSA. 2014. *U.S. Department of Transportation Announces Decision to Move Forward with Vehicle-to-Vehicle Communication Technology for Light Vehicles.* National Highway Traffic Safety Administration (NHTSA). February 3. Accessed April 25, 2014. www.nhtsa.gov.

NHTSA. 2011. *USDOT Connected Vehicle Research Program: Vehicle-to-Vehicle Safety Application Research Plan.* Report No. DOT HS 811 373, United States Department of Transportation (USDOT), Washington, D.C.: National Highway Traffic Safety Administration (NHTSA). www.safercar.gov/v2v.

North Dakota State Government. 2014. *North Dakota Geographic Information Systems.* 10 1. Accessed 10 1, 2014. www.nd.giv/gis.

—. 2014. *North Dakota Geographic Information Systems.* October 1. Accessed October 1, 2014. www.nd.giv/gis.

NREL. 2014. "National Renewable Energy Laboratory (NREL)." *Transportation Secure Data Center.* May 5. Accessed May 5, 2014. www.nrel.gov/tsdc.

O'Kane, Thomas, and John V. Ringwood. 2012. "Vehicle Speed Estimation Using GPS/RISS (Reduced Inertial Sensor System)." *The 24th Irish Signals and Systems Conference.* Donegal, Ireland: Letterkenny Institute of Technology.

Oke, S. A., T. A. O. Salau, O. A. Adeyefa, O. G. Akanbi, and F. A. Oyawale. 2007. "Mathematical Modelling of the Road Bumps Using Laplace Transform." *International Journal of Science & Technology* (Firat University) 2 (2): 129-141.

Oppenheim, Alan V., and Ronald W. Schaefer. 1975. *Digital Signal Processing.* Englewood Cliffs, New Jersey: Prentice-Hall.

Papagiannakis, A. Tom. 1997. "The Need for a New Pavement Roughness Index; RIDE." *International Truck & Bus Meeting & Exposition.* Washington, D.C.: Society of Automotive Engineers International. doi:10.4271/973267.

Papoulis, Athanasios. 1991. *Probalility, Random Variables, and Stochastic Processes.* New York: McGraw-Hill.

Perera, R. W., and S. D. Kohn. 2005. *Quantification of Smoothness Index Differences Related to Long-Term Pavement Performance Equipment Type.* Research, Office of Research, Development, and Technology, Soil and Materials Engineers, Inc., McLean: Federal Highway Administration, 159.

Perera, R. W., C. Byrum, and S.D. Kohn. 1998. *Investigation of Development of Pavement Roughness.* FHWA-RD-97-147, Washington, D.C.: Federal Highway Administration (FHWA). http://www.fhwa.dot.gov/publications/research/infrastructure/pavements/ltpp/97147/97147.pdf.

Ramji, K., A. Gupta, V. H. Saran, V. K. Goel, and V. Kumar. 2004. "Road Roughness Measurements using PSD Approach." *Journal of the Institution of Engineers, Civil Engineering Division* (Institution of Engineers) 85: 193-201.

Rizenbergs, Rolands L. 1965. *Accelerometer Method of Riding-Quality Testing.* Research Report KYHPR-64-25; HPS-HPR-1(26), Lexington, Kentucky: Kentucky Department of Highways, 47.

Robson, J. D. 1979. "Road Surface Description and Vehicle Response." *International Journal of Vehicle Design* (Inderscience Enterprises Limited) 1 (1): 25-35.

Shafizadeh, Kevan, Fred Mannering, and Linda Pierce. 2002. *A Statistical Analysis of Factors Associated with Driver-Perceived Road Roughness on Urban Highways.* Research Report WA-RD 538.1, Washington State Transportation Center (TRAC), University of Washington, Olympia,, Washington: Washington State Department of Transportation (WSDOT), 138.

Silva, Girisha Durrel De, Ravin Saranga Perera, and Ravin Saranga Perera. 2008. "Automated Pothole Detection Using Wireless Sensor Motes." *International IT Conference (IITC 08).* Colombo, Sri Lanka: University of Colombo School of Computing.

Solomon, P.D., J. Wang, and C. Rizos. 2011. "Latency Determination and Compensation in Real-Time GNSS/INS Integrated Navigation Systems." *Conference on Unmanned Aerial Vehicle*

in Geomatics. Waltham, MA: The International Society for Photogrammetry and Remote Sensing (ISPRS) Journal of Photogrammetry and Remote Sensing, Elsevier. C22.

Spangler, Elson B., and William J. Kelley. 1966. "GMR Road Profilometer -- A Method for Measuring Road Profile." *44th Annual Meeting of the Highway Research Board.* Washington, DC: Highway Research Board. 27-54. http://trid.trb.org/view.aspx?id=104787.

Sun, Lu. 2003. "Simulation of Pavement Roughness and IRI Based on Power Spectral Density." *Mathematics and Computers in Simulation* (Elsevier Science B. V.) 61 (2): 77-88. doi:10.1016/S0378-4754(01)00386-X.

Tai, Yu-chin, Cheng-wei Chan, and Jane Yung-jen Hsu. 2010. "Automatic Road Anomaly Detection Using Smart Mobile Device." *Proceedings of the 2010 Conference on Technologies and Applications of Artificial Intelligence (TAAI2010).* Hsinchu City, Taiwan: National Taiwan University.

The Transtec Group. 2012. *Smoothness Specifications Online - Overview of Current Practices.* The Transtec Group, Inc. March 28. Accessed March 28, 2015. SmoothPavements.com.

Thomas, George B., and Ross L. Finney. 1995. *Calculus and Analytic Geometry.* 9th. Addison Wesley.

Todd, Kevin B., and Bohdan T. Kulakowski. 1989. "Simple Computer Models for Predicting Ride Quality and Pavement Loading for Heavy Trucks." *Transportation Research Record* (Transportation Research Board) (1215): 137-150.

Tomiyama, Kazuya, Akira Kawamura, and Tomonori Ohiro. 2014. "Automatic Detection of Surface Distress Due to Frost Heaving on Expressway by Use of an Accelerometer-Based Profilometer." *Journal of Japan Society of Civil Engineers* (Japan Society of Civil Engineers) 2 (1): 323-330. doi:http://dx.doi.org/10.2208/journalofjsce.2.1_323.

TRIP. 2013. *Bumpy Roads Ahead: America's Roughest Rides and Strategies to Make our Roads Smoother.* Research Report, Washington, D.C.: The Road Improvement Project (TRIP).

Türkay, Semiha, and Hüseyin Akçay. 2008. "Influence of tire damping on the ride performance potential of quarter-car active suspensions." *47th IEEE Conference on Decision and Control.* Institute of Electrical and Electronic Engineers.

USDHS. 1996. *NAVSTAR GPS User Equipment Introduction.* Technical Guide, United States Coast Guard, Navigation Center, Washington, D.C.: U.S. Department of Homeland Security, 215. http://www.navcen.uscg.gov/pubs/gps/gpsuser/gpsuser.pdf.

USDOT. 2014. *2013 Status of the Nation's Highways, Bridges, and Transit: Conditions & Performance.* Report to Congress, Washington, D.C.: United States Department of Transportation (USDOT).

—. 2012. "Enabling a Secure Environment for Vehicle-to-Vehicle (V2V) and Vehicle-to-Infrastructure (V2I) Transactions." Edited by Booz Allen Hamilton. *April 2012 Public*

Workshop. Washington, D.C.: ITS Joint Program Office, Research and Innovative Technology Administration (RITA), United States Department of Transportation (USDOT).

—. 2014. "Together, we can GROW AMERICA." *United States Department of Transportation.* April 30. Accessed May 5, 2014. www.dot.gov/grow-america.

—. 2014. "USDOT's Connected Vehicle Reference Implementation Architecture (CVRIA)." *Stakeholders Outreach Meeting.* Washington D.C.: United States Department of Transportation (USDOT) Office of the Assistant Secretary for Research and Technology. 131.

Verizon. 2014. "Fleet Managemetn Solutions for Your Business." *Networkfleet's GPS Fleet Tracking System.* May 5. Accessed May 5, 2014. www.networkfleet.com.

Waechter, M., F. Riess, H. Kantz, and J. Peinke. 2003. "Stochastic analysis of road surface roughness." *Europhysics Letters* (IOP Publishing) 64 (5): 579. doi:10.1209/epl/i2003-00616-4.

Walker, Roger S., Emmanuel Fernando, and Yoshitaka Sho. 2005. *A Methodology for Bump Detection Using Inertial Profile Measurements.* Research Report FHWA/TX-05/0-4479-1, Research and Technology Implementation Office, Texas Department of Transportation (TxDOT), Arlington, Texas: The University of Texas at Arlington for TxDOT, 86.

Wang, Chih-Jye, and Wei-Shinn Ku. 2012. "Anonymous Sensory Data Collection Approach for Mobile Participatory Sensing." *2012 IEEE 28th International Conference on Data Engineering Workshops (ICDEW).* Arlington, Virginia: Institute of Electrical and Electronic Engineers (IEEE). 220-227. doi:10.1109/ICDEW.2012.78.

Wang, Ming, Ralf Birken, and Salar Shahini Shamsabadi. 2014. "Framework and implementation of a continuous network-wide health monitoring system for roadways." Edited by H. Felix Wu, Tzu-Yang Yu, Andrew L. Gyekenyesi and Peter J. Shull. *Proc. SPIE 9063, Nondestructive Characterization for Composite Materials, Aerospace Engineering, Civil Infrastructure, and Homeland Security 2014.* San Diego, California: Society of Photo-Optical Instrumentation Engineers (SPIE). 12. doi:10.1117/12.2047681.

Wei, Liu, T. F. Fwa, and Zhao Zhe. 2004. "Pavement Roughness Analysis Using Wavelet Theory." *6th PMS Conference.* Brisbane, Australia: National University of Singapore. http://www.pavementmanagement.org/ICMPfiles/2004014.pdf.

Wermers, Lyle G. 1962. *Analysis of Road Roughness of Flexible Pavements Using the Kentucky Accelerometer.* FHWA/IN/JHRP-62/16 Project No. C-36-54BB, Lafayette, Indiana: Purdue University, 20. doi:10.5703/1288284313610.

Woodyard, Chris. 2007. *Vehicles keep inching up and putting on pounds.* July 16. Accessed March 14, 2014. http://usatoday30.usatoday.com/money/autos/2007-07-15-little-big-cars_N.htm.

Yagi, Koichi. 2013. "A Measuring Method of Road Surface Longitudinal Profile from Sprung Acceleration and Verification with Road Profiler." *Journal of Japan Society of Civil Engineers, Ser. E1 (Pavement Engineering)* (Japan Science and Technology (JST)) 69 (3): 1-7.

APPENDIX A. DATA PROCESSING ALGORITHMS

This appendix provides an overview of the software developed to process the data, implement the RIF-transform, and produce the EAR-indices.

A.1. Data Processing Procedure

Evaluating and cleaning the data is a first step in computing the RIF-transform. The onboard sensors will upload data files periodically to a server. The algorithm examines the input queue for new files to process.

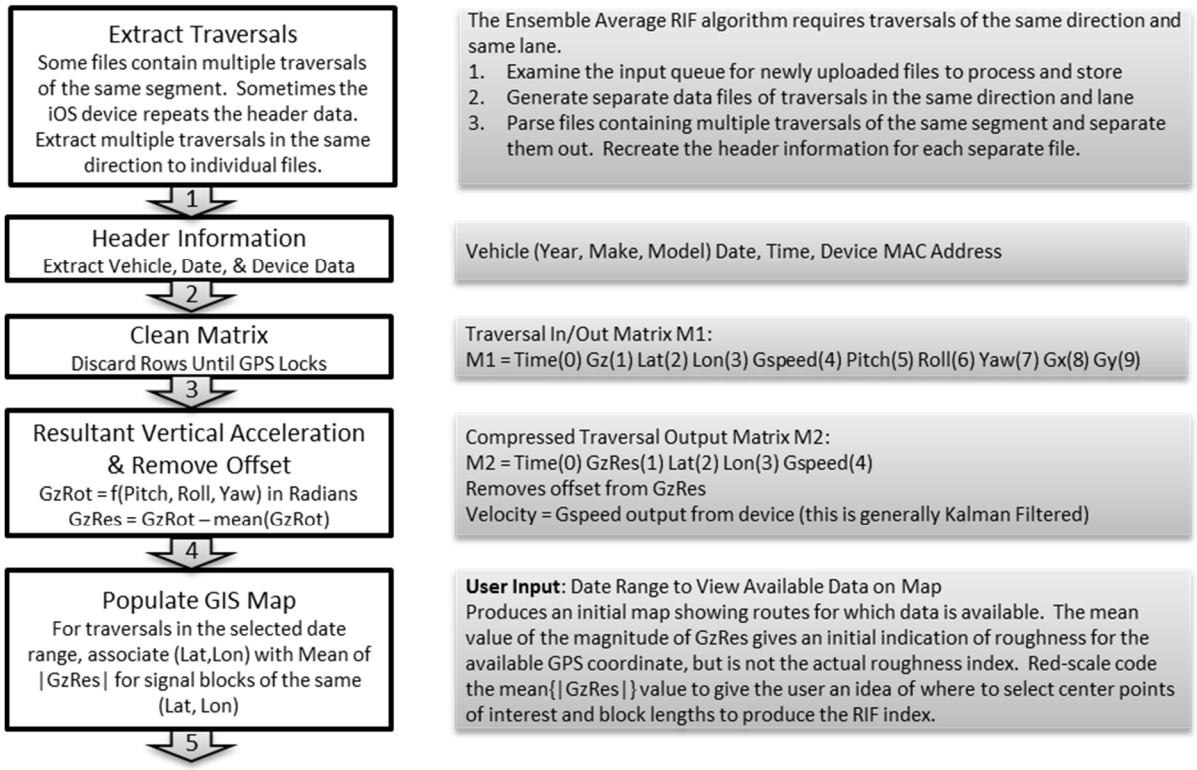

Figure A.1. Data preparation procedure

Figure A.1 summarizes the sequence of steps to process the raw data from each .CSV file. The header contains relevant data about the vehicle and the onboard sensor types.

A.2. Segment Extraction Procedure

After validation of the data quality through the cleansing process, the procedure extracts the relevant segments of specified lengths for processing.

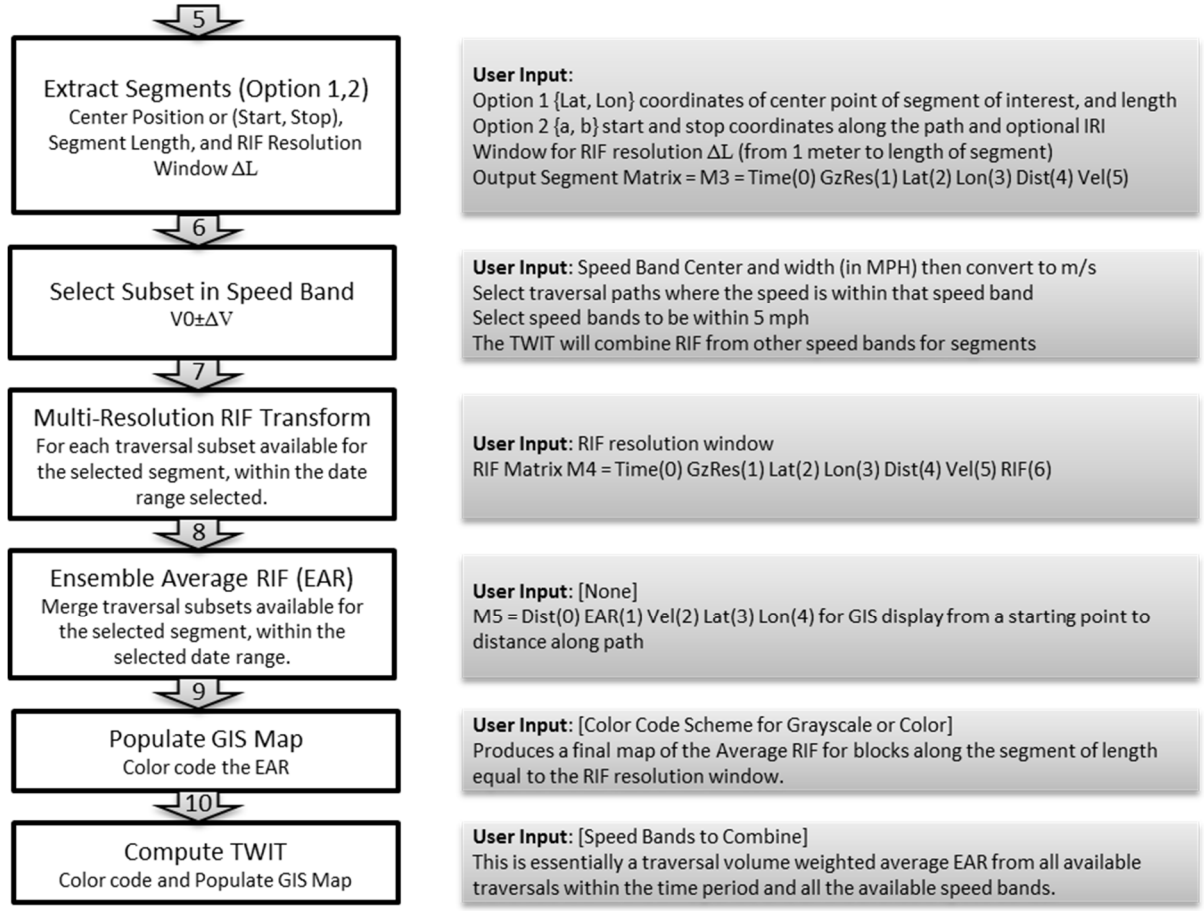

Figure A.2. Segment extraction procedure

Figure A.2 summarizes the steps in the procedure to extract the specified segments of a specified speed band. The steps following are computation of the RIF-transforms for the specified spatial resolution, the corresponding EAR-indices, and optionally populating the data into a GIS map. When data are available for multiple speed bands of traversals for a segment, the TWIT-indices will display a speed independent indication of roughness.

APPENDIX B. VEHICLE USED IN THE CASE STUDIES

This appendix provides a summary of the various vehicles used for the case studies and the estimates of their quarter-car parameters.

B.1. Frequency Responses

2011 Ford E350 (Van)

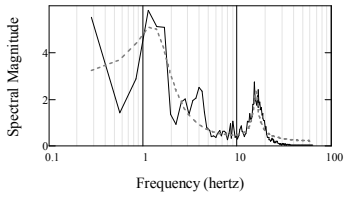

2011 Ford E350 (NDDOT)

2007 Toyota Camry LE (Luxury Car)

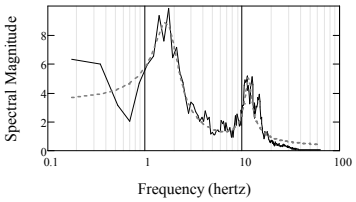

2007 Toyota Camry LE (Luxury Car)

2007 Subaru Legacy (Compact Car)

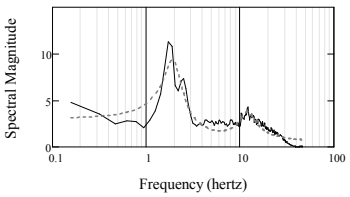

2007 Subaru Legacy (Compact Car)

2001 Ford Explorer (SUV)

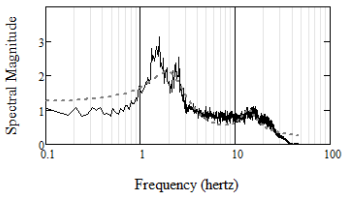

2001 Ford Explorer (SUV)

2011 Chevrolet Traverse (Mini-Van)

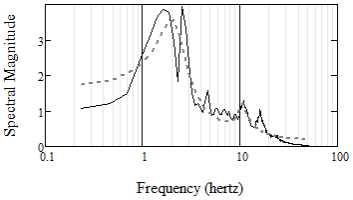

2011 Chevolet Traverse (Mini-Van)

Figure B.1. Vehicles used for the various case studies

The charts on the left side of Figure B.1 shows the DFT of the inertial signal obtained from sensors installed in the respective vehicles pictured on the right side. The dotted lines of the plots are the quarter-car model estimates from fitting the data using a least-squares method.

B.2. Quarter-Car Parameter Estimates

Table B.1. Parameter estimates for the composite quarter-car

Vehicle	f_s (hertz)	ζ_s	f_u (hertz)	ζ_u
2011 Ford E350 (Van)	1.4	0.39	15.7	0.05
2007 Toyota Camry LE	1.7	0.27	11.5	0.08
2007 Subaru Legacy	1.9	0.22	11.9	0.18
2001 Ford Explorer	2.2	0.46	13.8	0.18
2011 Chevrolet Traverse	2.1	0.35	10.8	0.10

Table B.1 summarizes the sprung- and unsprung-mass estimates for the quarter-car representation of each vehicle. These results show that the parameters for different vehicle types are consist with the expected response that complies with design guidelines of the international standards for human safety and comfort.